Simulating Semiclassical Black Holes

Benjamin Berczi

Centre for Astronomy and Particle Theory

Supervised by

Paul M. Saffin

UNITED KINGDOM · CHINA · MALAYSIA

Thesis submitted to the University of Nottingham for the degree of
Doctor of Philosophy, September 2023.

Abstract

In this thesis the first attempts to study the real-time dynamics of semiclassical gravitational collapse and semiclassical black holes are presented. Specifically, the chosen system is a massless quantum scalar field coupled to Einstein gravity in spherical symmetry in four dimensions. The semiclassical system is built using a coherent state as the chosen quantum state, which enables the semiclassical simulations to connect to classical ones. Thus, the existing literature of classical collapse can be utilised and semiclassical simulations can be built upon them. The quantum field is regularised using dynamical Pauli-Villars fields. This formalism is ideal to study semiclassical gravitational collapse and critical phenomena, as well as correlation functions to look for signals of Hawking radiation.

The thesis explores multiple formulations of such simulations, both in terms of the system of equations and numerical methods. The first part of the thesis uses the ADM formulation of the Einstein equations whilst the second part uses the characteristic formulation. For both cases the formation of semiclassical black holes is presented with associated quantum effects around the black holes. Backreaction is studied and the effect of the quantum effects on the resulting black hole masses are analysed. In addition, the first study of a semiclassical version of Choptuik scaling is presented. Correlation functions are studied and long-range correlations are found between the inside and outside of the horizon of black holes, however, whether or not these correspond to Hawking radiation remains a question.

Declaration

This dissertation contains my own work unless otherwise referenced, carried out under the supervision of Paul M. Saffin at the University of Nottingham. No part of this thesis has previously been submitted for a degree or other qualification at this or any other university.

Chapter 2 contains original research presented in the following papers:

- BB, Paul M. Saffin, and Shuang-Yong Zhou. Gravitational collapse with quantum fields. Phys. Rev. D, 104(4):L041703, 2021.
- BB, Paul M. Saffin, and Shuang-Yong Zhou. Gravitational collapse of quantum fields and choptuik scaling. Journal of High Energy Physics, 2022(2), feb 2022.

These papers are listed in the bibliography as references [1, 2], respectively.

Benjamin Berczi

Nottingham, September 30, 2023

Acknowledgements

First and foremost I would like to thank my supervisor, Paul, for the opportunity to work on such an exciting project and for his continuous support throughout the years. I could not have wished for a better supervisor, helping me with general guidance as well as specific problems of quantum fields or writing code. In addition, I am grateful for the help and support of our collaborator, Zhou.

I would also like to thank my colleagues at CAPT and in general Nottingham for creating a warm and welcoming atmosphere. Due to the pandemic I was working remotely most of my PhD, but nevertheless I have great memories of both (briefly) living in Nottingham and visiting for day trips countless times. Thank you Chad, Swagat, Cesc, Sergio, Matt, Kieran, Moustafa, Finlay, CB, Roan, Simon, Oli, Pete, Ed, Ben and many others.

I am grateful for the support from my partner, Anna, who has listened to more physics than she wanted to in the last couple of years. I am also thankful for the support I got from my parents and family throughout my studies.

Lastly, I would like to thank my friends in (and out of) London, who kept me sane working remotely all the time; Ollie, Bryony, Dragos, Matyas, Dori, Ruth, Giulia, Rizzy, Pichi, Veronika and many others. Last, but not least, my friends from home; Gergo, Viktor, Laci, Fanni, Andras, Levi, Milan and more.

Contents

List of Figures

Chapter 1

Introduction

1.1 Black holes

Black holes are fascinating objects in the universe that form as the end states of gravitational collapse, a unique manifestation of the strength and special nature of gravity. Since Hawking's famous calculation [6], we know that black holes have a temperature, as they can evaporate via Hawking quanta. This is an astonishing result, as it connects general relativity to quantum field theory, which is another pillar of modern physics that underlies all known matter sources in the universe. While stationary astronomical black holes are expected to exhibit little in the way of quantum effects outside the event horizons, the dynamical formation of black holes or other compact stars may involve extreme matter sources that are quantum in essence. Moreover, primordial black holes may form in the early universe [7] and can have a high temperature and large Hawking radiation. Purely theoretically, black holes along with their quantum properties have caused great puzzles but also great advances in our understanding of gravity and quantum field theory.

1.2 Gravitational collapse

The dynamics of classical gravitational collapse with various matter sources have been studied over the years. The simple pressure-less homogeneous dust model was studied as early as the late 1930s [8, 9]. This has been generalized to spherically symmetric inhomogeneous dust models [10, 11, 12, 13, 14, 15] and more general perfect fluid models [16, 17, 18, 19, 20, 21].

While black holes are the natural end states of gravitational collapse, it is singularities that must form as the end states of gravitational collapse from reasonable matter sources, as required by the singularity theorems of [22, 23]. The cosmic censorship conjecture [24] suggests that naked singularities should be cloaked by horizons under appropriate assumptions so as to avoid loss of predictability at the singularities. However, naked singularities do appear in the above models of gravitational collapse. A major purpose of the gravitational collapse studies is to clarify the scopes and the assumptions of the cosmic censorship conjecture. See [25] for a review on gravitational collapse and spacetime singularities.

At a more fundamental level, one may model the matter source as a scalar field, which provides arguably the simplest arena to probe the nonlinearities of general relativity and its interaction with matter. Classical scalar collapse in spherical symmetry has been analytically investigated by [26, 27, 28, 29, 30, 31], which also provides counter-examples to the naive cosmic censorship [30]. Indeed, as numerically uncovered by [32], interesting critical phenomena exist in spherical scalar collapse that are characterized by scale invariance and universal scaling of the black hole mass with initial data. The critical collapse happens at the boundary between the parameter region of regular initial data that can form black holes and the region that can not, and the singularity at critical collapse is exactly a naked singularity, as explicitly shown in an analytical example [33]. [34, 35] provided some further insights into the critical phenomena. Critical collapse has

also been observed with axisymmetric gravitational waves [36], spherical collapse of radiation fluid [37] and a non-Abelian field [38]. A real analytical solution of the Choptuik spacetime has recently been constructed [39]. See [40] for a review of critical collapse.

1.3 Semiclassical black holes

Since Hawking's famous 1974 calculation [6], we know that black holes are not eternal, but they radiate thermally and lose their mass slowly. As black holes evaporate, they seemingly turn pure states into (thermal) mixed states, which is a paradox as it means that information about the pure state is lost. This is the so-called black hole information paradox. Hawking argued that indeed this is what happens and thus gravity breaks the conservation of information in quantum mechanics.

Hawking's calculation shows without a doubt that black holes radiate, however, how exactly this happens remains unknown, as Hawking's statements rely on past and future null infinities. Questions about the location of Hawking radiation, the exact rate of black hole mass loss and the nature of the end state of evaporation remain unanswered. Thus, the local dynamics of particle creation and black hole evaporation is still a mystery. There have been suggestions to answer these questions, like the famous firewall proposal [41], where the authors suggest that there is a firewall at the horizon, as Hawking radiation is completely localised there. However, this is not widely accepted, and there have been arguments made against this idea, see e.g. [42].

In addition, quantum effects might become important in the context of Choptuik scaling in gravitational collapse. Recall that the critical phenomena in gravitational collapse suggests that naked singularities are valid end states of the collapse

if the initial data is fine-tuned, which violates the weak cosmic censorship. Quantum effects may change this behaviour qualitatively and stop naked singularities from forming [43].

To answer questions about the detailed dynamics of Hawking radiation and quantum fields around black holes in general, hence, it is necessary to study dynamical semiclassical black holes in four dimensions. This is a difficult task for many reasons. Firstly, one has no access to analytical expressions of the quantum mode functions that the relevant quantum field decomposes into, whereas in vacuum these take the form of simple plane waves. Secondly, in vacuum one can simply regularise quantum field theories using normal ordering, however, in general spacetimes, it cannot be used.

Early attempts to study semiclassical collapse include [44, 45, 46]. The quantum properties of spherical shell collapse have also been investigated by [47, 48, 49], and [50, 51, 52, 53] studied dilaton collapse in two dimensions gravity, which is drastically different from a four dimensional model for a number of reasons. First of all, by restricting to spherical symmetry or a two dimensional setup, these models essentially neglected all the effects of the spherical harmonics in the mode expansion, which are important for a thorough understanding of a dynamical gravitational collapse.

1.4 Project outline

In this thesis I present the first numerical simulations of semiclassical collapse of a massless scalar field in four dimensions in spherical symmetry[1]. The core idea in the construction of these simulations is the use of a specific quantum state in which expectation values are taken; a coherent state. This allows the semi-

[1]Note that the codes written for the simulations are available at [2].

classical simulations to straightforwardly connect to classical simulations, as the expectation value of a quantum scalar in the coherent state is exactly equivalent to a classical scalar. Thus, one can construct semiclassical simulations by building upon classical ones, and adding extra quantum mode functions as dynamical variables.

It is important to mention that the geometry is spherically symmetric, but the quantum scalar field itself may fluctuate non-spherically. It is the coherent state that is spherically symmetric, thus the expectation value of the quantum scalar taken in the coherent state is a spherically symmetric object. Thus there is no inconsistency at the level of the equations of motion. Then all quantum modes may have a contribution to the stress-energy tensor in the system, not just the spherically symmetric zero-mode.

The quantum field is regularised using massive dynamical Pauli-Villars ghost fields. Even though in theory the quantum field is composed of infinite quantum modes, throughout this thesis I show that a finite number of them is sufficient to capture all the physical quantum effects present in these simulations. Nevertheless, a large number of quantum modes is needed to capture the quantum effects (order of thousands) which makes these semiclassical simulations computationally expensive, both in memory and time.

The structure of the thesis is as follows. In Chapter 2 I present our first attempt at a full semiclassical collapse simulation. This uses the ADM formulation of the Einstein equations and finite difference methods as the numerical scheme. I show that a finite amount of modes create a well-defined stress-energy tensor that is regularised by massive Pauli-Villars fields. Then I show results of the dynamical simulations of both no black hole formation and black hole formation evolutions. I present new quantum effects in case of the black hole formation that are validated by convergence tests with respect to the number of quantum

mode functions. I also present the first picture of dynamical backreaction of the quantum effects, semiclassical Choptuik scaling and study of correlation functions in search of signals of Hawking radiation.

In Chapter 3 I present the same semiclassical system but using spectral methods as a numerical scheme. I find a specific spectral method that works well for the purposes of these simulations and a detailed description of it. I show, however, that these numerical methods do not perform better than the previous finite difference methods, and conclude that they are not better suited for semiclassical simulations.

In Chapter 4 I introduce a semiclassical collapse simulation where the outer boundary is ingoing null and thus the physical domain is shrinking, based on [4]. This creates an ideal scenario to study the fine-structure of Choptuik scaling, as the dynamics similarly shrinks as the critical solution is approached. I present the semiclassical version of the simulation with results of quantum effects, and reproduce the fine-structure of Choptuik scaling classically. However, the semiclassical version of Choptuik scaling is not studied, as the numerical methods used in this system are not sufficient for the stable simulation of the quantum mode functions in this case.

In Chapter 5 and 6 I change the form of Einstein equations used from the ADM formulation to the double null or characteristic formulation. In Chapter 5 I present a version of this system where the centre of the physical space is part of the numerical domain, based on [54], in order to study the fine-structure of Choptuik scaling, as in this formulation, the numerical domain is naturally shrinking. I successfully reproduce the classical version of Choptuik scaling once again, however, the semiclassical version cannot be studied due to similar numerical difficulties arising regarding the quantum mode functions, similarly as before.

In Chapter 6 I present a version of a double null collapse where the physical centre

of the spacetime is not part of the numerical domain, hence allowing for a more stable simulation for the quantum modes. This results in stable and long-time evolutions of semiclassical black holes, allowing the detailed study of quantum effects. I show the late-time behaviour of quantum fluctuations around the black hole, and validate these using convergence tests. I also study correlation functions in order to find signals for long-range correlations inside and outside of the horizon of the black hole. I find long-range correlations but it remains a question whether or not these constitute as Hawking radiation signals.

I end the thesis with Chapter 7 where I summarise, draw conclusions and suggest directions of future work.

Part I

ADM formulation

Chapter 2

Quantum collapse

2.1 Introduction

In this chapter I will present a formalism that allows us to simulate the gravitational collapse of a quantum scalar field into a black hole. This was first reported in [55] where the formalism was introduced and some initial results were obtained. (Ref. [56], which appeared after [55], studied a similar system with a different method that only included the spherical mode for the quantum field.) This chapter, based on [1], provides a more thorough overview of the formalism with all essential technical details. Specifically, a spherically symmetric massless quantum scalar field is coupled to classical gravity. Importantly, the notion of coherent states is utilised so that the semiclassical system can be built upon the previously well-studied classical collapse. Namely, the expectation value of the quantum scalar field operator in the coherent state is identified with the classical scalar field of classical collapse. This is a crucial point in the formalism because it allows one to split the stress-energy tensor components into a sum of contributions from the "classical field" and contributions from quantum modes.

It is also essential in the formalism to make use of the latest stable numerical relativity formulations of the Einstein equations, as numerically the quantum field simulation corresponds to a simulation of thousands of mode functions, which is computationally much more demanding in numerical accuracy and stability than the classical collapse. Also, to further sustain a sufficiently long period of simulation, as high as a tenth order finite difference method is used and introduce artificial dissipation terms in our equations of motion. Another major difference in simulations with products of quantum fields evaluated at the same spacetime point is that there will be UV divergences that needs cancelling, similar to loop calculations in quantum field theory. In this chapter and throughout the thesis Pauli-Villars fields are used to regularise the quantum field together with a cosmological constant.

I reproduce the results of classical scalar collapse to a black hole with our semiclassical simulations and extract the quantum deviations for the stress-energy tensor. Choptuik scaling is also studied for the semiclassical critical collapse and it is found that when approaching the critical point the quantum deviations from the classical Choptuik scaling actually decrease. These results are validated with various convergence studies.

2.2 Classical collapse

In this section the theory for the simulation of the collapse of a spherically symmetric classical massless scalar field is discussed using the methods of [57] but with a different gauge choice. First, the geometrical side of the Einstein equation will be presented using variables that make the evolution equations better suited for lattice simulations, and then the chosen matter fields are discussed. Before connecting the geometry to the matter equations, the gauge choices are

reviewed briefly. Lastly, the choices for the initial conditions for the simulation are shown. Note that in the simulation all the fundamental constants are set to one, $\hbar = c = M_P = 1$. If displayed, their purpose is simply for illustration.

2.2.1 Geometry

I will restrict the simulations to have spherical symmetry in $3+1$D in this chapter and throughout the thesis. For classical simulations, it is certainly viable to do full $3+1$D simulations with modern hardware, but real time simulations with quantum fields involve solving partial differential equations for many quantum modes simultaneously, which is computationally very expensive. Thus, the following spherically symmetric line element is chosen:

$$ds^2 = -\alpha^2(t,r)dt^2 + A(t,r)dr^2 + r^2 B(t,r)(d\theta^2 + \sin^2\theta d\varphi^2), \tag{2.1}$$

where $\alpha(t,r)$ is the lapse function and $A(t,r)$ and $B(t,r)$ are functions governing the spatial part of the metric. The lapse function $\alpha(t,r)$ has a crucial role to play in the collapse — not only will it be used to choose a Bona-Masso type gauge condition, but also one can use it to identify the formation of a black hole, due to the "collapse of the lapse" phenomenon [57].

In order to create a more stable simulation, the system is cast into a first order system, only involving first order partial differential equations. To achieve this, the following additional variables are defined:

$$\begin{aligned} K_A &= -\frac{1}{2\alpha}\frac{\dot{A}}{A}, & D_A &= \frac{A'}{A}, \\ K_B &= -\frac{1}{2\alpha}\frac{\dot{B}}{B}, & D_B &= \frac{B'}{B}, \\ \lambda &= \frac{1}{r}\Big(1 - \frac{A}{B}\Big), & D_\alpha &= \frac{\alpha'}{\alpha}, \end{aligned} \tag{2.2}$$

where the dot represents differentiation with respect to t, and the prime represents differentiation with respect to r.

Note that λ is defined in order to guarantee the local flatness of the metric (at $r = 0$). Local flatness in these coordinates manifests itself as $A(t, r = 0) = B(t, r = 0)$ for all t. Many $1/r$ terms in the evolution equations discussed below are only regular (not divergent) numerically, if this local flatness condition is exactly met. Small numerical errors in $A(t, r = 0)$ and $B(t, r = 0)$ could mean exponential divergences in the numerical system. Hence, using the definition of $\lambda(t, r)$, and further requiring it to be antisymmetric, the local flatness condition is exactly met at each time step.

In addition, to ensure that the system of equations is strongly hyperbolic for any gauge choice of $\alpha(t, r)$, some further changes of variables are performed. Namely, instead of (K_A, D_A), the functions $(K, \tilde{U})$ are used, respectively,

$$\begin{aligned} K &= K_A + 2K_B, \\ \tilde{U} &= D_A - 2D_B - \frac{4B\lambda}{A}. \end{aligned} \tag{2.3}$$

The detailed motivation for these choices are explained more in depth in [57], but essentially for some gauge choices for the lapse function $\alpha(t, r)$ the original system is not strongly hyperbolic. Hence, using the above change of variables, the system is strongly hyperbolic for any gauge choice of $\alpha(t, r)$, which are discussed at the end of this subsection.

Then the non-zero components of the Einstein tensor can be written as

$$G^t{}_r = \frac{2}{\alpha}\left[- K_B' + \Big(\frac{1}{r} + \frac{D_B}{2}\Big)(K - 3K_B)\right], \tag{2.4}$$

$$\begin{aligned} G^t{}_t =& \frac{1}{A}\left[D_B' + \frac{1}{r}\Big(\lambda + D_B - \tilde{U} - \frac{4\lambda B}{A}\Big) - D_B\Big(\frac{1}{4}D_B + \frac{1}{2}\tilde{U} + \frac{2\lambda B}{A}\Big)\right] \\ & - K_B(2K - 3K_B), \end{aligned} \tag{2.5}$$

$$\begin{aligned} G^r{}_r =& \frac{2}{\alpha}\left[\dot{K}_B - \frac{3}{2}\alpha K_B^2 + \frac{\alpha}{2r^2 A}\Big(1 - \frac{A}{B}\Big) + \frac{\alpha}{2rA}D_B + \frac{\alpha}{8A}D_B^2 \right. \\ & \left. + \frac{\alpha}{rA}D_\alpha + \frac{\alpha}{2A}D_B D_\alpha\right], \end{aligned} \tag{2.6}$$

$$\begin{aligned} G^\theta{}_\theta =& \frac{1}{\alpha}(\dot{K} - \dot{K}_B) - K^2 + 3K_B(K - K_B) + \frac{1}{2A}(D_B' + 2D_\alpha') \\ & - \frac{1}{4A}\left[(D_B + 2D_\alpha)\Big(\tilde{U} + D_B + \frac{4B\lambda}{A}\Big) - 4D_\alpha^2\right] \\ & + \frac{1}{2rA}\Big(2D_\alpha - \tilde{U} - \frac{4B\lambda}{A}\Big). \end{aligned} \tag{2.7}$$

The $G^r{}_t$ and $G^t{}_t$ components of the Einstein equations are actually constraint equations, which do not contain time derivatives with the new dynamical variables above. They are called the momentum and Hamiltonian constraint respectively

$$P = K_B' - \Big(\frac{1}{r} + \frac{D_B}{2}\Big)(K - 3K_B) + \frac{\alpha}{2}G^t{}_r = 0, \tag{2.8}$$

$$\begin{aligned} H =& D_B' + \frac{1}{r}\Big(\lambda + D_B - \tilde{U} - \frac{4\lambda B}{A}\Big) - D_B\Big(\frac{1}{4}D_B + \frac{1}{2}\tilde{U} + \frac{2\lambda B}{A}\Big) \\ & - AK_B(2K - 3K_B) - AG^t{}_t = 0. \end{aligned} \tag{2.9}$$

where $G^t{}_r$ and $G^t{}_t$ are understood to be replaced with the corresponding components of the stress-energy tensor via the Einstein equations. These constraints provide a sanity check on whether numerical errors are under control in the simulation.

The metric ansatz, Eq. (2.1), contains gauge/coordinate degrees of freedom. Particularly, one may freely choose α as a gauge choice, which slices the spacetime

into hypersurfaces with the same times. Since the spacetimes in these simulations, once a black hole forms, will contain singularities, one must choose a singularity avoiding gauge choice. This ensures that even when a singularity is present inside an apparent horizon, the spatial grid outside of the horizon may still be evolved. The two established families of singularity avoiding gauge choices are maximal slicing conditions and Bona-Masso type slicing conditions [58].

Maximal slicing conditions are used in [57], which is equivalent to demanding that the extrinsic curvature of the equal time hypersurface is constant in time. This leads to a constraint equation involving α that needs to be integrated with respect to r in spherical symmetry.

The Bona-Masso type slicing conditions [58], on the other hand, treat α as a dynamical variable, which is artificially specified by an evolution equation along with the evolution of other physical variables. These are also called hyperbolic slicing conditions, since $\alpha(t, r)$ obeys a wave equation with a source containing K.

Although maximal slicing is a robust gauge choice, it is computationally more expensive and slower for our purposes, since one needs to integrate spatially at every time step. The Bona-Masso type gauges possess similar robustness, but requires less computational power, since one just has an additional dynamical field that needs to integrated in time. Therefore, in the present simulations, Bona-Masso type slicing conditions are used. Specifically, the lapse function $\alpha(t, r)$ is chosen to satisfy the following evolution equation

$$\dot{\alpha} = -\alpha^2 f(\alpha) K, \tag{2.10}$$

where $f(\alpha)$ is a suitable function of α, to be tuned in a particular problem. The α evolution also leads to the evolution of D_α, which is given by

$$\dot{D}_\alpha = -\partial_r(\alpha f(\alpha) K). \tag{2.11}$$

The most used gauge choice within the Bona-Masso family is the 1+log gauge, which is given by

$$f(\alpha) = \frac{2}{\alpha}. \tag{2.12}$$

This choice ensures strong singularity avoidance and is the one I use.

2.2.2 Matter

Now let us turn to the scalar field involved in the simulation. The matter at hand is the simplest possible choice, a free massless scalar Φ, which couples minimally to gravity. Classically, the scalar field acts as a stress-energy source to the Einstein equation, and gravity also influences the matter via the Klein-Gordon equation. The stress-energy tensor for the scalar field is the following:

$$T_{\mu\nu} = \partial_\mu \Phi \partial_\nu \Phi - \frac{1}{2} g_{\mu\nu} \Big[g^{\rho\sigma} \partial_\rho \Phi \partial_\sigma \Phi \Big]. \tag{2.13}$$

Additionally, the following new field variables are introduced for the scalar field

$$\Pi = \frac{A^{\frac{1}{2}} B}{\alpha} \dot{\Phi}, \qquad \Psi = \Phi', \tag{2.14}$$

which are needed to formulate the scalar evolution equations with only first order derivatives. With these variables, the stress-energy tensor can be decomposed into

$$\rho = n^\mu n^\nu T_{\mu\nu} = \frac{1}{2A} \left(\frac{\Pi^2}{B^2} + \Psi^2 \right) + \frac{1}{2Br^2} (\partial_\theta \Phi)^2 + \frac{1}{2Br^2 \sin^2\theta} (\partial_\varphi \Phi)^2, \tag{2.15}$$

$$j_A = -n^\mu T_{\mu r} = -\frac{\Pi \Psi}{A^{\frac{1}{2}} B}, \tag{2.16}$$

$$S_A = \gamma^{rr} T_{rr} = \frac{1}{2A} \left(\frac{\Pi^2}{B^2} + \Psi^2 \right) - \frac{1}{2Br^2} (\partial_\theta \Phi)^2 - \frac{1}{2Br^2 \sin^2\theta} (\partial_\varphi \Phi)^2, \tag{2.17}$$

$$S_B = \gamma^{\theta\theta} T_{\theta\theta} = \frac{1}{2A} \left(\frac{\Pi^2}{B^2} - \Psi^2 \right) + \frac{1}{2Br^2} (\partial_\theta \Phi)^2 - \frac{1}{2Br^2 \sin^2\theta} (\partial_\varphi \Phi)^2. \tag{2.18}$$

Here n^μ is the unit timelike vector orthogonal to the equal time hypersurface, and γ^{ij} is the inverse of the spatial part of the metric. Note that in my coordinates these quantities are simply $\rho = -T^t{}_t$, $j_A = T^t{}_r$, $S_A = T^r{}_r$ and $S_B = T^\theta{}_\theta$.

2.2.3 Evolution equations

The Einstein equations and the scalar equation of motion are respectively given by

$$G_{\mu\nu} = \frac{1}{M_P^2}\big(T_{\mu\nu} - \Lambda g_{\mu\nu}\big), \tag{2.19}$$

$$\Box\Phi = 0, \tag{2.20}$$

where $M_P = 1/\sqrt{8\pi G}$ is the reduced Planck mass and I have also added the (bare) cosmological constant Λ as a stress-energy source. As I am interested in an asymptotically flat spacetime, for classical simulations, I can set the cosmological constant to zero, but the presence of a cosmological constant is required to regularise the quantum field in the semiclassical system, as will be explained in Section 2.3.4 in detail.

As mentioned above, the goal is to cast these field equations in a first order form, which can be achieved by evolving the following variables introduced previously

$$(\Phi^{(s)},\ \Psi^{(a)},\ \Pi^{(s)},\ A^{(s)},\ B^{(s)},\ D_B^{(a)},\ \tilde{U}^{(a)},\ K^{(s)},\ K_B^{(s)},\ \lambda^{(a)},\ \alpha^{(s)},\ D_\alpha^{(a)}), \tag{2.21}$$

where the first three fields are matter fields, the others are metric fields, and the (temporarily added) superscript indicates whether the field is symmetric or antisymmetric around $r = 0$, as the initial data has definite parity to help with numerical stability. The Klein-Gordon equation (2.20) can be cast in the following

form

$$\dot{\Phi} = \frac{\alpha}{A^{\frac{1}{2}}B}\Pi, \tag{2.22}$$

$$\dot{\Psi} = \partial_r\left(\frac{\alpha}{A^{\frac{1}{2}}B}\Pi\right), \tag{2.23}$$

$$\dot{\Pi} = \frac{1}{r^2}\partial_r\left(\frac{\alpha B r^2}{A^{\frac{1}{2}}}\Psi\right) + \frac{\alpha A^{\frac{1}{2}}}{r^2}\Big[\frac{1}{\sin\theta}\partial_\theta(\sin\theta\partial_\theta\Phi) + \frac{1}{\sin\theta^2}\partial_\varphi\partial_\varphi\Phi\Big]. \tag{2.24}$$

As for the metric fields, the relevant components of the Einstein equations are the following:

$$G^r{}_t = -\frac{\alpha j_A}{AM_P^2}, \tag{2.25}$$

$$G^t{}_t = -\frac{1}{M_P^2}\big(\rho + \Lambda\big), \tag{2.26}$$

$$G^r{}_r = \frac{1}{M_P^2}\big(S_A - \Lambda\big), \tag{2.27}$$

$$G^\theta{}_\theta = \frac{1}{M_P^2}\big(S_B - \Lambda\big). \tag{2.28}$$

where the first two equations are constraint equations, *i.e.,* Eq. (2.8) and Eq. (2.9), and the latter two are evolution equations of our chosen dynamical fields. For $A(t,r)$, $B(t,r)$ and $D_B(t,r)$, their evolution equations can be found straightforwardly by simply using their definitions:

$$\dot{A} = -2\alpha A(K - 2K_B), \tag{2.29}$$

$$\dot{B} = -2\alpha B K_B, \tag{2.30}$$

$$\dot{D}_B = -2\partial_r(\alpha K_B). \tag{2.31}$$

The evolution of the gauge degrees of freedom $\alpha(t,r)$ and $D_\alpha(t,r)$ are to be chosen

by hand, that is, by imposing the following slicing conditions

$$\dot{\alpha} = -\alpha^2 f(\alpha) K, \tag{2.32}$$

$$\dot{D}_\alpha = -\partial_r(\alpha f(\alpha) K), \tag{2.33}$$

I will work in 1+log gauge throughout, for which I choose $f(\alpha) = 2/\alpha$. To find the evolution equations of $K(t,r)$ and $K_B(t,r)$, the Einstein equations have to be used. The equation of motion for $K_B(t,r)$ is derived by combining the $G^r{}_r$ and $G^t{}_t$ components, which gives

$$\begin{aligned}\dot{K}_B = &\frac{\alpha}{Ar}\Big[\frac{1}{2}\tilde{U} + \frac{2\lambda B}{A} - D_B - \lambda - D_\alpha\Big] \\ &+ \frac{\alpha}{A}\Big[-\frac{1}{2}D_\alpha D_B - \frac{1}{2}D_B' + \frac{1}{4}D_B\Big(\tilde{U} + \frac{4\lambda B}{A}\Big) + AKK_B\Big] \\ &+ \frac{\alpha}{2M_P^2}(S_A - \rho - \Lambda).\end{aligned} \tag{2.34}$$

For the evolution of K, the equations for $G^r{}_r$, $G^t{}_t$ and $G^\theta{}_\theta$ can be used to find

$$\begin{aligned}\dot{K} = &\alpha(K^2 - 4KK_B + 6K_B^2) \\ &- \frac{\alpha}{A}\Big[D_\alpha' + D_\alpha^2 + \frac{2D_\alpha}{r} - \frac{1}{2}D_\alpha\Big(\tilde{U} + \frac{4\lambda B}{A}\Big)\Big] \\ &+ \frac{\alpha}{2M_P^2}(\rho + S_A + 2S_B - 2\Lambda).\end{aligned} \tag{2.35}$$

For λ, using its definition, one can get

$$\dot{\lambda} = \frac{2\alpha A}{B}\frac{(K - 3K_B)}{r}, \tag{2.36}$$

which is well defined in the continuum limit. However, the $1/r$ factor on the right hand side makes this evolution equation numerically highly unstable when discretising the equation and putting it on a lattice. To overcome this problem, the momentum constraint (2.8) can be used to remove this factor and one arrives

at

$$\dot{\lambda} = \frac{2\alpha A}{B}\Big[K'_B - \frac{1}{2}D_B(K - 3K_B) + \frac{j_A}{2M_P^2}\Big]. \tag{2.37}$$

Note that other $1/r$ terms in the evolution equations (such as in Eq. (2.24)) are automatically regular by demanding the dynamical variables to be symmetric or antisymmetric. However here, in Eq. (2.36), the combination of $(K-3K_B)/r$ must be regular. Analytically, this is true since the local flatness condition $A(t, r = 0) = B(t, r = 0)$ means also that $K_A(t, r = 0) = K_B(t, r = 0)$, hence $K(t, r = 0) = 3K_B(t, r = 0)$. Numerically, on the other hand, small errors can spoil this cancellation hence making the term unstable. Thus the need to make it regular by using the momentum constraint.

Similarly, using its definition and the Hamiltonian constraint Eq. (2.9), the evolution for $\tilde{U}$ can be found to be

$$\begin{aligned}\dot{\tilde{U}} = &-2\alpha\Big[K' + D_\alpha(K - 4K_B) - 2(K - 3K_B)\Big(D_B - \frac{2\lambda B}{A}\Big)\Big] \\ &- 4\alpha\frac{j_A}{M_P^2}.\end{aligned} \tag{2.38}$$

This completes the derivation of the evolution equations for our dynamical variables, which, unlike the original Einstein equations or even the ADM decomposed version, are generally well behaved numerically after discretisation.

2.2.4 Initial conditions

To evolve the system, some initial conditions must be chosen. Some care must be taken for a system with gauge degrees of freedom, in which case some of the equations of motion are actually constraint equations. I follow a free evolution scheme in which the constraints are solved once initially when preparing the initial data. Then the keeping of the constraint equations can be used to monitor how well the simulation works.

For the matter fields, I choose the initial conditions to be

$$\Phi^0 = g(r), \quad \Psi^0 = g'(r), \quad \Pi^0 = 0. \tag{2.39}$$

where here the superscript 0 denotes the initial condition of the corresponding quantity at $t = 0$. A natural choice for my purposes is to take the function $g(r)$ to be a Gaussian wave packet. In my simulations, I use the following family of functions

$$g(r) = a \exp\left[-(r/D)^2\right], \tag{2.40}$$

where a is the amplitude and D the width of the wave packet. Note that the above definition of $g(r)$ ensures that the initial scalar field is an even function, and thus all initial $1/r$ terms in the equations of motion are regular. The initial conditions for the gravity fields are chosen to be

$$\begin{aligned} K^0 &= K_B^0 = 0, \\ \alpha^0 &= B^0 = 1, \\ D_\alpha^0 &= D_B^0 = 0 \end{aligned} \tag{2.41}$$

such that they solve the constraint equations. Note that the choice $\Pi^0 = 0$ is convenient, since then one has $j_A^0 = 0$, which means that the momentum constraint in Eq. (2.8) is automatically solved by the choices $K^0 = K_B^0 = 0$. The initial conditions for the other gravity fields require some calculations. To do this, I first take $A^0(r = 0) = 1$, and integrate out the following equation to find the $A^0(r)$ function,

$$\partial_r A^0 = A^0\Big(\frac{1}{r}(1 - A^0) + \frac{r}{2M_P^2}(\Psi^0)^2 + \frac{rA^0}{M_P^2}\Lambda\Big), \tag{2.42}$$

which comes from the Hamiltonian constraint along with the initial condition

$\rho^0 = (\Psi^0)^2/(2A^0)$. Then to find λ^0 and $\tilde{U}^0$, I use their definitions along with A^0:

$$\begin{aligned} \lambda^0 &= \frac{1}{r}\Big(1 - \frac{A^0}{B^0}\Big), \\ \tilde{U}^0 &= \frac{A^{0\prime} - 4\lambda^0}{A^0}. \end{aligned} \tag{2.43}$$

Thus I have initial conditions for all classical dynamical variable fields. This completes the setup for the classical gravitational collapse in spherical symmetry, which provides the base framework for the quantum/semi-classical simulations. I will run the classical simulations along with the semi-classical ones for a comparison later. Before that, in the following, I shall first set up our formalism to simulate quantum fields on curved space.

2.3 Equal time quantisation

The goal is to develop a semiclassical simulation scheme where the metric fields are still treated classically, but the matter fields can be consistently treated as quantum fields. This is a valid approach in situations where the quantum effects of the matter fields have become important but the quantum gravity effects have yet to kick in. Thus, it is only the classical scalar field that needs to be promoted to be a quantum scalar field. To this end, the c-number Φ needs to be upgraded to an operator $\hat{\Phi}$, and its equation of motion is treated as an operator equation. One can not directly simulate the operator equation, but once $\hat{\Phi}$ is expanded in terms of creation and annihilation operators, the $\hat{\Phi}$ operator equation can be decomposed into the evolution equations for the functions in front of the creation and annihilation operators, the mode functions, which are c-numbers and can be put in a lattice. Of course, the difficulty is that there are infinitely many of these mode functions. Since the classical simulation is spherically symmetric, it is also convenient to further expand the mode functions in terms of the spherical harmon-

ics $Y(\theta, \varphi)$. The feedback of the quantum scalar field to the classical geometry is obtained via the semiclassical Einstein equations, by taking the quantum expectation value of the stress-energy tensor of the scalar field. Explicitly, I will work with the following semiclassical system of equations of motion

$$G_{\mu\nu} = \frac{1}{M_P^2}\Big[\langle\chi|\,\hat{T}_{\mu\nu}\,|\chi\rangle - \Lambda g_{\mu\nu}\Big], \tag{2.44}$$

$$\Box\hat{\Phi} = 0, \tag{2.45}$$

where $\hat{T}_{\mu\nu} = \partial_\mu\hat{\Phi}\partial_\nu\hat{\Phi} - \frac{1}{2}g_{\mu\nu}\big[g^{\rho\sigma}\partial_\rho\hat{\Phi}\partial_\sigma\hat{\Phi}\big]$ and a coherent state will be chosen for the quantum state $|\chi\rangle$.

The key element of this formalism is that, due to a convenient choice of the quantum coherent state, the sources for the Einstein equation can be nicely separated into a classical background plus some quantum fluctuations. This fact allows one to utilise all the existing classical numerical relativity setup, reviewed in the previous section, and simply add the quantum mode functions of the matter fields on top of the simulation of the classical fields. Crucially, though, the scalar field remains fully quantum mechanical.

2.3.1 Quantum scalar field

As mentioned, the real scalar field is now promoted to a Hermitian quantum field operator $\hat{\Phi}$, which can be expanded in spherical mode functions as

$$\hat{\Phi} = \sum_{l,m}\int dk\Big[\hat{a}_{k,l,m}\tilde{u}_{k,l}(t,r)Y_l^m(\theta,\varphi) + \hat{a}^\dagger_{k,l,m}\tilde{u}^*_{k,l}(t,r)Y_l^{m*}(\theta,\varphi)\Big], \tag{2.46}$$

where $Y_l^m(\theta,\varphi)$ are the spherical harmonics and in the following I shall mostly use the mode functions with a factor of r^l stripped off

$$u(t,r) \equiv \frac{\tilde{u}(t,r)}{r^l}. \tag{2.47}$$

For notational simplicity, I have suppressed the k,l indices for u and $\tilde{u}$, and I will also suppress these indices for the π and ψ quantities defined shortly, when not confusing. The $u(t,r) = u_{k,l}(t,r)$'s are the unknown quantities to be solved in my simulations. The operators $\hat{a}_{k,l,m}$ and $\hat{a}^\dagger_{k,l,m}$ are the corresponding ladder operators for each quantum mode denoted by the indices k,l,m. The standard route to quantisation is then to impose the canonical commutation relation between the scalar field and its conjugate momentum

$$\left[\hat{\Phi}(t,\vec{x}), \hat{\Pi}(t,\vec{x}')\right] = i\hbar\delta^3(\vec{x}-\vec{x}'). \tag{2.48}$$

If one requires the mode functions satisfy

$$i\int dr r^2 \left[\tilde{u}^*_{k,l}\partial_t\tilde{u}_{k',l'} - \partial_t\tilde{u}^*_{k,l}\tilde{u}_{k',l'}\right] = \delta(k-k')\delta_{ll'} \tag{2.49}$$

this is equivalent to requiring the ladder operators to obey

$$\left[\hat{a}_{k,l,m}, \hat{a}^\dagger_{k',l',m'}\right] = \hbar c^2\delta_{ll'}\delta_{mm'}\delta(k-k'). \tag{2.50}$$

It is important to emphasize that although the classical geometry is restricted to spherical symmetry, the quantum operators are allowed non-spherical fluctuations. The spherical symmetry is reflected in the quantum state chosen below.

Similar to the classical scalar field, I also define the following variables for the quantum mode functions in order to formulate the evolution equations in a first

order form

$$\pi = \frac{A^{\frac{1}{2}}B}{\alpha}\dot{u}, \qquad \psi = u'. \tag{2.51}$$

I then note that the evolution equations for the mode functions u and ψ are just

$$\dot{u} = \frac{\alpha}{A^{\frac{1}{2}}B}\pi, \tag{2.52}$$

$$\dot{\psi} = \partial_r\left(\frac{\alpha}{A^{\frac{1}{2}}B}\pi\right). \tag{2.53}$$

For the π evolution equation, one can use Eq. (2.46) along with Eq. (2.24) to find that (see Appendix A.1)

$$\dot{\pi} = \partial_r\left(\frac{\alpha B}{A^{\frac{1}{2}}}\right)\left(\frac{l}{r}u+\psi\right) + \frac{\alpha B}{A^{\frac{1}{2}}}\left(\frac{2l+2}{r}\psi+\psi'\right) + \frac{l(l+1)}{r^2}\left(\frac{B}{A}-1\right)A^{\frac{1}{2}}\alpha u, \tag{2.54}$$

which actually carries the real dynamics of the quantum scalar field. The last term in Eq. (2.54) is only strictly regular if $A(t,0) = B(t,0)$. Similar regularity conditions were encountered in the case of the classical collapse as well. There, the use of λ ensured regularity and hence one can use it here as well. Thus, the final dynamical equation to be used for the scalar mode functions is given by

$$\dot{\pi} = \partial_r\left(\frac{\alpha B}{A^{\frac{1}{2}}}\right)\left(\frac{l}{r}u+\psi\right) + \frac{\alpha B}{A^{\frac{1}{2}}}\left(\frac{2l+2}{r}\psi+\psi'\right) + \frac{l(l+1)}{r}\frac{\alpha B}{A^{\frac{1}{2}}}\lambda u. \tag{2.55}$$

I emphasize that here we have suppressed the k, l mode indices for u, ψ and π, that is, the above equation represents an infinite set of c-number equations, which however are decoupled as I work with a free scalar field. To get a good approximation for the quantum scalar field, one should evolve as many of these mode functions as possible, which makes the semiclassical simulations much more expensive computationally than the classical ones.

In order to find suitable initial conditions for the quantum mode functions, let me recall that the equation of motion in Minkowski space for $\Phi^{(M)}$ is $\partial^\mu\partial_\mu\Phi^{(M)} = 0$,

which is solved by

$$\Phi^{(M)} = \frac{k}{\sqrt{\pi\omega}} e^{-i\omega t} j_l(kr), \tag{2.56}$$

with $j_l(kr)$'s being the spherical Bessel functions. This means that the solution for u in Minkowski space is given by

$$u^{(M)} = \frac{k}{\sqrt{\pi\omega}} e^{-i\omega t} \frac{j_l(kr)}{r^l}. \tag{2.57}$$

For simplicity, I shall choose this as our basis of functions at $t = 0$. This entails the following initial conditions at $t = 0$

$$\begin{aligned} u^0 &= \frac{k}{\sqrt{\pi\omega}} \frac{j_l(kr)}{r^l}, \\ \psi^0 &= \frac{k}{\sqrt{\pi\omega}} \left(\frac{j_l'(kr)}{r^l} - \frac{l j_l(kr)}{r^{l+1}} \right), \\ \pi^0 &= -i\omega \frac{k}{\sqrt{\pi\omega}} \frac{j_l(kr)}{r^l}, \end{aligned} \tag{2.58}$$

since initially I have $A = B = \alpha = 1$.

2.3.2 Coherent state

After setting up the evolution of the field operators, one also needs to specify the quantum state of a system. I choose the quantum state to be a spherically symmetric coherent state

$$|\chi\rangle = \exp\left\{ -\frac{1}{2} \frac{1}{\hbar c^2} \int dk |z(k)|^2 \right\} \exp\left\{ \frac{1}{\hbar c^2} \int dk z(k) \hat{a}^\dagger_{k,0,0} \right\} |0\rangle \,, \tag{2.59}$$

which is an eigenstate of the lowering operator, $\hat{a}_{k,0,0} |\chi\rangle = z(k) |\chi\rangle$, and $\hat{a}_{k,l,m}|0\rangle = 0$. The first exponential in the $|\chi\rangle$ definition above is fixed by normalisation $\langle\chi|\chi\rangle = 1$. Coherent states are known to be useful to connect quantum systems to classical ones, and they are "minimal uncertainty states" (see *e.g.* [59]), which are

in a sense "the closest to the classical limit". This specific choice of the quantum state will be crucial in this formalism, and it will allow for a direct comparison between the semiclassical collapse and classical collapse. It is worth pointing out that the state I am considering is an eigenstate of the initial lowering operator, and that in the Heisenberg picture, where operators evolve, the state need not be an eigenstate of the time-evolved lowering operator. This, however, is not a factor in the simulations performed.

The expectation value of the quantum scalar field operator in the chosen coherent state is defined to be

$$\phi(t,r) \equiv \langle\chi|\,\hat{\Phi}(t,r)\,|\chi\rangle\,. \tag{2.60}$$

which is often called the "classical field". Indeed, one may identify it with the scalar field in the classical gravitational collapse. To see this, note that, making use of the coherent state definition $\hat{a}_{k,l,m}\,|\chi\rangle = \delta_{l,0}\delta_{m,0}z(k)\,|\chi\rangle$, one can get

$$\phi(t,r) = \frac{1}{2\sqrt{\pi}}\int dk[z(k)\tilde{u}_{k,0}(t,r) + h.c.]. \tag{2.61}$$

where *h.c.* stands for the Hermitian conjugate of the previous terms and the fraction is due to the fact that $Y_0^0 = 1/2\sqrt{\pi}$. By the evolution equation of the mode function $\tilde{u}_{k,0}(t,r)$, one can see that this expectation value $\phi(t,r)$ satisfies the same equation of motion as the classical scalar field in Section 2.2. Hence the coherent state choice allows me to separate the classical and quantum contributions in the stress-energy tensor, which is crucial to tap into the established methods to simulate classical gravitational collapse. Note that this is also a consequence of the fact that the theory at hand is a free theory - this separation would not happen if a theory with interactions was considered. This is discussed in the next subsection.

2.3.3 Quantum stress-energy tensor

By virtue of the chosen coherent state above, and the fact that our theory is free, the objects appearing in the stress-energy tensor automatically separate into a sum of contributions from the coherent state expectation value $\phi(t,r)$, which only involves the spherically symmetric mode function $\tilde{u}_{k,0}(t,r)$, and contributions from the mode functions $\tilde{u}_{k,l}(t,r)$. Specifically, using Eq. (2.46), the choice of the quantum coherent state Eq. (2.59) and some identities for the spherical harmonics, it is straightforward to find that the expectation values for the bilinears appearing in the relevant stress-energy tensor components are

$$\langle\chi|\,\hat{\Phi}\hat{\Phi}\,|\chi\rangle = \partial_t\phi\partial_t\phi + \frac{\hbar c^2}{4\pi}\int dk\sum_{l=0}^{N_l-1}(2l+1)|\tilde{u}_{k,l}|^2, \tag{2.62}$$

$$\langle\chi|\,\partial_t\hat{\Phi}\partial_t\hat{\Phi}\,|\chi\rangle = \partial_t\phi\partial_t\phi + \frac{\hbar c^2}{4\pi}\int dk\sum_{l=0}^{N_l-1}(2l+1)|\partial_t\tilde{u}_{k,l}|^2, \tag{2.63}$$

$$\langle\chi|\,\partial_r\hat{\Phi}\partial_r\hat{\Phi}\,|\chi\rangle = \partial_r\phi\partial_r\phi + \frac{\hbar c^2}{4\pi}\int dk\sum_{l=0}^{N_l-1}(2l+1)|\partial_r\tilde{u}_{k,l}|^2, \tag{2.64}$$

$$\begin{aligned}\langle\chi|\,\frac{\partial_r\hat{\Phi}\partial_t\hat{\Phi}+\partial_t\hat{\Phi}\partial_r\hat{\Phi}}{2}\,|\chi\rangle &= \partial_t\phi\partial_r\phi \\ &\quad+\frac{\hbar c^2}{4\pi}\int dk\sum_{l=0}^{N_l-1}(2l+1)\frac{1}{2}(\partial_r\tilde{u}_{k,l}\partial_t\tilde{u}^*_{k,l}+\partial_t\tilde{u}_{k,l}\partial_r\tilde{u}^*_{k,l}),\end{aligned} \tag{2.65}$$

$$\langle\chi|\,\partial_\theta\hat{\Phi}\partial_\theta\hat{\Phi}\,|\chi\rangle = \frac{\hbar c^2}{4\pi}\int dk\sum_{l=0}^{N_l-1}\frac{1}{2}(l+1)(2l+1)|\tilde{u}_{k,l}|^2, \tag{2.66}$$

$$\langle\chi|\,\partial_\phi\hat{\Phi}\partial_\phi\hat{\Phi}\,|\chi\rangle = \frac{\hbar c^2}{4\pi}\int dk\sum_{l=0}^{N_l-1}\frac{1}{2}(l+1)(2l+1)|\tilde{u}_{k,l}|^2\sin^2\theta. \tag{2.67}$$

where I have explicitly put back the reduced Planck constant $\hbar$ and the speed of light c. In addition, N_l here denotes the number of l-modes. Note that here $\phi(t,r)$ is taken to be the same as the scalar field in the classical gravitational collapse. The fact that the quantum expectation values of these operators separate into the classical coherent part and the extra quantum part is merely due to the choice of

the coherent state. Note that Eqs. (2.66-2.67) contain only quantum fluctuations, as expected, since the classical pieces of those terms do not depend on (θ, ψ). In addition, by setting $\hbar$ to zero, one can readily switch off quantum contributions.

Therefore, in my semiclassical simulations, I shall take the decomposed stress-energy tensor quantities ρ, j_A, S_A and S_B to be

$$\rho = n^\mu n^\nu \langle T_{\mu\nu} \rangle = \frac{1}{2A}\left(\frac{\langle \hat{\Pi}^2 \rangle}{B^2} + \langle \hat{\Psi}^2 \rangle \right) + \frac{1}{Br^2} \langle (\partial_\theta \hat{\Phi})^2 \rangle - \frac{1}{2}\mu^2 \langle \hat{\Phi}^2 \rangle, \tag{2.68}$$

$$j_A = -n^\mu \langle T_{\mu r} \rangle = -\frac{\langle \hat{\Pi}\hat{\Psi} \rangle}{A^{\frac{1}{2}} B}, \tag{2.69}$$

$$S_A = \gamma^{rr} \langle T_{rr} \rangle = \frac{1}{2A}\left(\frac{\langle \hat{\Pi}^2 \rangle}{B^2} + \langle \hat{\Psi}^2 \rangle \right) - \frac{1}{Br^2} \langle (\partial_\theta \hat{\Phi})^2 \rangle - \frac{1}{2}\mu^2 \langle \hat{\Phi}^2 \rangle, \tag{2.70}$$

$$S_B = \gamma^{\theta\theta} \langle T_{\theta\theta} \rangle = \frac{1}{2A}\left(\frac{\langle \hat{\Pi}^2 \rangle}{B^2} - \langle \hat{\Psi}^2 \rangle \right) - \frac{1}{2}\mu^2 \langle \hat{\Phi}^2 \rangle, \tag{2.71}$$

where I have defined $\langle \hat{O} \rangle \equiv \langle \chi | \, \hat{O} \, | \chi \rangle$ and used the following relations for the dynamical fields

$$\begin{aligned} &\langle \hat{\Phi}^2 \rangle = \langle \hat{\Phi}\hat{\Phi} \rangle, \quad \langle \hat{\Pi}^2 \rangle = \frac{AB^2}{\alpha^2} \langle \partial_t \hat{\Phi} \partial_t \hat{\Phi} \rangle, \quad \langle \hat{\Psi}^2 \rangle = \langle \partial_r \hat{\Phi} \partial_r \hat{\Phi} \rangle, \\ &\langle \hat{\Pi}\hat{\Psi} \rangle = \frac{1}{2} \frac{A^{\frac{1}{2}} B}{\alpha} \langle \partial_r \hat{\Phi} \partial_t \hat{\Phi} + \partial_t \hat{\Phi} \partial_r \hat{\Phi} \rangle, \quad \langle (\partial_\theta \hat{\Phi})^2 \rangle = \langle \partial_\theta \hat{\Phi} \partial_\theta \hat{\Phi} \rangle. \end{aligned} \tag{2.72}$$

2.3.4 Regularisation

The semiclassical Eq. (2.44) needs regularisation, since the quantum expectation values on the right hand side diverge, which manifests itself as the infinite sums over the mode functions appearing in Eqs. (2.62-2.67). In my lattice simulations, these divergences appear as large, unphysical numbers in the evolution equations that need to be regularised, as is to be expected for a quantum field theory. Note that regularising is the process of casting these divergent sums to finite values, which then enables us to calculate renormalised physical quantities, like the stress-energy tensor components or correlation functions. In a lattice simulation

the popular regularisation scheme used in analytic perturbative computations, dimensional regularisation, can not be used. In general, dimensional regularisation is useful because it maintains all the symmetries of a theory, including Lorentz symmetry. So if dimensional regularisation were to be used, the introduced bare cosmological constant Λ would be sufficient to regularise the UV divergences in Eq. (2.44). However, the finite number of modes (or lattice points) used in a numerical scheme necessarily breaks Lorentz invariance, which means that the UV divergences can not be cancelled by a simple cosmological constant counter term. (In other words, Lorentz invariance is not a symmetry of a lattice field theory, which has a built-in hard cutoff, and in a regularization scheme with a hard cutoff, the UV divergences in Eq. (2.44) are not proportional to $\eta_{\mu\nu}$.) Instead, I shall introduce Pauli-Villars fields [60] to cancel the various divergences that appear. As one shall see, I need to introduce several Pauli-Villars fields to achieve our goal. This is because while one Pauli-Villars ghost field would eliminate the original divergences in Eq. (2.44), it also introduces some less severe divergences, which need to be balanced/canceled by introducing extra Pauli-Villars fields.

The Pauli-Villars regularisation scheme consists of adding some extra auxiliary (ghost) fields to the physical one, which by construction cancel the UV divergences. This happens by giving the ghost terms in the Lagrangian the appropriate signs, so that the divergences disappear in the stress-energy tensor. These ghost fields must have larger masses than the physical field, in order to only influence the UV physics. The ghost fields are chosen also to cancel each others' contributions to the various divergences.

Note that even though the quantum field will live on a curved spacetime, it is sufficient to fix the masses of the ghosts by first regularising in Minkowski spacetime. This is because the divergences are UV in nature, hence short distance. In short distances, due to local flatness, the Minkowski space approximation still holds. Thus, once the UV divergences are fixed in Minkowski, they are cured on curved

spacetimes as well.

To illustrate the divergences involved in the system, let me take a massless scalar field in Minkowski spacetime. The Lagrangian is just

$$\mathcal{L} = \frac{1}{2}\int d^4x\Big[-\frac{1}{2}\partial_\mu\Phi\partial^\mu\Phi\Big]. \tag{2.73}$$

This scalar field may be expanded in terms of mode functions similarly as in Eq. (2.46). Then, the energy density and pressure for the field can be found to be [61]

$$\begin{aligned}\varrho &= \frac{1}{4\pi^2}\int_0^{\mathcal{M}} k^3 dk,\\ P &= \frac{1}{4\pi^2}\int_0^{\mathcal{M}} \frac{k^3}{3} dk,\end{aligned} \tag{2.74}$$

where k is just the wave number and a cut-off $\mathcal{M}$ has been introduced. These integrals are straightforwardly evaluated to be

$$\varrho = \frac{1}{16\pi^2}\mathcal{M}^4, \tag{2.75}$$

$$P = \frac{1}{16\pi^2}\frac{1}{3}\mathcal{M}^4. \tag{2.76}$$

One can see that these terms are divergent, and need to be regularised. The introduction of a bare cosmological constant Λ, which is equivalent to the normal ordering for the quantum fields, can only cancel divergences of the form $\varrho_{vac} = -P_{vac}$, and so is not able to cure the divergence in Eqs. (2.75-2.76), which does not satisfy the equation of state of vacuum energy.

Thus, one needs to introduce Pauli-Villars ghost fields to cancel the divergent density and pressure contributions in Eqs. (2.75-2.76). Let me introduce one ghost field $\mathcal{G}_1$ with mass m_1 (which is non-zero) and observe how it changes these expressions. The ghost field is introduced in the Lagrangian with opposite sign

kinetic and mass terms, so that

$$\mathcal{L} = \frac{1}{2}\int d^4x \Big[-\frac{1}{2}\partial_\mu\Phi\partial^\mu\Phi + \frac{1}{2}\partial_\mu\mathcal{G}_1\partial^\mu\mathcal{G}_1 + \frac{1}{2}m_1^2\mathcal{G}_1^2\Big]. \tag{2.77}$$

Then, the energy density and pressure for the system is

$$\begin{aligned} \varrho_{total} &= \frac{1}{4\pi^2}\int_0^{\mathcal{M}} \Big[k^3 - k^2\sqrt{k^2+m_1^2}\Big]dk, \\ P_{total} &= \frac{1}{4\pi^2}\int_0^{\mathcal{M}} \Big[\frac{k^3}{3} - \frac{k^4}{3\sqrt{k^2+m_1^2}}\Big]dk. \end{aligned} \tag{2.78}$$

Hence the large $\mathcal{M}$ expansion of these integrals is modified to be

$$\begin{aligned} \varrho_{total} = \frac{1}{16\pi^2}\Bigg[&\cancel{\Big(\mathcal{M}^4 - \mathcal{M}^4\Big)} - m_1^2\mathcal{M}^2 \\ &- \frac{1}{2}m_1^4\ln\Big(\frac{m_1}{\mathcal{M}}\Big) - \frac{1}{8}(1-4\ln(2))m_1^4 + \mathcal{O}\Big(\frac{m_1^6}{\mathcal{M}^2}\Big)\Bigg], \end{aligned} \tag{2.79}$$

$$\begin{aligned} P_{total} = \frac{1}{16\pi^2}\Bigg[&\cancel{\Big(\frac{1}{3}\mathcal{M}^4 - \frac{1}{3}\mathcal{M}^4\Big)} + \frac{1}{3}m_1^2\mathcal{M}^2 \\ &+ \frac{1}{2}m_1^4\ln\Big(\frac{m_1}{\mathcal{M}}\Big) + \frac{1}{24}(7-12\ln(2))m_1^4 + \mathcal{O}\Big(\frac{m_1^6}{\mathcal{M}^2}\Big)\Bigg]. \end{aligned} \tag{2.80}$$

The original divergence coming from the physical field is cancelled, however, due to the nonzero mass of the ghost field, there are new, quadratic, divergences introduced. In addition, now there are finite terms in the expansions from the ghost field, which are unphysical. Therefore, both the new divergences and the finite ghost contributions need to be cancelled.

Notice that the third terms in Eqs. (2.79-2.80) can be cancelled by the cosmological

constant Λ, so that

$$\varrho_{total} = \frac{1}{16\pi^2}\Bigg[\cancel{\Big(\mathcal{M}^4 - \mathcal{M}^4\Big)} - m_1^2\mathcal{M}^2 + \cancel{\Big[\frac{1}{2}m_1^4\ln\Big(\frac{m_1}{\mathcal{M}}\Big) + \Lambda\Big]} - \frac{1}{8}(1-4\ln(2))m_1^4 + \mathcal{O}\Big(\frac{m_1^6}{\mathcal{M}^2}\Big)\Bigg], \tag{2.81}$$

$$P_{total} = \frac{1}{16\pi^2}\Bigg[\cancel{\Big(\frac{1}{3}\mathcal{M}^4 - \frac{1}{3}\mathcal{M}^4\Big)} + \frac{1}{3}m_1^2\mathcal{M}^2 - \cancel{\Big[\frac{1}{2}m_1^4\ln\Big(\frac{m_1}{\mathcal{M}}\Big) + \Lambda\Big]} + \frac{1}{24}(7-12\ln(2))m_1^4 + \mathcal{O}\Big(\frac{m_1^6}{\mathcal{M}^2}\Big)\Bigg]. \tag{2.82}$$

However, one is left with the quadratic divergences (the second terms) and the unphysical finite ghost contributions (the fourth terms). To cancel these, one needs to introduce more Pauli-Villars fields. On the other hand, to make sure that the first terms in Eqs. (2.81-2.82) keep being cancelled, one needs a total number of fields that is even and therefore two Pauli-Villars fields will not suffice. Note that the third terms will be cancelled by the cosmological constant no matter the number of Pauli-Villars fields.

Hence, one needs to introduce at least three Pauli-Villars fields $\mathcal{G}_1, \mathcal{G}_2$ and $\mathcal{G}_3$, with masses m_1, m_2 and m_3. To cancel the $\mathcal{M}^4$ terms, one simply uses the opposite sign for the kinetic and mass terms in the Lagrangian for two of them, e.g. $\mathcal{G}_1$ and $\mathcal{G}_3$. To cancel the m^4 and $m^2\mathcal{M}^2$ contributions, the masses must obey the equations

$$\begin{aligned} m_2^2 &= m_1^2 + m_3^2, \\ m_2^4 &= m_1^4 + m_3^4. \end{aligned} \tag{2.83}$$

The solutions to this set of equations always involve m_1 or m_3 being zero. However, the Pauli-Villars masses must be larger than the physical mass, and therefore these are not suitable solutions. In order to obtain a set of masses that are nonzero, two more Pauli-Villars fields have to be introduced, $\mathcal{G}_4$ and $\mathcal{G}_5$, with $\mathcal{G}_5$ having the

opposite sign kinetic and mass terms. Thus, the masses must obey

$$\begin{aligned} m_2^2 + m_4^2 &= m_1^2 + m_3^2 + m_5^2, \\ m_2^4 + m_4^4 &= m_1^4 + m_3^4 + m_5^4. \end{aligned} \tag{2.84}$$

There are many solutions to this set of equations, and I choose the following:

$$m_2 = \sqrt{3}m_1, \quad m_3 = m_1, \quad m_4 = \sqrt{3}m_1, \quad m_5 = \sqrt{4}m_1. \tag{2.85}$$

Therefore, using five Pauli-Villars fields with the above particular masses, the system is regularised. Note that, together with the physical field, this means one has to evolve six dynamical quantum fields now. The Lagrangian for the full regularised semiclassical system is then:

$$\mathcal{L} = \frac{1}{2}\int d^4x\sqrt{-g}\Big[M_P^2\frac{R}{2} - \Lambda_{ct} - \frac{1}{2}\partial_\mu\Phi\partial^\mu\Phi - \sum_{i=1}^{5}(-1)^i\Big(\frac{1}{2}\partial_\mu\mathcal{G}_i\partial^\mu\mathcal{G}_i + \frac{1}{2}m_i^2\mathcal{G}_i^2\Big)\Big], \tag{2.86}$$

where now three ghost fields (with $i = 1, 3, 5$) have opposite sign kinetic and mass terms. In addition the cosmological constant term has a "ct" subscript to emphasise that it is merely a counter term, rather than a physical constant in the system. Hence, the system with the Lagrangian in Eq. (2.86) produces regularised stress-energy tensor components and so the expressions in Eqs. (2.68-2.71) will also be finite.

For the specific value of the cosmological constant counter term, one can find an exact analytical value by performing the integrals of the stress energy tensor components. This is detailed in Appendix A.2, and, setting the mass of the lightest Pauli-Villars field $M_{PV} = m_1$, the final value of the cosmological constant counter term is:

$$\Lambda_{ct} = \frac{M_{PV}^4}{(2\pi)^2}\frac{1}{8}\ln\left(\frac{3^9}{2^{16}}\right). \tag{2.87}$$

2.4 Simulation setup

The coupled system of the quantum field plus gravity is solved numerically by discretising the spacetime and putting the equations on a lattice. In this section, the numerical scheme of the spacetime grid is presented along with techniques to solve the discretised system. A subsection is also devoted to the initialisation of the quantum field, which involves choosing a specific number of quantum modes that build up the full quantum operator. It is illustrated how the stress-energy tensor components change for different numbers of modes.

2.4.1 Numerical methods

In the simulation I use a uniform spatial grid consisting of 500 points with $dr = 0.025$ and $dt = dr/4$. For spatial derivatives, tenth order finite difference methods are used, and similarly a tenth order implicit Runge-Kutta method [62] is used for time integration. Such high order numerical methods are necessary due to the evolution equations, such as Eq. (2.54), containing terms involving the $1/r$ and/or $1/r^2$ factor, which are numerically unstable due to the coordinate singularity at $r = 0$ if not treated carefully.

To this end, one also needs to use some artificial dissipation, which acts as damping for the numerical errors. In my code, this is done by adding Kreiss-Oliger terms [63] to the evolution equation of each field. For example, for $\phi(t, r)$, at time step n with the original evolution step denoted schematically by $G(\phi^n)$, ϕ at the next time step would be calculated by

$$\phi^{n+1} = \phi^n + dt\ G(\phi^n). \tag{2.88}$$

Then, adding the extra dissipation term, the evolution equation $G(\phi^n)$ is modified

as

$$G(\phi^n) \longrightarrow G'(\phi^n) = G(\phi^n) - \epsilon(-1)^N dr^{2N-1}\partial_r^{2N}\phi^n, \tag{2.89}$$

where ϵ is a positive constant which is smaller than one, and $2N$ is the order of dissipation, and is an integer. This added term essentially damps the modes with wavelength close to the grid spacing dr.

In order to preserve the tenth order accuracy of the system, the dissipation term must be at least twelfth order. Even though the accuracy of the system is maintained to be high, in my experience the simulation is more robust when lower order dissipation is used. Thus, following Alcubierre's notation [57], the Kreiss-Oliger term is fourth order with $\epsilon = 0.5$ for the quantum mode functions and $\epsilon = 0.1$ for the metric fields and $\phi(t, r)$. Thus, I use the tenth order methods to stabilise the evolution around $r = 0$, but the overall accuracy is second order, which is sufficient for my purposes.

The semiclassical simulation starts with the initial conditions described in subsection 2.2.4 with the coherent state expectation value of the quantum field replacing the classical scalar field. In addition, the initial quantum mode functions are described in Eqs. (2.58). I also run the classical simulation with the same initial conditions for a comparison. I solve the constraint equations only once at $t = 0$ and then use the Hamiltonian constraint to monitor the accuracy of the simulations.

Note that the accuracy and stability of the system are dependent on the initial coherent state expectation value of the quantum field. This is parameterised by the Gaussian configuration parameters a, D. In terms of stability, the most sensitive part of the simulation is the quantum mode functions, specifically the mode functions with high l values. These dynamical variables have the highest tendency to develop instabilities at the origin. Even though both the spatial derivatives and time iteration method are tenth order and dissipation is added

artificially to the system, instabilities still arise for l modes, which limits the number of l modes that can be added to achieve a better simulation. The artificial dissipation, on the other hand, greatly delays the appearance of the instabilities.

One also needs to choose numerical parameters for the mode functions and the integrals, appearing in the stress-energy tensor components, that become discrete sums. Firstly, the mass m_1 of the ghost field $\mathcal{G}_1$ must be chosen, which is simply taken to be $m_1 = 1.0$ in Planck units through my simulations. Crucially, this needs to be larger than the energy of the initial scalar field, which is satisfied by the above mentioned initial conditions. In addition, the continuous integrals of the mode functions over k, in e.g. Eqs. (2.62), must be numerically approximated. To this end, a minimum wave number k_{min} is chosen, which will then be the minimal step between wave numbers $dk = k_{min}$, and the integrals over k then become summations multiplied by dk. In my simulations I choose $k_{min} = \pi/15$ throughout. Lastly, one needs to choose a finite number of mode functions to involve in the simulation, namely the number of k-modes and l-modes, which will be denoted by N_l and N_k respectively. This will be discussed in the next subsection.

2.4.2 Vacuum

As mentioned, a crucial choice in the system is the number of quantum modes $\tilde{u}_{k,l}$ used, which essentially defines the quantum field operator. In practice, one can only use a finite number of quantum modes and generally the more quantum modes one uses, the better simulated the quantum operator is. I find that the maximum number of quantum modes one can use is $N_l = N_k = 150$ in my current numerical setup. This limit arises from the amplitude of the modes becoming too small, saturating the double precision limit of the simulations.

Due to the finite amount of mode functions, the quantum field is well-defined only in a limited spatial region around $r = 0$. In addition, thanks to instabilities from the high k and l valued mode functions, one can simulate the well-defined quantum field only for a finite amount of time also. Hence, there are both spatial and temporal limitations of the simulation. More specifically, for a particular set of initial conditions for the coherent state expectation value, there is a characteristic spatial region where the quantum field is accurately modelled, as well as a characteristic time frame during which all the relevant evolution takes place and through which all evolved mode functions must stay stable. Thus the initial coherent state expectation value must be chosen so that it vanishes outside the region of well-defined quantum field operator, as well as the evolution taking place before the mode functions become unstable. This ensures that everything stays physical in the chosen spatial region and time frame.

Let us discuss the case when the coherent state expectation value is just the vacuum, *i.e.*, $z(k) = 0$. Since the coherent state expectation value does not contain divergences, but only the quantum mode contributions do, if the quantum mode contributions are well-defined, then the full quantum operator is as well. The field operator in the vacuum contains exactly these quantum mode contributions only. Since all stress-energy tensor components need to vanish in a well-defined quantum vacuum, this is a good consistency check. When this is true, I expect that the full quantum field operator is well-defined.

First, as a consistency check, one can analyse the numerical value of the cosmological constant counter term that arises for different number of quantum modes used. In theory, using an infinite number of quantum modes, the value of the cosmological constant counter term is that of Equation 2.87, however, since in numerical settings only finite numbers of quantum modes are available, it won't match exactly. In addition, since the integrals are performed numerically, that also introduces an error between the numerically calculated and analytical values

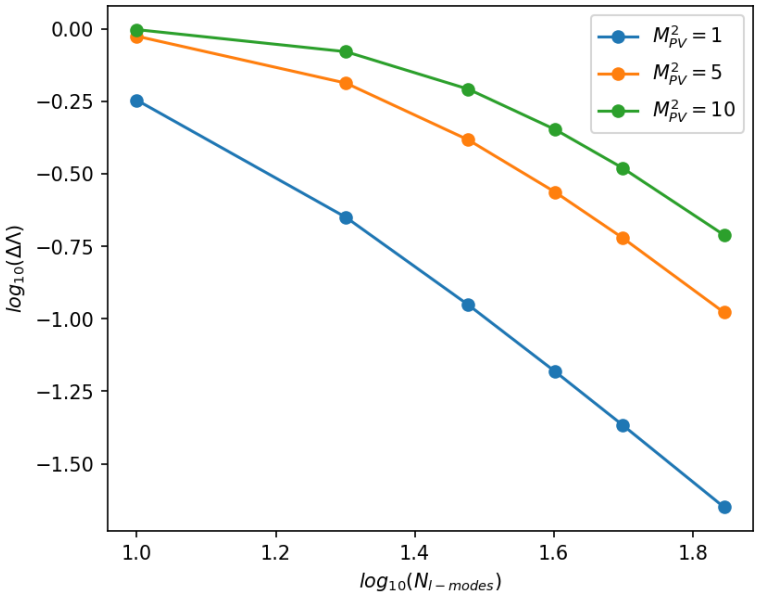

Figure 2.1: Convergence of the cosmological constant counter term calculated numerically to its analytical value for different ghost masses and for various numbers of quantum mode functions included, with equal number of l-modes and k-modes. Here $\Delta\Lambda = \Lambda_{analytical} - \Lambda_{numerical}$, where the counter term subscripts "ct" have been suppressed.

for the cosmological constant counter term. One expects, though, that the more quantum modes one uses, the closer to the analytical value the numerical value would go. A comparison of these two values for different ghost masses is plotted in Figure 2.1 as a function of the number of quantum modes.

As mentioned before, using a larger number of mode functions, one achieves a well-defined quantum vacuum in a larger spatial region. To illustrate this, the stress-energy tensor components, for the case of zero coherent state expectation value, are presented in Figure 2.2 for various numbers of mode functions with $N_k = N_l$. The stress-energy tensor components have been regularised in the previously presented manner. The cosmological constant has been chosen such that the $T^t{}_t$ component is zero at $r = 0$. This is merely an ad-hoc choice, which then introduces a small deviation of the $T^r{}_r$ and $T^\theta{}_\theta$ components from zero, as seen in Figure 2.2. The relative difference between the components is unchanged by the choice of the cosmological constant.

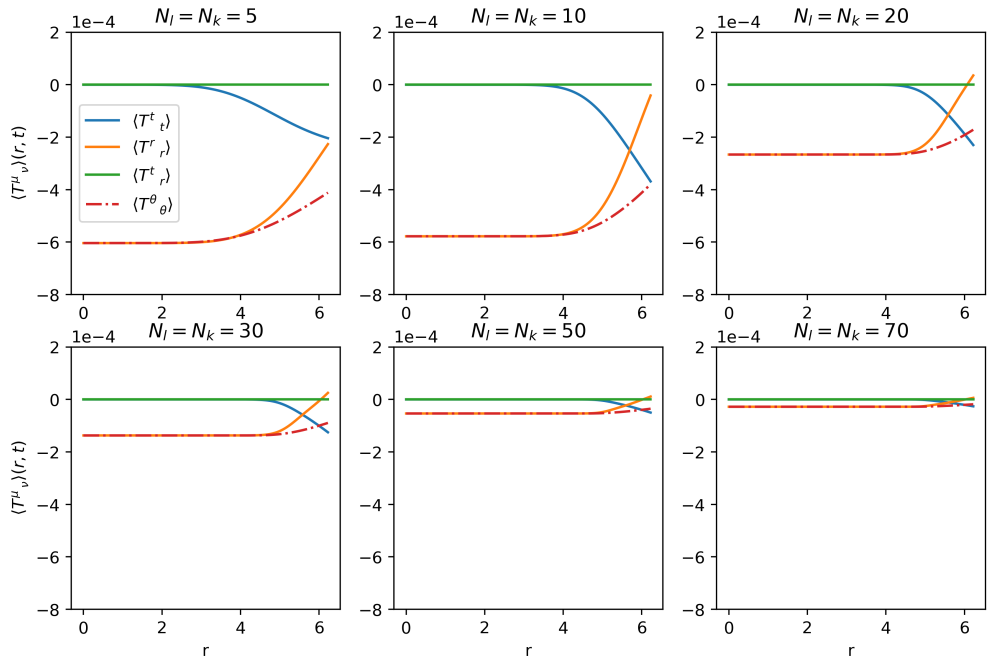

Figure 2.2: Expectation values of the stress-energy tensor components in the case of zero coherent state expectation value for various numbers of quantum mode functions included, with equal number of l-modes and k-modes.

From Figure 2.2, it is evident that more mode functions make a better quantum vacuum. The spatial region in which all stress tensor components (approximately) vanish, is more or less constant, namely when $r < 5$ for the chosen set of initial conditions. The deviation from zero of the $T^r{}_r$ and $T^\theta{}_\theta$ components, on the other hand, greatly decreases as the number of mode functions is increased. This deviation introduces a small systematic error in the simulation, but generally the errors coming from other sources of the full evolution are actually greater than this error.

Another set of plots are shown in Figure 2.3, where the number of l-modes and k-modes are not equal ($N_k \neq N_l$), in order to demonstrate how varying one and holding the other number constant influences the vacuum. Note that in these plots, the spatial region is increased in preferable cases, compared to Figure 2.2, now r stretching out to $r_{max} = 20$. In the first row, N_k is held constant, whilst N_l is increased. The region where the vacuum is well-defined becomes larger

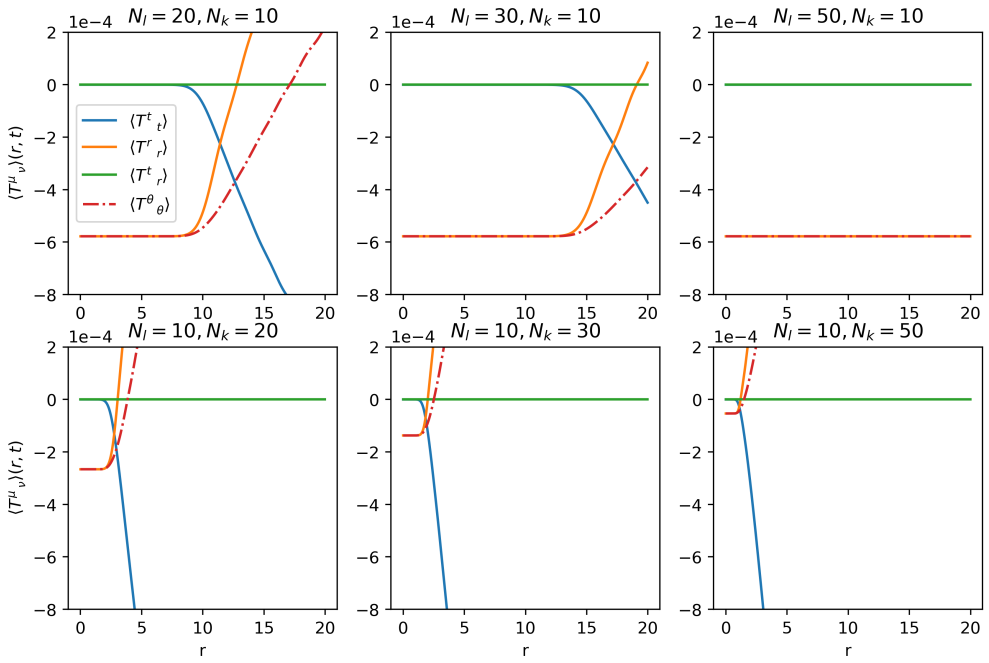

Figure 2.3: Expectation values of stress-energy tensor components in the case of zero coherent state expectation value for various numbers of quantum mode functions, with different numbers of l-modes and k-modes.

as this happens. The relative difference between the components stays constant throughout. In the second row, I hold N_l constant but increase N_k. One sees now that the relative difference between the components decreases, as one adds more k mode functions. Unfortunately, the flat region where the quantum field is well-defined is actually shrinking as well. This is the reason why, in Figure 2.2, even though both the number of l-modes and k-modes are increased, the flat region stays relatively constant.

For my purposes, I have managed to simulate a quantum field with $N_l = N_k = 50$, *i.e.*, 2500 modes, for a sufficiently long time in a sufficiently large spatial region to capture the gravitational collapse to a black hole as well as Choptuik scaling.

Having established the physical region of the quantum field operator, a "good" set of initial conditions for the coherent state expectation value is presented in the next section which vanishes outside the aforementioned spatial region, and its relevant evolution finishes before the mode functions spoil the simulation.

2.5 Results

Once the initial conditions are determined for both coherent state expectation value $\phi(t, r)$ and quantum modes $\tilde{u}_{k,l}$, one is ready to simulate the gravitational dynamics with a quantum field. In this section, results are shown for initial conditions ending up collapsing into a black hole and also dispersing to infinity. In addition, the system is studied close to the critical amplitude in order to demonstrate Choptuik scaling in critical collapse, which is a universal scaling of the resulting black hole's mass as a function of the deviation in the initial pulse's amplitude from the critical amplitude. I also compare with the classical collapse and identify the quantum deviations in these phenomena.

2.5.1 Black hole formation

After establishing that the quantum field is well-defined in a sufficient region around $r = 0$, one can add a nonzero initial coherent state expectation value, and evolve it. The evolution can have two distinct final spacetime structures: Minkowski or Schwarzschild, depending on the initial conditions. I will show the evolution of a chosen initial coherent state expectation value for both cases of black hole formation and no black hole formation.

As discussed, choosing the coherent state expectation value is equivalent to choosing the initial classical scalar configuration. I focus on an initial classical scalar configuration described by Eq. (2.39) and Eq. (2.40) with $D = 1.0$. This initial amplitude can be tuned to achieve an evolution involving a black hole formation or otherwise. For the former case, I can choose $a = 5.0$ and for the latter $a = 1.0$ is a possible choice. Note that these results were obtained using $N_l = N_k = 50$, in other words, 2500 quantum modes. The classical simulations without adding the quantum modes are also performed for a comparison. As expected, for my choices

of initial conditions, the classical simulations are a good approximation of the semiclassical ones. More specifically, the plots presented in Figure 2.4 would be almost indistinguishable from the ones obtained using classical matter. Crucially, though, they are not exactly the same, I will come back to this at the end of this section.

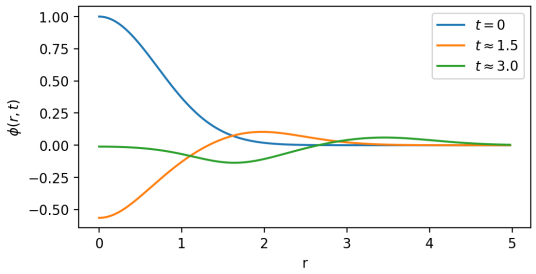

(a) Evolution of $\langle\hat{\Phi}\rangle$ for no gravitational collapse

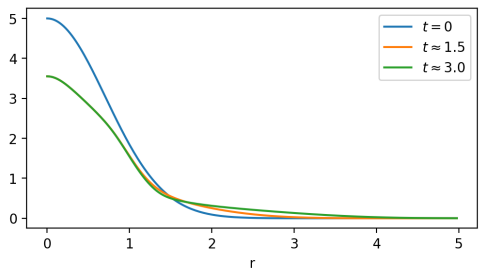

(b) Evolution of $\langle\hat{\Phi}\rangle$ for gravitational collapse

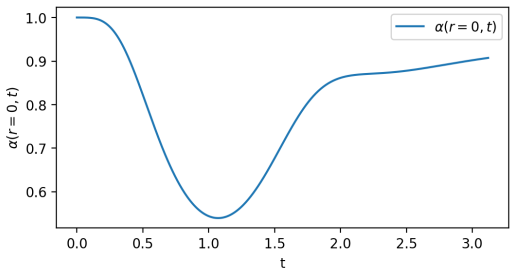

(c) Evolution of $\alpha(r = 0)$ for no gravitational collapse

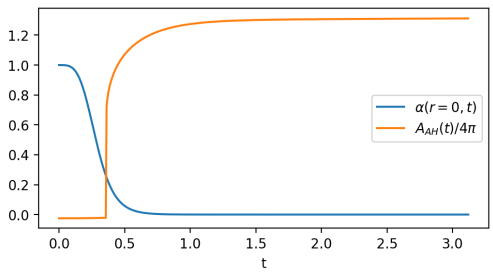

(d) Evolution of $\alpha(r = 0)$ when a black hole does form, along with the evolution of the apparent horizon area.

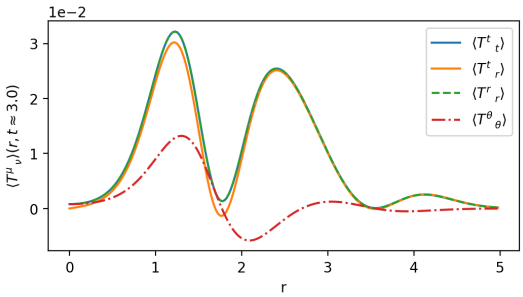

(e) $\langle\hat{T}^\mu{}_\nu\rangle$ at $t \approx 3.0$ when a black hole does not form

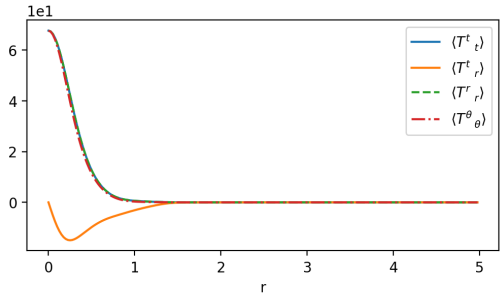

(f) $\langle\hat{T}^\mu{}_\nu\rangle$ at $t \approx 3.0$ when a black hole forms

Figure 2.4: Evolution of centred wave-packets with initial amplitude $a = 1.0$ (left column) and $a = 5.0$ (right column). The latter evolution results in gravitational collapse, which can be seen by the collapse of the lapse $\alpha(t, r = 0)$ and the appearance of an apparent horizon located at r_{AH}.

The results for the two separate simulations are presented in Figure 2.4. The left column corresponds to the case of no black hole formation (subcritical), and the right column to when the quantum field collapses and a black hole forms (supercritical). (The critical case is presented in the next subsection.) The different rows show various quantities relevant to the evolutions. Let us go through these row by row.

The first row shows plots of the coherent state expectation value of the quantum field, namely $\phi(t,r) = \langle\hat{\Phi}\rangle$, at three times: at the very beginning, in the middle of the simulation, and at the end of it. In the case of no black hole formation, one can observe that the initial Gaussian wave-packet immediately starts to drop, after which it propagates outward. In the case of the black hole formation (right column), the wave-packet starts a similar evolution, however, it quickly freezes around $r = 0$ by virtue of the singularity avoiding gauge choice for the lapse function $\alpha(r,t)$. One can observe a small fraction of the wave-packet still escaping, albeit extremely slowly.

The second row shows the evolution of the lapse function at the very centre, $\alpha(0,t)$. This is significant, since the lapse function vanishes if a black hole forms, due to my gauge choice [57]. Thus $\alpha(r,t)$ essentially signals the strength of the curvature at any given point. It is plotted at the centre of the spherically symmetric grid, since that is where $\alpha(r,t)$ first reaches zero in case of gravitational collapse. On the left hand side $\alpha(0,t)$ is plotted when no black hole forms. One can see that at its minimal value it reaches about 0.5-0.6, signalling quite a significant curvature. However, it starts increasing and asymptotically approaches one, in other words, Minkowski spacetime is recovering. The plot on the right hand side, corresponding to the supercritical case, shows the evolution of the central value of the lapse function as well as the area of the appearing apparent horizon. The apparent horizon is found using the vanishing of the outgoing null geodesics Θ, given by

$$\Theta = \frac{1}{\sqrt{A}}\left(\frac{2}{r} + \frac{\partial_r B}{B}\right) - 2K_B, \tag{2.90}$$

where the physical significance of K_B is that it is the (θ,θ) component of the extrinsic curvature. If Θ vanishes for any given r, then there is an apparent horizon located there with radius $r = r_{AH}$ and area $A_{AH} = 4\pi r_{AH}^2\, B|_{r_{AH}}$. Thus, in Figure 2.4 (d), the central value of $\alpha(r,t)$ is plotted along with $A_{AH}/4\pi$. It can be seen

that $\alpha(0,t)$ collapses to zero rather quickly, during which an apparent horizon appears with area $A_{AH}/4\pi \approx 0.8$. The latter then asymptotes to a constant value of $A_{AH}/4\pi \approx 1.25$. The presence of a black hole is unequivocally signalled by these two phenomena; the collapse of the lapse function, and the appearance of an apparent horizon.

The last row in Figure 2.4 shows the expectation value of the stress-energy tensor components in the coherent state at the end of the simulation, at $t = 3.0$. When no black hole forms, as expected, these values are vanishing at $r = 0$ and follow the wave-packets propagating outward. On the other hand, in the supercritical case (right figure), all the components of the stress-energy tensor are centred around $r = 0$, which is again expected, since most of the energy is located in the black hole around the centre. Additionally, note that the stress-energy tensor components are larger by three orders of magnitude in the black hole case compared to the no black hole case.

The same simulations as above was repeated but with initial data that is not centred at $r = 0$. The results for these are plotted in Figure 2.5. The rows and columns correspond to the results of the centred results.

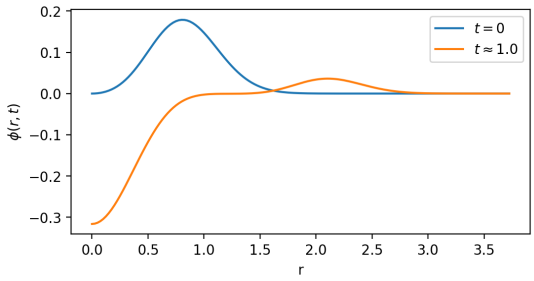

(a) Evolution of $\langle\hat{\Phi}\rangle$ for no gravitational collapse

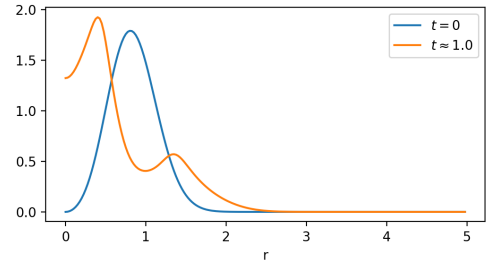

(b) Evolution of $\langle\hat{\Phi}\rangle$ for gravitational collapse

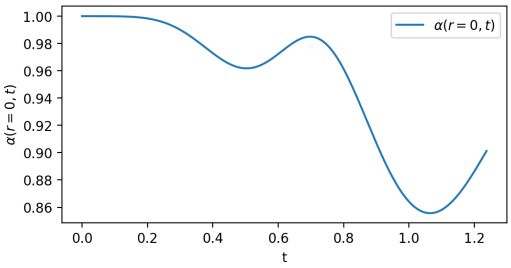

(c) Evolution of $\alpha(r = 0)$ for no gravitational collapse

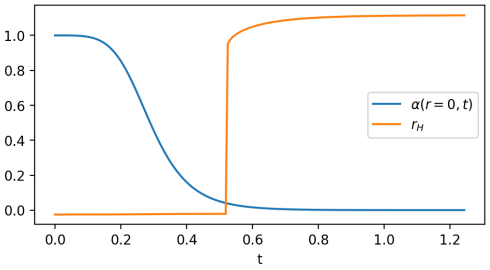

(d) Evolution of $\alpha(r = 0)$ when a black hole does form, along with the evolution of the apparent horizon area.

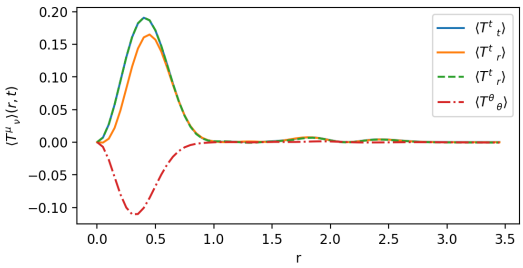

(e) $\langle\hat{T}^\mu{}_\nu\rangle$ at $t \approx 3.0$ when a black hole does not form

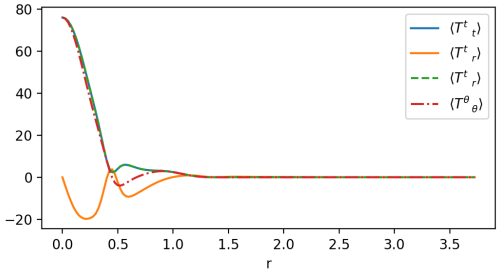

(f) $\langle\hat{T}^\mu{}_\nu\rangle$ at $t \approx 3.0$ when a black hole forms

Figure 2.5: Evolution of non-centred wave-packets with initial amplitude $a = 1.0$ (left column) and $a = 5.0$ (right column). The latter evolution results in gravitational collapse, which can be seen by the collapse of the lapse $\alpha(t, r = 0)$ and the appearance of an apparent horizon located at r_{AH}.

Therefore, one has seen that the simulation goes as expected for both subcritical and supercritical cases, with clear signs of black hole formation in the supercritical case. These plots, however, are very similar when the matter is just classical as well. The obvious step then is to compare some values in the semiclassical simulation to the classical one. As a proxy to measure the quantum effects, I shall plot the differences between the quantum expectation values of the stress-energy

components and the classical stress-energy components:

$$\Delta T^{\mu}{}_{\nu} = \langle T^{\mu}{}_{\nu} \rangle - T^{\mu}_{(c)\ \nu}, \tag{2.91}$$

where $T^{\mu}_{(c)\ \nu}$ corresponds to the purely classical simulation, without any quantum modes added. This is plotted in Figure 2.6. Interestingly, as it can be seen in the figure, the largest quantum effects are cloaked by the horizon of the black hole. Nevertheless, there are some quantum deviations spilling out of the horizon. Also note that even though the quantum field is said to be well defined only until $r = 5$ (visible in Figure 2.2), the quantum mode contributions look flat until around $r = 10$. This is just because the quantum mode contributions diverge after the well-defined region $(0 < r < 5)$ rather slowly.

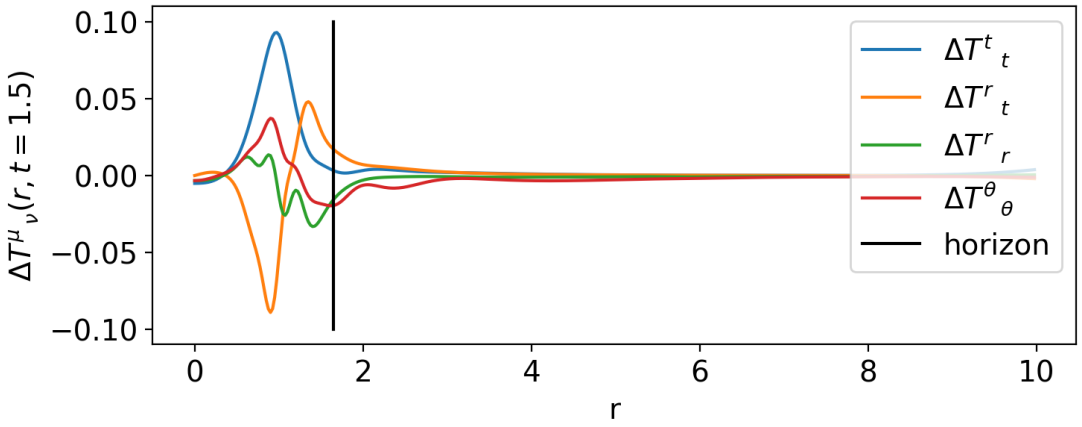

Figure 2.6: Quantum corrections for the stress-energy tensor components $T^{\mu}{}_{\nu}$, defined by $\Delta T^{\mu}{}_{\nu} = \langle \chi | \hat{T}^{\mu}{}_{\nu} | \chi \rangle - T^{\mu}_{(c)\nu}$ (with $T^{\mu}_{(c)\nu}$ from the classical collapse) at $t = 1.5$.

2.5.2 Backreaction

In my simulations backreaction (the influence of the quantum effects on the curvature) is naturally built in, since the quantum mode functions contribute to the stress-energy tensor, which then determined the Einstein tensor. Therefore, in my simulations, backreaction can be traced in real time, by comparing the metric

functions' evolutions in case of semiclassical and classical simulations.

To illustrate this, I have performed this analysis on the extrinsic curvature component K_B, which is a dynamical variable in my system. The results of this can be seen in Figure 2.7.

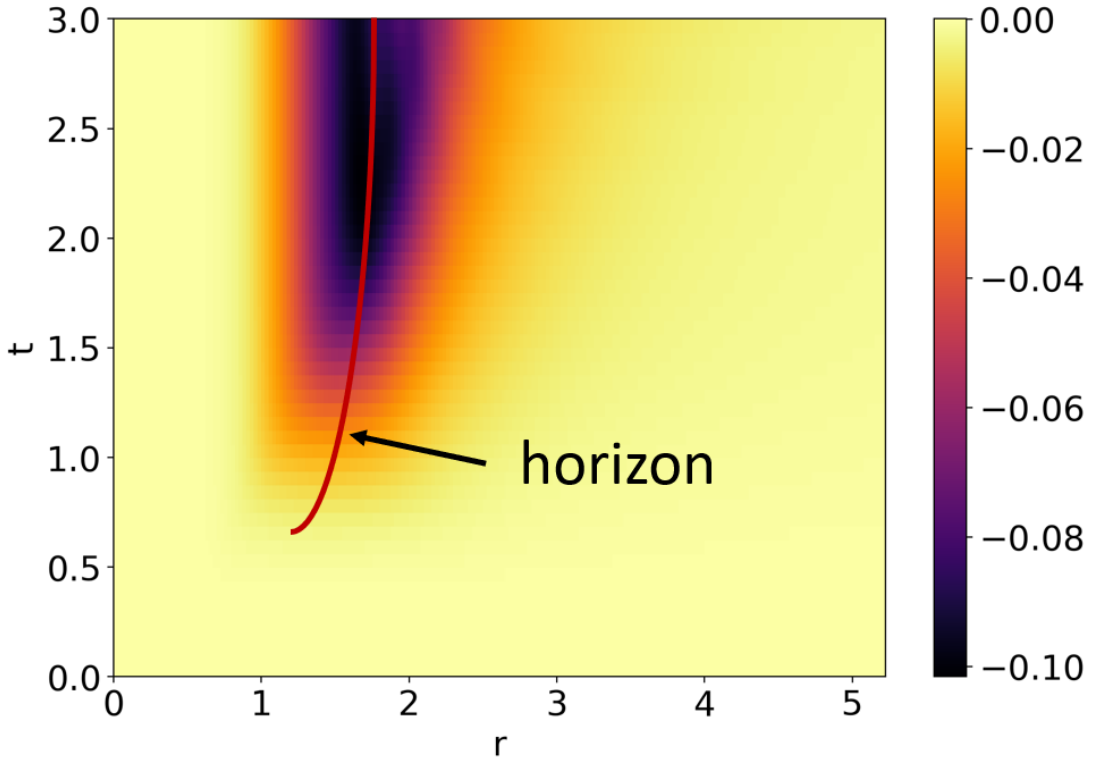

Figure 2.7: The evolution of corrections to the extrinsic curvature component K_B, defined by $\Delta K_B = K_{B(q)} - K_{B(c)}$, with $K_{B(c)}$ and $K_{B(q)}$ from the classical and semiclassical collapses respectively. The location of the apparent horizon is illustrated with a red line.

One can see in Figure 2.7 that the largest corrections to the extrinsic curvature, and hence the geometry, is around the apparent horizon itself. Note that the corrections are three orders of magnitude smaller than the extrinsic curvature, and thus they do not make a qualitative difference to the evolution. In addition, it is important to note that due to the lapse function rapidly approaching zero around the centre throughout the evolution, the dynamics there is essentially frozen. This may contribute to the small value of the extrinsic curvature correction around the centre.

2.5.3 Choptuik scaling

We have explored the subcritical and supercritical evolution of semi-classical gravitational collapse in the previous subsection. The critical behaviour in gravitational collapse has been studied extensively in the classical case, due to the universal scaling phenomena first discovered by [32]. A natural question is how the universal scaling behaviour changes in a semiclassical setting.

To answer this question, I ran the simulations closer to the critical point, both classically and semiclassically to compare the two. To this end, I fix the parameter D in Eq. (2.2.4) and vary the initial amplitude a. The apparent horizon radius is again found using Eq. (2.90), from which the mass of the black hole can be readily determined by [57]

$$M_{BH} = \frac{r_{AH}\sqrt{B|_{r_{AH}}}}{2}. \tag{2.92}$$

The results for both the classical and semiclassical simulations using various different initial amplitudes are plotted in Figure 2.8. Note that I have chosen fewer data points for the semiclassical case than the classical case. This is simply due to the computationally expensive nature of the semiclassical simulations. In addition, the difference between the semiclassical and classical black holes can be measured by

$$\delta M_{BH} = 100 * \frac{M_{BH}^{(classical)} - M_{BH}^{(semiclassical)}}{M_{BH}^{(classical)}}, \tag{2.93}$$

which defines the percentages of the deviation in the semiclassical black hole mass from the classical ones. This is also plotted in Figure 2.8. One can observe two significant features of the black hole masses in the semiclassical case relative to the classical case. First, the semiclassical black hole mass is always smaller than its classical counter part, which presumably is due to the fact that quantum effects introduce extra dissipation for the matter fields. Secondly, this difference decreases as the black hole masses decrease. However, whether or not this tendency continues

as one approaches the critical amplitude even closer is unclear.

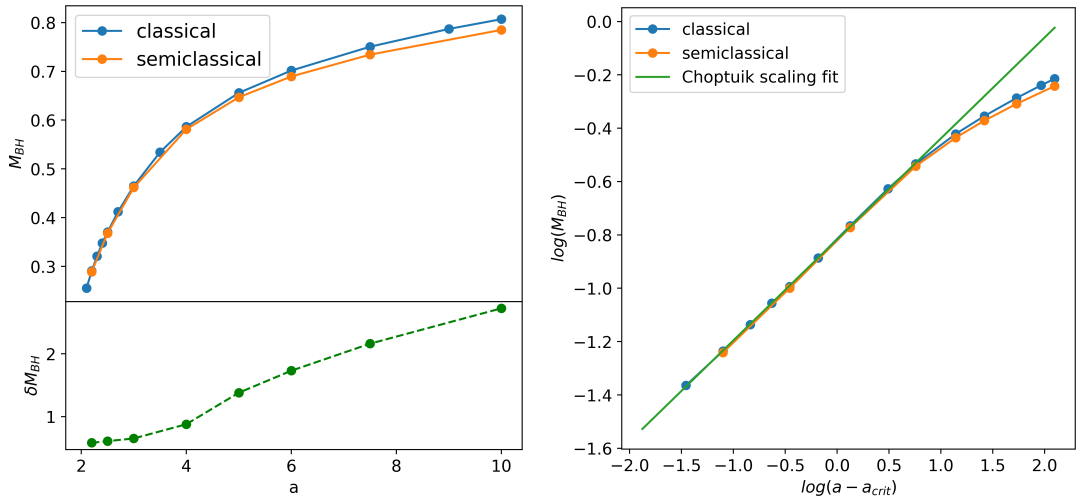

Figure 2.8: Black hole mass M_{BH} against initial amplitude a for both classical and semiclassical cases. In the left graph, both the M_{BH} and a axis are linear, whereas in the right graph they are plotted (natural) logarithmically to illustrate the proportionality. In addition, the bottom part of the left graph shows the deviation of the semiclassical black hole masses from the classical black hole masses, in percentages. As the system is tuned closer to the critical point, the deviation decreases.

Due to the gradients of functions at the centre reaching arbitrarily large values as the critical amplitude is approached, since the singularity is closer, the simulation becomes more unstable and the data points are limited in the vicinity of the critical point. Nevertheless, the value of the critical amplitude and the critical exponent can be still extracted using curve fitting. This has been done with the classical points, using a fitting function of the form:

$$M_{BH}(a, \gamma, a_{crit}, c) = c(a - a_{crit})^{\gamma}, \tag{2.94}$$

where a is the data array of the amplitudes and the other three entries, the critical exponent γ, the critical amplitude a_{crit} and the constant of proportionality c, are parameters of the fit. This function is the expected critical behaviour of the mass of the formed black holes, classically well-known. Using the non-linear least squares fit, the best values of the three parameters are found. Note that in the fitting, not

all classical data points in Figure 2.8 have been used, only the ones with smaller amplitudes, as those are the ones expected to obey the critical behaviour. Indeed, one can see the significant departure from the critical behaviour in case of the last few points (with largest amplitudes). The specific values of the fit plotted in Figure 2.8 is the following:

$$\gamma = 0.379 \pm 0.006, \qquad a_{crit} = 1.87 \pm 0.01, \qquad c = 0.442 \pm 0.003. \tag{2.95}$$

The accepted value of the classical scaling exponent in the literature [35, 64] is $\gamma = 0.374 \pm 0.001$, which is in close agreement with the value found here.

As mentioned above, the difference between the semiclassical and classical black hole masses decreases for smaller black holes as the system flows to the universal scaling limit. On the other hand, the curvature at the centre at the critical fixed point is theoretically infinite, so one would naively expect that quantum effects also get larger close to the critical point. Additionally, the strength of Hawking radiation is believed to scale as M_{BH}^{-2}, which also suggests this. Whether the semiclassical gravitational collapse approaches the classical one at the critical point is beyond the scope of this paper.

2.5.4 Correlation functions

Our system is essentially the same with which it was proved that black holes radiate, by [6], but with backreactions fully incorporated. Therefore, one should expect that Hawking radiation is present in my simulations. One way to check if it is indeed present, is to look at correlation functions inside and outside of the formed black hole. As Hawking partners are created around the horizon, one will move inwards towards the centre of the black hole, whilst the other escapes and moves towards infinity. This translates to a correlation between the quantum field

inside and outside of the black hole.

In analog models of gravity, these correlation functions have been studied, and the signature of Hawking radiation has been identified. In particular the authors of [3] numerically simulated an analog model of a horizon in a Bose-Einstein condensate, and found that once a horizon is present, long distance correlations arise inside and outside of the horizon. These correlation functions are plotted in Figure 2.9.

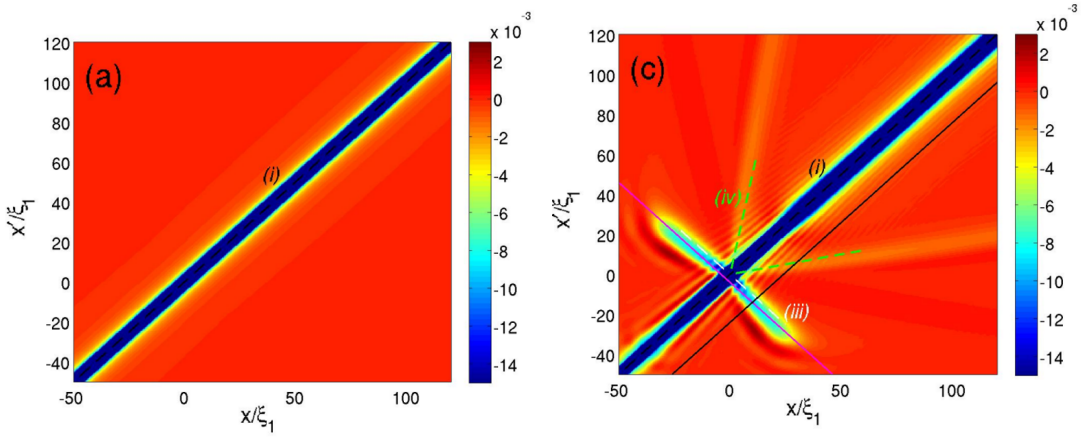

Figure 2.9: Correlation functions in an analog model of a black hole horizon. In the plot on the left, no horizon is present, whilst in the plot on the right, a horizon is present at $x/\xi_1 = 0$. Figures taken from [3]

In Figure 2.9 one can clearly see that when there is no horizon present (left hand side) there is only short range correlation, in other words, the correlation quickly go to zero away from the diagonal. On the other hand, in case of a horizon present, one can see that from the location of the horizon, there are longer range correlations perpendicular to the diagonal (denoted by (iii) on the plot). This is identified by the authors of [3] as the signature of Hawking radiation, as it corresponds to a pair of Hawking partners moving inside and outside from the horizon. Note that the plot on the right has additional lines coming from the diagonal, denoted by (iv), which according to the authors, corresponds to the backreaction effect.

In order to check whether or not similar correlations are present in my simulations, I have repeated the same analysis as above. The results of this can be seen in

Figure 2.10.

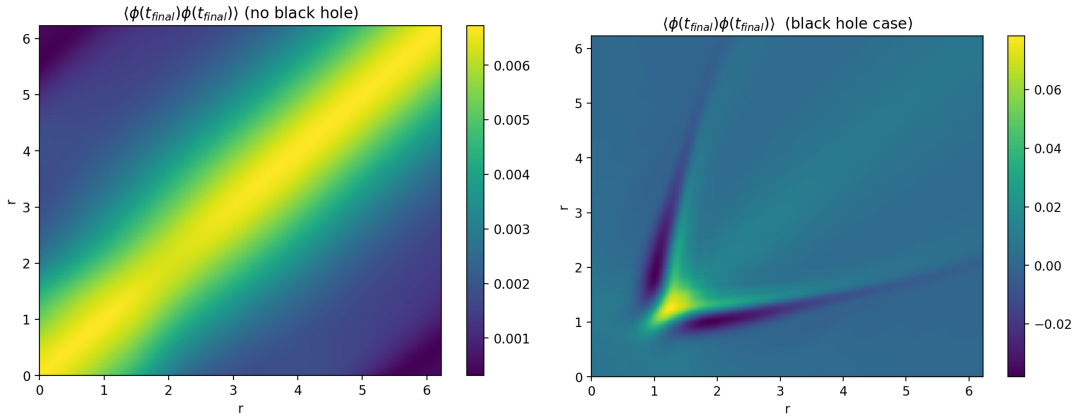

Figure 2.10: Correlation functions of the quantum field in my system. In the plot on the left, no black hole is present, whilst in the plot on the right, a black hole is present and there is a horizon at $r = 1.4$. These correlators are taken from time $t = 2.0$.

In the case of no black hole (left hand side), and hence no horizon, the same diagonal correlations are present as in the analog case. When a black hole is present (right hand side) one can see additional correlations, however, these seem to be between points that are both outside the horizon. Hence, they cannot correspond to Hawking partners. On the other hand, it should be noted that these lines are similar to the (iv) lines in the analog correlation plots. As the long-range correlations do not seem to be between the inside and outside of the black hole, one cannot say that Hawking radiation signatures can be observed in my simulations.

2.6 Convergence tests

Code validation is important to ensure that the approximate numerical system does indeed converge toward a true exact solution, ruling out the presence of systematic numerical errors that could be falsely identified with physical effects. In this section, the convergence properties of the semiclassical system are analysed in order to validate the simulation numerically. The simulations have two significant

parameters: the number of points used on the physical grid (N_{grid}) and the number of mode functions (N_l, N_k) used in the semiclassical simulation. These will be analysed separately, since they each individually must be convergent to a true solution for the convergence of the whole semiclassical system.

Let us first discuss the number of grid points, N_{grid}. Specifically, by this, I mean the number of discrete spatial points and temporal steps that the 2D computational grid is divided into. Thus N_{grid} is inversely proportional with the separation between grid points spatially dr and also temporally (through the relation $dt = dr/4$). Hence, as one uses more grid points for a given physical region, the separation between the points decreases with the grid approaching the smooth continuous spacetime. To check convergence for this parameter, the L_2-norm of the Hamiltonian constraint is analysed, which is a staple object in numerical relativity used for such purposes. This is plotted on the left hand side of Figure 2.11, for four different cases: supercritical evolution with low and high order artificial damping and subcritical evolution with low and high order damping. As the purpose of this convergence study is to calibrate the numerical accuracy of the finite difference method for the grid and the damping term, these simulations are done using classical matter, in other words, without any quantum mode functions added. From the figure, convergence for all cases is clear. It is also indicated on the graph which specific configurations are used to plot Figures 2.4 and 2.6.

In order to check convergence with respect to the number of quantum modes added, another staple numerical relativity object is chosen; the ADM mass. This is calculated using the so-called "Schwarzschild-like" mass [57], which converges to the correct ADM mass very rapidly, sufficiently far away from the centre of the spacetime where all the mass is contained. The "Schwarzschild-like" mass is defined by

$$m_{Schw} = \sqrt{\frac{A_{sphere}}{16\pi}}\Big(1 - \frac{(dA_{sphere}/dr)^2}{16\pi A(r,t) A_{sphere}}\Big), \tag{2.96}$$

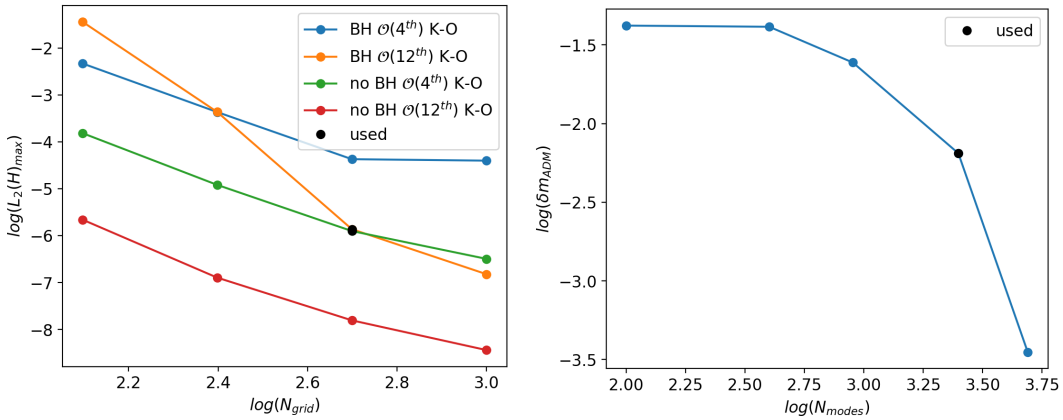

Figure 2.11: Convergence of the L_2 norm of the Hamiltonian constraint with respect to the number of grid points (left) and convergence of the ADM mass with respect to the number of quantum mode functions used (right). Note that both plots have a logarithmic scale. The dots labeled with "used" are the ones that I use in Fig. 2.4 and Fig. 2.6.

where r is an arbitrary radial coordinate, $A_{sphere} = 4\pi B(r,t)r^2$ is the area of spheres at radial coordinate r and $A(r,t)$ is the rr component in metric, Eq. (2.1). Then the ADM mass is just

$$m_{ADM} = \lim_{r\to R} m_{Schw}, \tag{2.97}$$

where R is some sufficiently large value of radial distance. Then, to measure the convergence of the system with respect to the number of added quantum modes, I define the deviation from the initially calculated ADM mass as time evolves

$$\delta m_{ADM} = \frac{m_{ADM}(t) - m_{ADM}(t=0)}{m_{ADM}(t=0)}. \tag{2.98}$$

This is plotted on the right hand side of Figure 2.11 with various different numbers of quantum mode functions added, for the black hole formation case at $t = 1.5$ and $r \approx 8.0$. The convergence is clear as the number of modes, N_{mode}, is increased. Again, the specific amount of quantum modes used to obtain the results presented in Figure 2.4 and 2.6 is indicated as well.

While monitoring the convergence of the Hamiltonian constraints and the black

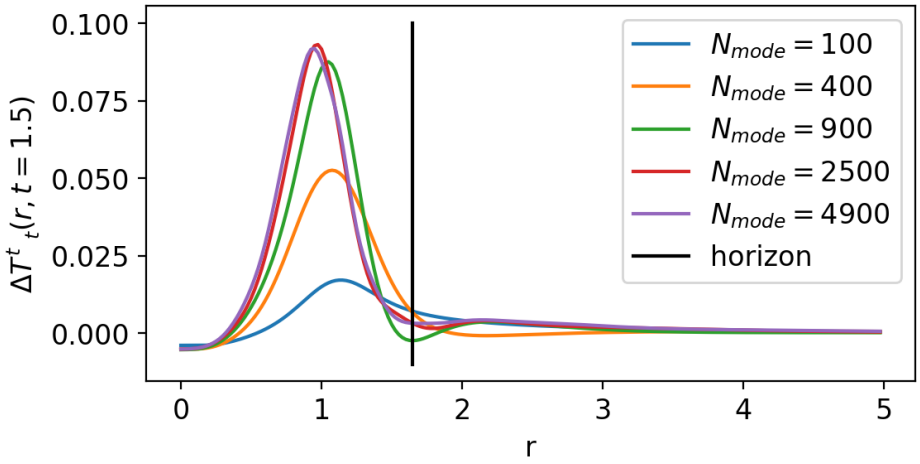

Figure 2.12: Convergence study of quantum corrections for the stress-energy tensor component $\Delta T^t{}_t = \langle\chi|\,\hat{T}^t{}_t\,|\chi\rangle - T^t_{ct}$ (with T^t_{ct} from the classical collapse) at $t = 1.5$, in case of the centred initial data.

hole mass provides a useful sanity check for the whole numerical setup, to ensure convergence of Figure 2.6 specifically, I plot $\Delta T^t{}_t$ for various different numbers of quantum modes in Figure 2.12. From this, I see that adding even more quantum modes would not qualitatively change the observed quantum deviations for the stress-energy tensor. In addition, the same convergence test for the quantum effects was performed for the non-centred initial data simulations as well. This is plotted in 2.13.

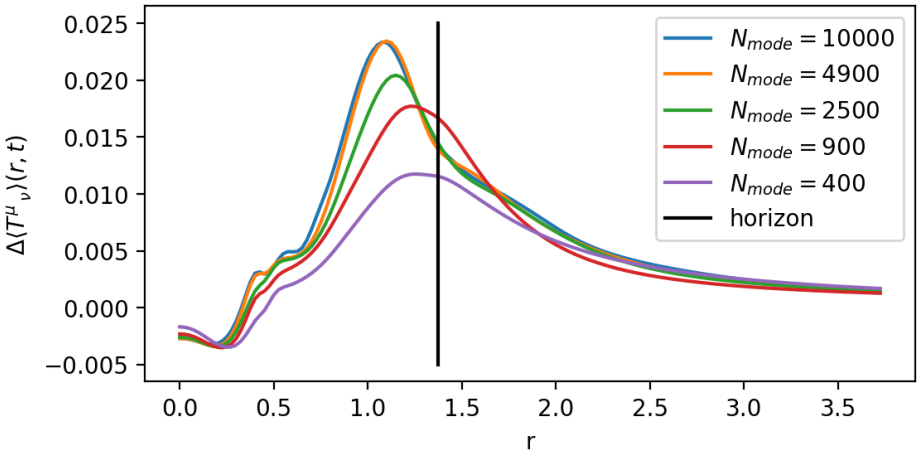

Figure 2.13: Convergence study of quantum corrections for the stress-energy tensor component $\Delta T^t{}_t = \langle\chi|\,\hat{T}^t{}_t\,|\chi\rangle - T^t_{ct}$ (with T^t_{ct} from the classical collapse) at $t \approx 0.94$ in case of the non-centred initial data.

It is also worth looking at the convergence of the Choptuik scaling. For this, I shall check the convergence of the black hole mass differences defined in Eq. (2.93) for Figure 2.8. This can be seen in Fig 2.14, where I plot the percentages of the black hole mass differences for various numbers of quantum modes. One can see that increasing the number of quantum modes makes the black hole mass corrections converge rather quickly. There is little difference between the curves with $N_{mode} = 1600$ and $N_{mode} = 2500$ ($N_{mode} = 2500$ being used in Figure 2.8) for small initial amplitude a, and good convergence has also been achieved for the larger a in Figure 2.8.

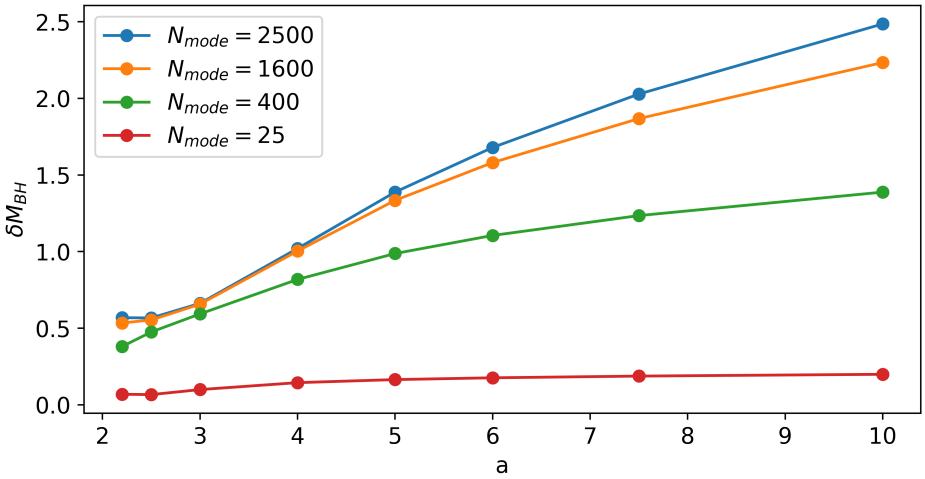

Figure 2.14: Convergence study of quantum corrections to the black hole mass M_{BH}, defined by Eq. (2.93). The vertical axis labels the percentage of the quantum corrections.

2.7 Summary

In this chapter a new formalism has been introduced to collapse quantum fields into black holes. Coherent states have been utilised in order to relate the semiclassical system to the purely classical one. This allows one to replicate the already well-studied classical simulations in a semiclassical setting, hence giving rise to a convenient framework to study quantum effects in gravitational collapse. The

simulations have been validated by convergence analysis for the L_2-norm of the Hamiltonian constraint and the deviation in the ADM mass during the evolution. In addition, the convergence of the quantum effects themselves in the results has been illustrated.

The formalism has been implemented in numerical simulations to solve the coupled differential equations of the Einstein field equations along with the Klein-Gordon (operator) equation of a fully quantum mechanical massless scalar field in a spherically symmetric spacetime. It has been shown that using a finite number of quantum modes the quantum field operator is well-defined in a finite but sufficiently large spatial grid where interesting dynamics can take place. Results have been presented for initial conditions of both the subcritical and supercritical gravitational collapse, which are in agreement with the expected classical evolution. The presence of quantum effects have been explicitly demonstrated in the case of supercritical collapse by comparing the stress-energy tensor components in the semiclassical simulation to the ones in the corresponding classical simulation. The emerging quantum effects are found to be located around the apparent horizon.

The black hole masses in the semiclassical and classical systems have also been compared. The semiclassical black hole mass seems to be always smaller than its classical counterpart, and also the difference between them grows for increasing initial energy input in the simulation. The scaling behaviour of the black hole mass with the initial amplitude of the input wave-packet was investigated for both classical and semiclassical systems. It is found that they both obey the Choptuik scaling near the critical amplitude. The scaling exponent and critical amplitude have been computed using a least squares fitting, with the results in agreement with the accepted classical values.

Chapter 3

Classical collapse with spectral methods

3.1 Introduction

In this chapter a simulation is built of the semiclassical gravitational collapse of a massless scalar field using a specific Galerkin-collocation method [65] to solve the equations of motion numerically.

The semiclassical system is based on the BSSN formulation of Einstein equations [66, 67] coupled to the quantum scalar field. This is a convenient and popular formalism since it naturally deals with the issue of the gauge choice.

I have presented the same semiclassical system using finite difference methods in chapter 2 with some results. However, these numerical techniques seem to only enable the simulation to be stable for a relatively short period of time. This means an obstacle to study effects like the Hawking radiation, which could only be meaningfully analysed once the classical dynamics are settled. Since this requires time, we turn to other numerical schemes which have a more robust stability.

The authors of [68] have published numerous works using Galerkin-collocation methods in the context of numerical relativity for various different systems. These are a subset of spectral methods that expand the dynamical fields in terms of basis functions that automatically obey the boundary conditions. Hence, the usual numerical issues imposed by $1/r$ and similar terms are not present in such systems.

In a recent publication [69] a similar system to the one used in chapter 2 is taken as an example with specific basis functions. The stability and spectral convergence of the system is illustrated. As the gravity part of our system includes almost the same dynamical fields (up to a conformal factor), to implement their numerical techniques in our simulations seems to be a natural way of improvement.

Hence, in this chapter, inspired by [69], a Galerkin-collocation type spectral method is implemented, which is tailored to our system by using specific boundary conditions, to solve the classical and semiclassical equations of a massless scalar field coupled to Einstein gravity.

The chapter is organised as follows. In section 2 the classical and semiclassical system is briefly introduced. Then, in section 3 the numerical method is presented. This is followed by some results of the classical and semiclassical system, including convergence and stability properties. Lastly, a short summary together with possible future avenues of research is presented.

3.2 Chebyshev methods

Using spectral methods is highly beneficial in numerical calculations since they achieve an incredible accuracy at a cost of more memory and computational time compared to finite difference methods. In this subsection, a specific spectral

method will be discussed, which is called Chebyshev differentiation. Note that this section is loosely based on [70].

Different spectral methods should be used for different problems. In periodic numerical problems, the functions are normally expanded using trigonometric functions using evenly spaced grids. However, for a non-periodic and bounded problem, these cannot be used, and one needs to turn to polynomial interpolation. In addition, if one uses evenly spaced grids and polynomial interpolation, the so-called Runge phenomenon [71] is encountered, which spoils the accuracy of the calculations dramatically.

Therefore, when using polynomial interpolation, one needs to use unevenly spaced grids, so that the density of the distributed points is

$$\text{density} \sim \frac{N}{\pi\sqrt{1-x^2}}, \tag{3.1}$$

where N is the number of grid points. This can be explained using potential theory [70], but the verdict is that if one has a grid between $[-1, 1]$, then a polynomial will take 2^N times larger values around $x = \pm 1$ than around $x = 0$.

The simplest set of points that cluster around $x = \pm 1$ as required is the so-called Chebyshev points:

$$x_j = \cos\left(\frac{j\pi}{N}\right), \text{ with } j = 0, 1, ..., N. \tag{3.2}$$

These are also called Chebyshev-Lobatto-Gauss points. The name originates from the fact that they are the extreme points of the Chebyshev polynomials $T_n(x)$ between $[-1, 1]$. Note that the points in (3.2) actually oriented as $[1, -1]$.

The polynomial interpolation goes as follows. Let x_j be the Chebyshev points between $[-1, 1]$ and v_j the data on it. Let p be a degree $\leq N$ polynomial such

that $p(x_j) = v_j$. The derivative $v'_j = w_j$ will be just

$$w_j = p'(x_j). \tag{3.3}$$

This is a linear operation, therefore it can be represented by a matrix such that

$$w = D_N v, \tag{3.4}$$

where D_N is a $(N+1) \times (N+1)$ matrix. D_N will be called the Chebyshev differentiation matrix.

For example, let us take the case when $N = 2$. Then, the interpolation points are $x_0 = 1$, $x_1 = 0$, and $x_2 = -1$, and we can express the interpolating polynomial $p(x)$ by

$$p(x) = \frac{1}{2}x(1+x)v_0 + (1+x)(1-x)v_1 + \frac{1}{2}x(x-1)v_2. \tag{3.5}$$

The derivative of the polynomial will now be

$$p'(x) = \left(x + \frac{1}{2}\right)v_0 - 2xv_1 + \left(x - \frac{1}{2}\right)v_2. \tag{3.6}$$

The differentiation matrix D_2 is found by substituting the relevant x_j into the derivative of the polynomial. Then the derivative at each point will be

$$\begin{aligned} p'(x=1) &= \frac{3}{2}v_0 - 2v_1 + \frac{1}{2}v_2, \\ p'(x=0) &= \frac{1}{2}v_0 - \frac{1}{2}v_2, \\ p'(x=-1) &= -\frac{1}{2}v_0 + 2v_1 - \frac{3}{2}v_2, \end{aligned} \tag{3.7}$$

and therefore the differentiation matrix D_2 is

$$D_2 = \begin{pmatrix} \frac{3}{2} & -2 & \frac{1}{2} \\ \frac{1}{2} & 0 & -\frac{1}{2} \\ -\frac{1}{2} & 2 & -\frac{3}{2} \end{pmatrix}. \tag{3.8}$$

The general form of the matrix D_N can be found as a function of the Chebyshev points and N (e.g. in [70]). The rules of making the $(N+1) \times (N+1)$ Chebyshev differentiation matrix are the following:

$$\begin{aligned} (D_N)_{00} &= -(D_N)_{NN} = \frac{2N^2+1}{6}, \\ (D_N)_{jj} &= \frac{-x_j}{2(1-x_j^2)}, \qquad \text{for} \quad j = 1, ..., N-1, \\ (D_N)_{ij} &= \frac{c_i}{c_j}\frac{(-1)^{(i+j)}}{(x_i - x_j)}, \quad \text{for} \quad i \neq j, \quad i, j = 0, ..., N, \end{aligned} \tag{3.9}$$

where

$$c_i = \begin{cases} 2 & \text{when } i = 0 \text{ or } i = N, \\ 1 & \text{otherwise.} \end{cases} \tag{3.10}$$

The jth column of the matrix D_N contains the derivative of the interpolant polynomial $p(x_j)$ of degree N to the delta function supported at the corresponding Chebyshev point x_j. Therefore applying this matrix to the data v_j on the Chebyshev grid x_j does the interpolation and differentiation at the same time, arriving at w_j; the derivative of v_j.

There is also another way to calculate the diagonal elements of D_N:

$$(D_N)_{ii} = -\sum_{j=0, j\neq i}^{N} (D_N)_{ij}, \tag{3.11}$$

which could replace the first two lines of (3.9). According to [70] this latter way of calculating leaves the Chebyshev differentation matrix with better stability properties.

Note that to find the second derivative one simply needs to square the Chebyshev differentiation matrix and act on the data using that.

Spectral methods are often extremely sensitive about the time step δt to the numerical stability of the resulting system. This is roughly due to the eigenvalues of the Chebyshev differentiation matrices and the stability regions of differentiation. Due to this, the time step should approximately go like

$$dt \sim N^{-2}, \tag{3.12}$$

for a simple leap frog time step formula. This could be also interpreted as a consequence of the x points being very close to each other around the boundaries. Using implicit or semi-implicit methods can improve this, since they are much more accurate.

In practice, to use Chebyshev differentiation, the Chebyshev matrix is calculated in our code before the simulation starts and is used later to calculate derivatives using a dot product. Also, note that the constraint on the time iteration means a significant drawback in the speed of the simulation.

3.3 Dynamical system

Here I present the dynamical system that the spectral methods solve. This is the same system as presented in Chapter 2; a massless scalar field coupled to Einstein gravity in spherical symmetry in four dimensions.

An important feature of spectral methods is that the basis functions, that are used to expand the dynamical variables, themselves must obey the boundary conditions associated with the dynamical fields. Hence in this section there will be particular emphasis put on the near zero and asymptotic behaviours of the dynamical fields

in order to choose the right basis functions for their expansion.

3.3.1 Evolution equations

The line element of the system is the same as it was in Chapter 2:

$$ds^2 = -\alpha^2(t,r)dt^2 + A(t,r)dr^2 + r^2B(t,r)d\Omega^2, \tag{3.13}$$

where $d\Omega^2 = d\theta^2 + \sin^2\theta d\phi^2$. The stress-energy tensor of the massless scalar field is

$$T_{\mu\nu} = \partial_\mu\Phi\partial_\nu\Phi - \frac{1}{2}g_{\mu\nu}\Big[g^{\rho\sigma}\partial_\rho\Phi\partial_\sigma\Phi\Big]. \tag{3.14}$$

To ensure hyperbolicity of the system, some new variables are defined in both matter and metric sectors. The evolution equations for the dynamical fields of the system are the same as presented in Chapter 2 and can be found to be:

$$\dot{\Phi} = \frac{\alpha}{A^{\frac{1}{2}}B}\Pi, \tag{3.15}$$

$$\dot{\Psi} = \partial_r\left(\frac{\alpha}{A^{\frac{1}{2}}B}\Pi\right), \tag{3.16}$$

$$\dot{\Pi} = \frac{1}{r^2}\partial_r\left(\frac{\alpha B r^2}{A^{\frac{1}{2}}}\Psi\right) + \frac{\alpha A^{\frac{1}{2}}}{r^2}\Big[\frac{1}{\sin\theta}\partial_\theta(\sin\theta\partial_\theta\Phi) + \frac{1}{\sin\theta^2}\partial_\varphi\partial_\varphi\Phi\Big], \tag{3.17}$$

for the matter field, where the angular dependence of the field was left in the equations. However, note that classically, the scalar field does not depend on

(θ, φ), but its quantum counterpart does. For the metric fields:

$$\dot{A} = -2\alpha A(K - 2K_B), \tag{3.18}$$

$$\dot{B} = -2\alpha B K_B, \tag{3.19}$$

$$\dot{D}_B = -2\partial_r(\alpha K_B), \tag{3.20}$$

$$\dot{\alpha} = -\alpha^2 f(\alpha) K, \tag{3.21}$$

$$\dot{D}_\alpha = -\partial_r(\alpha f(\alpha) K), \tag{3.22}$$

$$\dot{K}_B = \frac{\alpha}{Ar}\Big[\frac{1}{2}\tilde{U} + \frac{2\lambda B}{A} - D_B - \lambda - D_\alpha\Big] \tag{3.23}$$

$$+\frac{\alpha}{A}\Big[-\frac{1}{2}D_\alpha D_B - \frac{1}{2}D_B' + \frac{1}{4}D_B\Big(\tilde{U} + \frac{4\lambda B}{A}\Big) + AKK_B\Big] \tag{3.24}$$

$$+\frac{\alpha}{2M_P^2}(S_A - \rho - \Lambda), \tag{3.25}$$

$$\dot{K} = \alpha(K^2 - 4KK_B + 6K_B^2) - \frac{\alpha}{A}\Big[D_\alpha' + D_\alpha^2 + \frac{2D_\alpha}{r} - \frac{1}{2}D_\alpha\Big(\tilde{U} + \frac{4\lambda B}{A}\Big)\Big] \tag{3.26}$$

$$+\frac{\alpha}{2M_P^2}(\rho + S_A + 2S_B - 2\Lambda), \tag{3.27}$$

$$\dot{\lambda} = \frac{2\alpha A}{B}\Big[K_B' - \frac{1}{2}D_B(K - 3K_B) + \frac{j_A}{2M_P^2}\Big], \tag{3.28}$$

$$\dot{\tilde{U}} = -2\alpha\Big[K' + D_\alpha(K - 4K_B) - 2(K - 3K_B)\Big(D_B - \frac{2\lambda B}{A}\Big)\Big] - 4\alpha\frac{j_A}{M_P^2}. \tag{3.29}$$

Here $\rho = -T_t^t$, $j_A = T_r^t$, $S_A = T_r^r$ and $S_B = T_\theta^\theta$. These stress-energy variables are chosen in accordance with Alcubierre's method in [57], for the sake of consistency. Lastly, Λ is a cosmological constant that is classically zero, but is necessary for the regularisation of the semiclassical system.

3.3.2 Boundary conditions

Let us specify the boundary conditions of the dynamical fields. In practice this means finding their Taylor expansions around $r = 0$ and also asymptotically, as r goes to infinity. This enables one to choose suitable basis functions for the spectral expansion that possess the same near zero and asymptotic behaviours as

the dynamical fields themselves. Thus the boundary conditions are contained in the basis functions by design.

The initial scalar field is usually chosen to be a Gaussian wave-packet, hence symmetric by choice. Then, the parity of the matter fields are readily determined:

$$(\Phi^{(s)},\ \Psi^{(a)},\ \Pi^{(s)}). \tag{3.30}$$

The parity of the metric fields are

$$(A^{(s)},\ B^{(s)},\ D_B^{(a)},\ \tilde{U}^{(a)},\ K^{(s)},\ K_B^{(s)},\ \lambda^{(a)},\ \alpha^{(s)},\ D_\alpha^{(a)}), \tag{3.31}$$

The superscript indicates if the field is symmetric (s) or antisymmetric (a) around $r = 0$. These are immediately implied by the parity of the initial scalar field and the form of the Hamiltonian and momentum constraints.

The asymptotic conditions are determined by the fact that the spacetime should be asymptotically flat. For the metric fields these conditions are summarised as:

$$\begin{aligned} \alpha = A = B = 1, \\ K = K_B = 0, \\ D_\alpha = D_B = 0, \\ \lambda = \tilde{U} = 0, \end{aligned} \tag{3.32}$$

as $r \to \infty$. For the matter fields these conditions are just

$$\Phi = \Psi = \Pi = 0, \tag{3.33}$$

as $r \to \infty$.

Then, using the above information, the Taylor expansions for all fields for both around $r = 0$ and asymptotically can be found. For the symmetric fields, these

are

$$F^{(s)}(t,r) = F_0^{(s)}(t) + F_2^{(s)}(t)r^2 + \mathcal{O}(r^4), \tag{3.34}$$

as $r \to 0$, where $F^{(s)}(t,r)$ denotes all the symmetric fields from above. For the antisymmetric fields, these are

$$F^{(a)}(t,r) = F_1^{(a)}(t)r + \mathcal{O}(r^3), \tag{3.35}$$

as $r \to 0$, where $F^{(a)}(t,r)$ denotes all the antisymmetric fields listed before.

Let us now turn to the asymptotic expansions. For the symmetric fields these are

$$F^{(s)}(t,r) = F_0^{(s)} + \frac{F_{-2}^{(s)}(t)}{r^2} + \mathcal{O}\Big(\frac{1}{r^4}\Big), \tag{3.36}$$

as $r \to \infty$. In addition, for the symmetric functions ($\Phi^{(s)}$, $\Pi^{(s)}$, $K^{(s)}$, $K_B^{(s)}$) the constant vanishes, $F_0^{(s)} = 0$. Whilst for the remaining symmetric functions ($\alpha^{(s)}$, $A^{(s)}$, $B^{(s)}$) it is $F_0^{(s)} = 1$, as mentioned above.

And for the antisymmetric fields:

$$F^{(a)}(t,r) = \frac{F_{-1}^{(a)}(t)}{r} + \mathcal{O}\Big(\frac{1}{r^3}\Big), \tag{3.37}$$

as $r \to 0$.

Hence, equipped with the knowledge of the behaviour of all dynamical fields on both physical boundaries, let us proceed to discuss the numerical method.

3.4 Galerkin-collocation

As mentioned before, Galerkin-collocation methods are a specific type of spectral methods. Spectral methods are numerical techniques to solve partial differential equations where the variables are expanded in terms of basis functions, in order to transform the partial differential equation into a series of ordinary differential equations. This is achieved by solving for the coefficients of expansion.

Galerkin-collocation methods are distinguished within spectral methods by the fact that the basis functions are chosen to automatically obey the boundary conditions of the solutions. This is particularly helpful if one has $1/r$-like terms in PDEs, which numerically can be unstable and spoil the accuracy of the solutions. These instabilities are exactly cancelled at the level of the series of ODEs by virtue of the suitable basis functions.

However, one needs to find specific basis functions that obey the boundary conditions on both boundaries simultaneously. Otherwise, one can choose to divide the numerical grid into different domains [68]. Here, in the other hand, there exist a series of basis functions that obey both boundary conditions, therefore there is just one numerical domain.

The standard basis functions used in non-periodic numerical problems are the Chebyshev polynomials [65]. According to [65], there is but one set of basis functions derived from the Chebyshev polynomials that can be both symmetric and antisymmetric around $r = 0$ and also go to zero as $r \to \infty$; the even and odd sines

$SB_{2n}(r)$ and $SB_{2n+1}(r)$, respectively. These functions can be found by defining

$$SB_0(r) = \left(1 + \frac{r^2}{L_0^2}\right)^{-\frac{1}{2}}, \tag{3.38}$$

$$SB_1(r) = \frac{2r}{L_0}\left(1 + \frac{r^2}{L_0^2}\right)^{-1}, \tag{3.39}$$

$$\tag{3.40}$$

where L_0 is the map parameter. Then, by the following recurrence relation, all basis functions can be found:

$$SB_{n+1}(r) = \frac{2r}{L_0}\left(1 + \frac{r^2}{L_0^2}\right)^{-\frac{1}{2}} SB_n(r) - SB_{n-1}(r), \tag{3.41}$$

for all $n > 1$.

Hence, now, we are ready to find the expansion for the dynamical fields so that the boundary conditions are respected. These are the following for the matter fields:

$$\Phi(t, r) = \sum_{j=0}^{N} \hat{\Phi}_j(t) SB_{2j}(r), \tag{3.42}$$

$$\Psi(t, r) = \sum_{j=0}^{N-1} \hat{\Psi}_j(t) SB_{2j+1}(r), \tag{3.43}$$

$$\Pi(t, r) = \sum_{j=0}^{N} \hat{\Pi}_j(t) SB_{2j}(r), \tag{3.44}$$

where N is the truncation order. For the metric fields the expansions are:

$$\alpha(t,r) = 1 + \sum_{j=0}^{N} \hat{\alpha}_j(t) SB_{2j}(r), \tag{3.45}$$

$$A(t,r) = 1 + \sum_{j=0}^{N} \hat{A}_j(t) SB_{2j}(r), \tag{3.46}$$

$$B(t,r) = 1 + \sum_{j=0}^{N} \hat{B}_j(t) SB_{2j}(r), \tag{3.47}$$

$$D_\alpha(t,r) = \sum_{j=0}^{N-1} \hat{D}_{\alpha j}(t) SB_{2j+1}(r), \tag{3.48}$$

$$D_B(t,r) = \sum_{j=0}^{N-1} \hat{D}_{Bj}(t) SB_{2j+1}(r), \tag{3.49}$$

$$K(t,r) = \sum_{j=0}^{N} \hat{K}_j(t) SB_{2j}(r), \tag{3.50}$$

$$K_B(t,r) = \sum_{j=0}^{N} \hat{K}_{Bj}(t) SB_{2j}(r), \tag{3.51}$$

$$\lambda(t,r) = \sum_{j=0}^{N-1} \hat{\lambda}_j(t) SB_{2j+1}(r), \tag{3.52}$$

$$\tilde{U}(t,r) = \sum_{j=0}^{N-1} \hat{\tilde{U}}_j(t) SB_{2j+1}(r), \tag{3.53}$$

3.5 Results

The classical system with the Galerkin-collocation method reproduces the same evolution as presented in Chapter 2, either forming a black hole or dispersing. Since the graphs depicting this evolution are identical to the ones in Chapter 2, these are omitted from this section.

Spectral methods are known to require significantly fewer grid points to reproduce the same accuracy as finite difference methods, thanks to their global nature.

Thus, in order to understand the level of accuracy for both methods, as a function of number of grid points used, the Hamiltonian constraints are compared.

The main motivation for using spectral methods was to produce a more stable evolution for the quantum mode functions, avoiding numerical instabilities occurring at the centre that oscillate and exponentially grow, thus spoiling the semiclassical simulations. Therefore, to compare the finite difference methods from the previous chapter to the Galerkin-collocation methods presented in this chapter, the evolution of the quantum modes in simple Minkowski spacetime are analysed for both cases.

3.5.1 Hamiltonian constraint

The L_2-norm of the Hamiltonian constraint is a staple indicator of the accuracy of a numerical scheme in general relativity, showing the overall energy conservation violation of a system. As long as this violation is negligible compared to the typical energies the dynamics of the system is not changed and the evolution is controlled. In case of spacetimes in which a black hole is forming, the Hamiltonian constraint gaining order 1, or larger, values is a good indicator of the numerics breaking down due to the singularity.

Here, I present the evolution of the Hamiltonian constraint throughout a black hole collapse evolution for the presented Galerkin-collocation method with various number of points, along with the same evolution but using finite difference methods as comparison. This is presented in Figure 3.1.

These results are presented for the same initial conditions as in the previous chapter for R and D, with an amplitude of $a = 2.1$. This choice of the amplitude is motivated by the fact this is the amplitude closest to the critical amplitude that the finite difference methods are capable of simulating. More specifically, for this

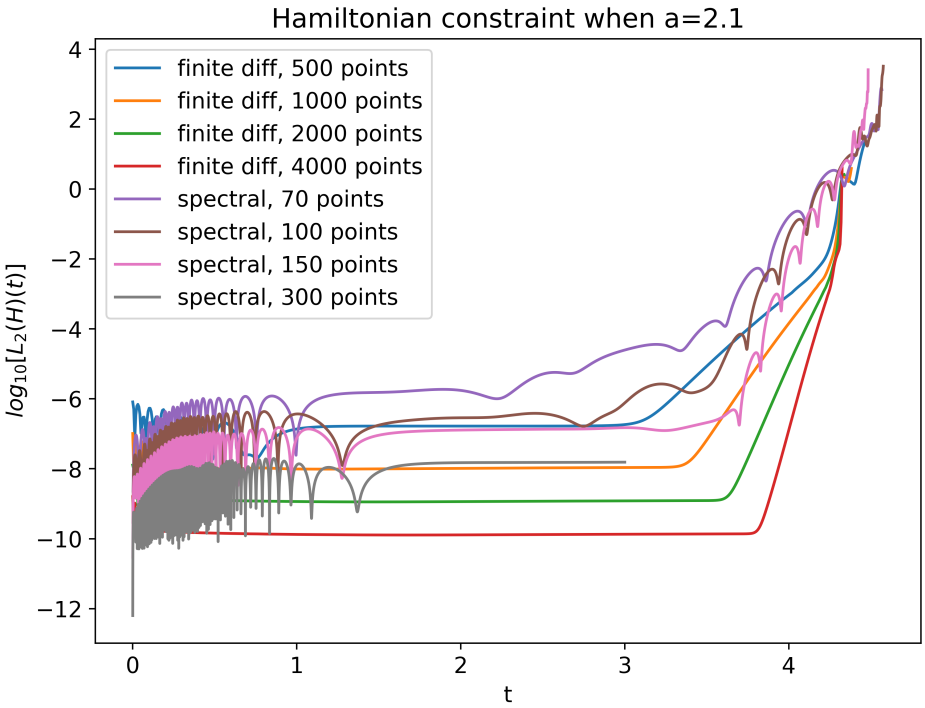

Figure 3.1: Comparison of the L_2-norm of the Hamiltonian constraint for both Galerkin-collocation method and finite difference method as a function of time, for various numbers of grid points for a typical black hole formation evolution close to the critical amplitude. (Note that in the case of the 300 point spectral method, the evolution only lasts until $t = 3$, due to memory issues.)

amplitude, the apparent horizon forms at a time when the Hamiltonian constraint is still well-behaved and negligible. For a smaller amplitude, closer to the critical amplitude, the Hamiltonian constraint blows up before an apparent horizon forms, therefore rendering the value of the apparent horizon unreliable.

The Hamiltonian constraint is presented for various numbers of grid points for both the finite difference method and Galerkin-collocation method. As it can be seen in Figure 3.1, convergence is visible for both cases, however, all methods break down at some fixed time (around $t = 4.5$), albeit the Hamiltonian constraint starts blowing up later for more grid points. Note that the power of spectral methods is apparent as a 100 grid points for the Galerkin-collocation case produces the same accuracy as 500 points for the finite difference methods.

Thus one can conclude that the Galerkin-collocation method produces comparable

results to our high order finite difference methods using a fraction of the grid points. However, it still breaks down in the vicinity of black hole formation, just as the finite difference methods.

3.5.2 Quantum mode evolution

As mentioned before, part of the motivation to use spectral methods is to produce stable quantum mode function evolution. In this subsection, these evolutions are compared for finite difference and Galerkin-collocation methods.

For this comparison, I simply evolve one quantum mode with a chosen l- and k-value in Minkowski spacetime using the two different numerical methods, to check how long they stay stable for. In flat spacetime one has access to analytical solutions to the quantum modes, therefore it gives a good toy model to study the numerics. The analytical solution for the quantum mode functions in Minkowski is:

$$u^{(M)}_{k,l}(r,t) = \frac{k}{\sqrt{\pi\omega}} e^{-i\omega t} \frac{j_l(kr)}{r^l}, \tag{3.54}$$

where $j_l(kr)$ is just the spherical Bessel function. Thus the quantum modes are just complex valued standing waves oscillating in time, with a constant norm.

The evolution equation for these quantum modes in flat spacetime is the following:

$$\partial_t^2 u_{k,l} = \frac{2l+2}{r} \partial_r u_{k,l} + \partial_r^2 u_{k,l}, \tag{3.55}$$

where as before we can cast this in first order form and evolve three dynamical variables.

The comparison is plotted in Figure 3.2, showing the evolution of three quantum mode functions with different l- and k-values. This comparison has been done with numbers of grid points in each case that produce comparable Hamiltonian

constraint violation. In the top row one can see the oscillation of the quantum mode functions calculated using finite difference methods. For $l = 10$, there are no instabilities developing around $r = 0$, however, for $l = 30$ and $l = 50$ instabilities do develop. Note that these errors develop sooner for larger l-values. In addition, they seem to be confined to close to the centre, not influencing the rest of the evolution.

In the bottom row, the oscillation of the quantum mode functions are plotted calculated using spectral methods. One can observe that the instabilities that are present in case of the finite difference methods are not there anymore. However, if one takes a closer look to the $l = 10$ case, it can be seen that the amplitude of the oscillation has increased at around $t = 8$. Therefore, errors are still present in the spectral case, but as it is a global method, the errors are also more global, and not confined to a local region around the centre of the grid.

3.6 Summary

In this Chapter I have presented spectral methods as a potential numerical alternative to finite difference methods previously used in my simulations of quantum field collapse. I have identified a specific method called Galerkin-collocation that is most suitable to solve the numerical system at hand.

The Galerkin-collocation method reproduced all classical results obtained using finite difference methods from the previous Chapter. It has been found that the Galerkin-collocation method requires a fraction of the number of grid points compared to the finite difference methods in order to produce the same accuracy (illustrated by the Hamiltonian constraint violation).

The evolution of the quantum mode functions were analysed as well, as the main

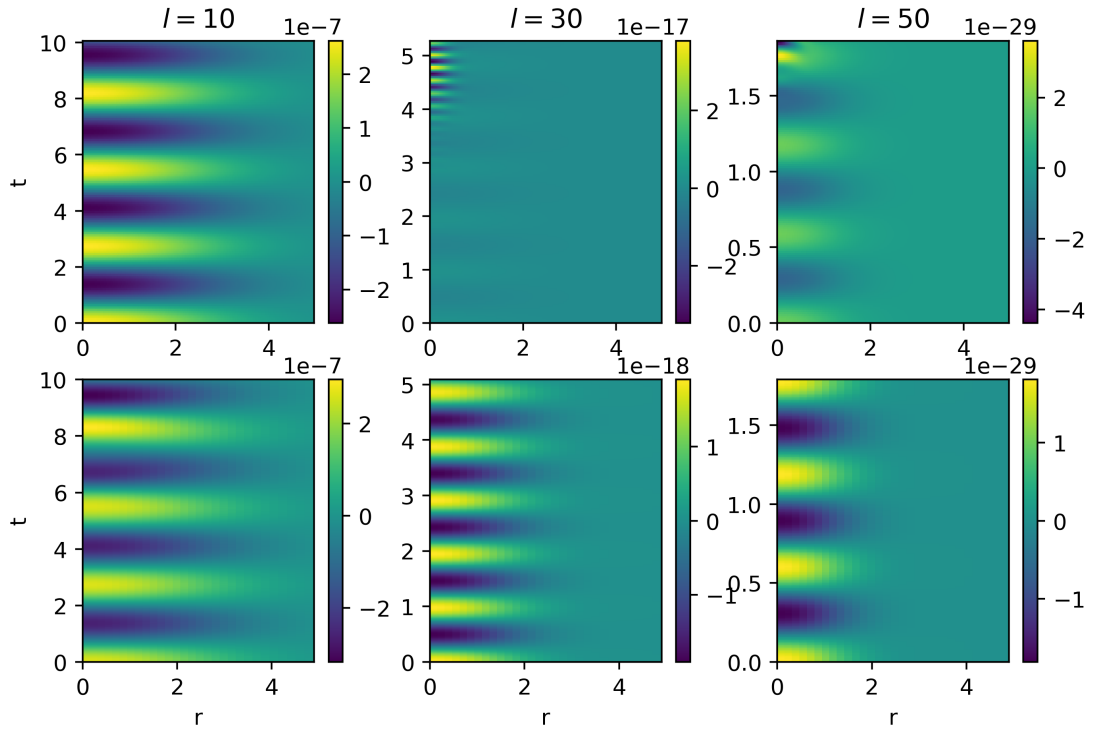

Figure 3.2: Comparison of the evolution of quantum mode functions using finite difference methods ($N_{grid} = 500$) and spectral methods ($N_{grid} = 100$) for three different l-values (note that the k-value equals the l-value for these choices). The top row corresponds to finite difference methods and the bottom row to spectral methods.

motivation of spectral methods was to produce a more numerically stable system to avoid numerical instabilities coming from the mode function equations. It has been observed that spectral methods still produce numerical instabilities, but these are more global compared to the cases with finite difference methods. In a typical black hole formation evolution the centre of the grid "freezes" due to the lapse function approaching zero there, therefore localised instabilities there do not even develop. Hence, it is easier to avoid the localised errors coming from finite difference methods than the global errors coming from the spectral methods calculation.

Due to the above observations, it is concluded that spectral methods are not more suited for the full semiclassical simulation than finite difference methods. In addition, the Galerkin-collocation method is a global one, which means that

matrices need to be calculated and its inverses must be found, which makes these simulations much slower than the finite difference ones, even though the latter involves more grid points.

Chapter 4

Quantum collapse with ingoing boundary

4.1 Introduction

In the previous chapter I attempted to change the numerical scheme from finite difference methods, used in Chapter 2, to spectral methods in order to improve on the simulations from Chapter 2. This turned out to not result in a better simulation. In this chapter, in contrast, I attempt to change the system of equations that we simulate in order to create a numerical simulation more suited to study quantum effects during and after gravitational collapse.

The new system of equations of the coupled system of gravity plus a quantum field is based on the method introduced by [4]. Rinne presents a simulation of gravitational collapse of a classical scalar field in four dimensions, where the boundary of the initial radial grid is ingoing and null. Thus, the physical radial size of the system is shrinking rapidly allowing to study the ever decreasing dynamics of the formation of tiny black holes, and so Choptuik scaling. This means that

the numerical methods required to study Choptuik scaling simplify significantly, as without a naturally shrinking system, the use of adaptive mesh refinement (AMR) is necessary. AMR is a non-trivial numerical scheme to implement where new points are introduced between already existing ones recursively in order to increase the resolution of the numerical grid where needed. Using the system introduced by Rinne, this can be avoided, and simple finite difference methods are sufficient.

The motivation to use Rinne's system is two-fold. Firstly, even though I have shown that semiclassical black holes obey Choptuik scaling in Chapter 2, only a small part of the parameter space has been explored, namely, one can get much closer to the critical amplitude and create much smaller black holes. This would be interesting to explore because quantum effects may be stronger for smaller black holes, resulting in a significantly different mass compared to their classical counter parts, and quantum effects may even stop extremely small black holes from forming. Also, the Choptuik scaling presented in Chapter 2 lacks the periodic fine structure (for both classical and semiclassical black holes), and it is unclear whether this periodicity is still present for semiclassical black holes.

The second motivation is Hawking radiation. In Chapter 2 equal-time correlators were studied with the objective of finding evidence for Hawking radiation. These were not found, however, the rate of evaporation of a black hole is inversely proportional to its mass, thus smaller black holes should show a more significant Hawking signal. Therefore one direction towards discovering Hawking radiation numerically would be to create smaller black holes that create larger long range correlations that are detectable in my numerical simulation.

This chapter is structured as follows. First, the classical system of equations is introduced based on [4]. In the next section the simple numerical methods are presented to solve the equations. Then, the classical system is promoted to a

semiclassical system involving the same quantum scalar field as in Chapter 2. After this the results of both classical and semiclassical simulations are presented, including an improved Choptuik scaling. In the last section the chapter is summarised.

4.2 Classical equations

This section is based on the numerical relativity formalism presented in [4]. Rinne uses the shift function $\beta(t, r)$ to continuously drive the far boundary at r_{max} to be ingoing and null, whilst simultaneously conformally transforming the spatial grid so that the physical grid would be shrinking, using the conformal factor $\psi(t, r)$. In other words, the physical space is "zooming in" whilst the coordinates are changing so that the numerical grid can stay the same.

In the ADM formulation of the Einstein equations the time vector $\frac{\partial}{\partial t}$ is decomposed into

$$\frac{\partial}{\partial t}^{\mu} = \alpha n^{\mu} + \beta^{\mu}, \tag{4.1}$$

where n_a is the unit future directed timelike vector, α is the lapse function and β is the shift vector. Then if one evolves from time t to time $t + dt$, the spatial coordinates will change from x^i to $x^i - \beta^i dt$. Now, if one chooses the shift vector to be proportional to the spatial coordinates themselves

$$\beta^i \propto x^i \tag{4.2}$$

then this corresponds to the coordinates isotropically zooming in. In spherical symmetry the only component of β^i that one needs to specify is β^r. Then one can choose this to be:

$$\beta^r = \beta r = cr, \tag{4.3}$$

where β is a constant which is chosen to be c, the speed of light, so that the far boundary is null. In practice β will be a function of (r, t) rather than a constant, for which an appropriate boundary condition is chosen at the far boundary to ensure that the coordinates are zooming in, with β at the far boundary doing so on a null geodesic.

Figure 4.1 shows a Penrose diagram of the simulated spacetime of a near-critical collapse with a null ingoing boundary. It illustrates how choosing the location of the far boundary (here r_{max}) has a crucial role in tuning the simulation to focus towards the relevant part of the spacetime, where the ever-decreasing dynamics is taking place. Here, the shaded area corresponds to the chosen computational domain that focuses exactly to the region where the apparent horizon first forms. In contrast, choosing r_1 as an outer boundary would result in an evolution that finishes before an apparent horizon could form. Similarly, choosing the outer boundary to be too large, r_2, the focusing is not sharp enough, hence not increasing the resolution enough to capture the ever-decreasing dynamics of near-critical collapse.

In addition the slicing condition for the lapse function α will be chosen to be maximal slicing. This allows one to penetrate the horizon of a form black hole, but also avoid the central singularity.

Thus the line element is chosen to be spherically symmetric and isotropic:

$$ds^2 = -(\alpha^2 - \psi^4 r^2 \beta^2)dt^2 + 2r\beta\psi^4 dtdr + \psi^4\Big[dr^2 + r^2(d\theta^2 + sin^2\theta d\varphi^2\Big], \quad (4.4)$$

and we define a rescaled version of the extrinsic curvature component as

$$K \equiv r^{-2}\psi^6 K^r_r. \quad (4.5)$$

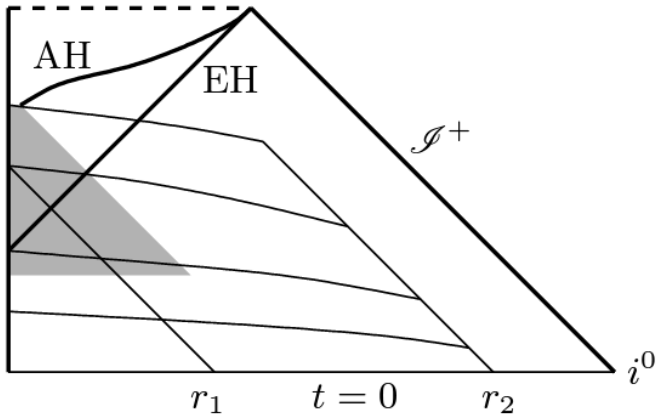

Figure 4.1: Penrose diagram of a near-critical spacetime to illustrate the "zooming in" nature of the simulated spacetime, picture taken from [4]. The simulated spacetime is shown as the grey shaded area. In addition, ingoing light rays are illustrated starting from r_1 and r_2 do demonstrate how tuning the value of r_{max} is necessary; if it is too small, the scalar field does not have time to collapse and create an apparent horizon (AH), and if it is too large, the resolution of the numerical domain is not sufficient to simulate the ever-decreasing dynamics of the collapse. Note that the apparent horizon (AH) forms inside the event horizon (EH) and approaches it towards future null infinity.

Similarly the derivatives of the scalar field $\Phi(t, r)$ are rescaled as

$$\begin{aligned} \Xi &\equiv \frac{\psi^2}{r}\Phi', \\ \Pi &\equiv \frac{\psi^4}{\alpha}(\dot{\Phi} - r\beta\Phi'). \end{aligned} \tag{4.6}$$

Thus the full system of dynamical variables is

$$(\Phi, \Pi, \Xi, \alpha, \beta, \psi, K) \tag{4.7}$$

which are all even functions in r and depend on r and t.

4.2.1 Field equations

Then one can readily derive the Einstein equations and the equation of motion of the scalar field. The Einstein equations corresponding to the momentum and

Hamiltonian constraint, respectively, are

$$\begin{aligned} rK' + 5K + \kappa\Pi\Xi = 0, \\ \psi'' + \frac{2\psi'}{r} + \frac{3}{16}\psi^{-7}r^4K^2 + \frac{1}{8}\kappa\psi^{-3}(\Pi^2 + r^2\Xi^2) = 0. \end{aligned} \tag{4.8}$$

These can be paired with a maximal slicing condition, which ensures that the trace of the extrinsic curvature stays zero, for the lapse function:

$$\alpha'' + 2\alpha'\Big(\frac{1}{r} + \frac{\psi'}{\psi}\Big) - \alpha\Big[\kappa\psi^{-4}\Pi^2 + \frac{3}{2}\psi^{-8}r^4K^2\Big] = 0, \tag{4.9}$$

and for the shift function we choose one that preserves the isotropic form of the metric:

$$\beta' - \frac{3}{2}r\alpha\psi^{-6}K = 0. \tag{4.10}$$

The evolution equations for the scalar variables are

$$\begin{aligned} \dot{\Xi} &= r\beta\Xi' + (3\beta + 2\alpha\psi^{-6}r^2K)\Xi + \alpha\psi^{-2}\frac{\Pi'}{r} + \psi^{-3}(\psi\alpha' - 4\alpha\psi')\frac{\Pi}{r}, \\ \dot{\Pi} &= r\beta\Pi' + (2\beta + \alpha\psi^{-6}r^2K)\Pi + \alpha\psi^{-2}r\Xi' + \psi^{-2}(r\alpha' + 3\alpha)\Xi. \end{aligned} \tag{4.11}$$

The scalar field itself does not enter the equations of motion but from the definition of Π one can find its equation of motion as well:

$$\dot{\Phi} = r^2\psi^{-2}\beta\Xi + \alpha\psi^{-4}\Pi. \tag{4.12}$$

For the sake of the full semiclassical system I will evolve Φ in the numerical scheme, since it will enter some evolution equations at the semiclassical level.

One can also find additional equations of motion for the metric fields ψ and K, but can be used as constraint equations. The evolution equation of ψ is

$$\dot{\psi} = r\beta\psi' + \frac{1}{2}\beta\psi + \frac{1}{4}r^2\alpha\psi^{-5}K. \tag{4.13}$$

Then we have equations to find all of our dynamical variables; we evolve the scalar variables (Φ, Ξ, Π) according to (4.12) and (4.11) in time using their time derivative, and the metric variables (K, ψ, α, β) are found using spatial integration according to (4.8), (4.9) and (4.10), in this order, as these equations form a hierarchy.

4.2.2 Initial and boundary conditions

The initial conditions for these variables can be determined as following. The scalar variables simply need an initial profile at $t = 0$ which can be freely chosen. In [4] the initial scalar variable fields are chosen as:

$$\Phi = A \exp\Big[-\frac{1}{2}\Big(\frac{r}{\sigma}\Big)^2\Big], \tag{4.14}$$

$$\Xi = \frac{\Phi'}{r}, \tag{4.15}$$

$$\Pi = 0, \tag{4.16}$$

where σ is the initial width of the wave-packet. For the metric variables, one needs to provide a boundary condition at $r = 0$ or $r = r_{max}$ at each time slice. For K this can be easily determined by enforcing its symmetry on the momentum constraint. For the shift function β we want to choose a boundary condition so that the outer boundary would be null ingoing. Thus this is enforced at the outer boundary $r = r_{max}$ and corresponds to:

$$\beta(t, r_{max}) = -\frac{\alpha(r_{max})}{r_{max}\psi(r_{max})^2}. \tag{4.17}$$

This choice ensures that the radial component of the shift vector, $\beta^r(t, r) = r\beta(t, r)$, at the outer boundary shifts the coordinate r exactly in a null line.

Also ψ can be evolved at the outer boundary as well to provide an initial condition

for its radial integration. We have freedom to choose the initial condition for the lapse function since it is merely a gauge choice. However, choosing it to be simply 1 at the outer boundary would cause too much slice stretching, so instead we choose it to be extrapolating its value at the outer boundary on the next time slice. This translates to the evolution equation

$$\dot{\alpha}(r_{max}) = r_{max}\beta(r_{max})\alpha'(r_{max}). \tag{4.18}$$

Thus we have initial conditions and evolution equations for all fields involved.

4.3 Numerical methods

Similarly as in Rinne (2020) we use an uneven grid which has more points close to the centre, and we use a staggered grid, so that $r = 0$ is not part of it.

An important note is that the value of dt must be changed at each time step since the physical grid is shrinking, and so one needs to make sure that the Courant condition is met. Hence dt is ever-decreasing, like the physical grid.

We use fourth order Runge-Kutta methods to evolve the scalar variables, and a band-diagonal matrix method to do the radial integrations, which is also fourth order.

The full classical system is then solved as follows. Given data for the scalar functions Φ, Π and Ξ at time t, the radial ordinary differential equations for the metric variables (K, ψ, α, β) are solved, in this order. These are supplied by boundary conditions by evolving ψ and α at the outer boundary according to Eq. (4.13) and Eq. (4.18) and finding β according to Eq. (4.17). The boundary condition for K is simply the fact that it is symmetric around $r = 0$. Once the metric functions are found, the scalar functions can be evolved in time to the next

time step $t + dt$ using Eq. (4.11) and Eq. (4.12). These steps are repeated until a black hole forms or the scalar disperses to the outside of the numerical grid.

4.4 Semiclassical system

Now let us turn to the version of this system with quantum matter. I start by expanding the scalar field in its mode functions, as usual:

$$\hat{\Phi} = \sum_{l,m} \int dk \Big[\hat{a}_{k,l,m} \tilde{u}_{k,l}(t,r) Y_l^m(\theta,\varphi) + \hat{a}^\dagger_{k,l,m} \tilde{u}^*_{k,l}(t,r) Y_l^{m*}(\theta,\varphi) \Big], \tag{4.19}$$

where $Y_l^m(\theta,\varphi)$ are the spherical harmonics and in the following we shall mostly use the mode functions with a factor of r^l stripped off

$$u(t,r) \equiv \frac{\tilde{u}(t,r)}{r^l}. \tag{4.20}$$

The field and its ladder operators obey the usual commutation relations.

Now, we can define similar additional mode variables, as for the classical scalar, corresponding to its first derivatives. First let us define

$$w \equiv \frac{\psi^2}{r} u'. \tag{4.21}$$

To define the momentum variable one needs to have one eye on the mode expansion of the field. Namely, schematically, the full quantum field is

$$"\hat{\Phi} = \sum r^l u Y". \tag{4.22}$$

We would like the momentum variable to obey a similar expansion:

$$"\hat{\Pi} = \sum r^l v Y". \tag{4.23}$$

Then knowing that

$$\Pi = \frac{\psi^4}{\alpha}(\dot{\Phi} - r\beta\Phi'), \tag{4.24}$$

we can insert the mode expansions as

$$r^l v = \frac{\psi^4}{\alpha}(r^l \dot{u} - r\beta\partial_r(r^l u)), \tag{4.25}$$

which becomes

$$r^l v = \frac{\psi^4}{\alpha}(r^l \dot{u} - r^{l+1}\beta u' - l r^l \beta u), \tag{4.26}$$

and so this motivates us to define

$$v \equiv \frac{\psi^4}{\alpha}(\dot{u} - r\beta u' - l\beta u). \tag{4.27}$$

Then we have our mode variables: (u, v, w), which are again even and functions of r and t. Now we can derive evolution equations for these mode variables from the original scalar equations of motion. For u this is trivial coming from the definition of v. After some algebra one can find the other equations of motion as well (see Appendix A.3), and these altogether are

$$\begin{aligned}
\dot{u} =& l\beta u + r^2\psi^{-2}\beta w + \alpha\psi^{-4}v, \\
\dot{w} =& r\beta w' + \Big[(l+3)\beta + 2\alpha\psi^{-6}r^2K\Big]w + \alpha\psi^{-2}\frac{v'}{r} \\
&+ \psi^{-3}(\psi\alpha' - 4\alpha\psi')\frac{v}{r} + \frac{3}{2}l\alpha\psi^{-4}Ku, \\
\dot{v} =& r\beta v' + \Big[(2+l)\beta + \alpha\psi^{-6}r^2K\Big]v + \alpha\psi^{-2}rw' \\
&+ \psi^{-2}\Big[r\alpha' + (2l+3)\alpha\Big]w + \frac{l}{r}\Big[\alpha' + 2\frac{\psi'}{\psi}\Big]u - m^2\alpha\psi^4 u.
\end{aligned} \tag{4.28}$$

4.4.1 Quantum state

As before, the quantum state is just a coherent state χ that ensures that the one point function of the scalar obeys the classical equation of motion.

We can go through the same derivation as before since we are still in Minkowski, the ingoing boundary is just a coordinate choice, so it doesn't affect physical variables.

Then the expectation value of the scalar will simply be

$$\phi = \langle\chi|\,\hat{\Phi}\,|\chi\rangle\,, \tag{4.29}$$

where ϕ intersects with the classical version of the scalar. Similarly for the other scalar variables:

$$\pi = \langle\chi|\,\hat{\Pi}\,|\chi\rangle\,, \tag{4.30}$$

$$\xi = \langle\chi|\,\hat{\Xi}\,|\chi\rangle\,. \tag{4.31}$$

The notation of $\pi(r,t)$ is unfortunate since we also have the number π in some of these equations, but it should be clear from the context which is which.

4.4.2 Bilinears

Since now our scalar field has been promoted to be a quantum operator we need to replace the classical bilinears with the expectation values of two point functions in the coherent state.

As before, the two point function of the scalar field is just

$$\langle\chi|\,\hat{\Phi}\hat{\Phi}\,|\chi\rangle = \phi\phi + \frac{\hbar c^2}{4\pi}\int dk \sum_{l=0}^{N_l-1}(2l+1)|\tilde{u}_{k,l}|^2, \tag{4.32}$$

We can do the same for the first derivatives of the scalar to find:

$$\langle\chi|\,\partial_t\hat{\Phi}\partial_t\hat{\Phi}\,|\chi\rangle = \partial_t\phi\partial_t\phi + \frac{\hbar c^2}{4\pi}\int dk\sum_{l=0}^{N_l-1}(2l+1)|\partial_t\tilde{u}_{k,l}|^2, \tag{4.33}$$

$$\langle\chi|\,\partial_r\hat{\Phi}\partial_r\hat{\Phi}\,|\chi\rangle = \partial_r\phi\partial_r\phi + \frac{\hbar c^2}{4\pi}\int dk\sum_{l=0}^{N_l-1}(2l+1)|\partial_r\tilde{u}_{k,l}|^2, \tag{4.34}$$

$$\begin{aligned}\langle\chi|\,\frac{\partial_r\hat{\Phi}\partial_t\hat{\Phi}+\partial_t\hat{\Phi}\partial_r\hat{\Phi}}{2}\,|\chi\rangle &= \partial_t\phi\partial_r\phi \\ &\quad+\frac{\hbar c^2}{4\pi}\int dk\sum_{l=0}^{N_l-1}(2l+1)\frac{1}{2}(\partial_r\tilde{u}_{k,l}\partial_t\tilde{u}^*_{k,l}+\partial_t\tilde{u}_{k,l}\partial_r\tilde{u}^*_{k,l}),\end{aligned} \tag{4.35}$$

$$\langle\chi|\,\partial_\theta\hat{\Phi}\partial_\theta\hat{\Phi}\,|\chi\rangle = \frac{\hbar c^2}{4\pi}\int dk\sum_{l=0}^{N_l-1}\frac{1}{2}(l+1)(2l+1)|\tilde{u}_{k,l}|^2, \tag{4.36}$$

$$\langle\chi|\,\partial_\varphi\hat{\Phi}\partial_\varphi\hat{\Phi}\,|\chi\rangle = \frac{\hbar c^2}{4\pi}\int dk\sum_{l=0}^{N_l-1}\frac{1}{2}(l+1)(2l+1)|\tilde{u}_{k,l}|^2\sin^2\theta. \tag{4.37}$$

Now in practice one would like to calculate the two-point functions of Π and Ξ as well, these can be easily found using their definitions:

$$\langle\chi|\,\hat{\Xi}\hat{\Xi}\,|\chi\rangle = \xi\xi + \frac{\hbar c^2}{4\pi}\int dk\sum_{l=0}^{N_l-1}(2l+1)|\tilde{w}_{k,l}|^2, \tag{4.38}$$

$$\langle\chi|\,\hat{\Pi}\hat{\Pi}\,|\chi\rangle = \pi\pi + \frac{\hbar c^2}{4\pi}\int dk\sum_{l=0}^{N_l-1}(2l+1)|\tilde{v}_{k,l}|^2, \tag{4.39}$$

where

$$\tilde{w}_{k,l} = r^l(w_{k,l}+\psi^2 l r^{-2}u_{k,l}), \tag{4.40}$$

$$\tilde{v}_{k,l} = r^l v_{k,l}. \tag{4.41}$$

Note that in practice the $1/r$ term in $\tilde{w}_{k,l}$ diverges, but $\langle\chi|\,\hat{\Xi}\hat{\Xi}\,|\chi\rangle$ only appears in the field equations as $r^2\langle\chi|\,\hat{\Xi}\hat{\Xi}\,|\chi\rangle$ which is regular.

These bilinears are regularised in the same way as presented in Chapter 2, using Pauli-Villars fields. The physical quantum scalar field is supplemented by five

extra non-physical fields that make sure that the regularised stress-energy tensor components are non-divergent.

4.4.3 Quantum collapse

Then we have all necessary ingredients to build the full semiclassical collapse. One important caveat to note is that now semiclassically the bilinears $\langle\chi|\,\partial_\theta\hat{\Phi}\partial_\theta\hat{\Phi}\,|\chi\rangle$ and $\langle\chi|\,\partial_\varphi\hat{\Phi}\partial_\varphi\hat{\Phi}\,|\chi\rangle$ are not zero, and thus we need to include them in the Einstein equations. In addition, we will need a cosmological constant for the regularisation procedure. Thus the Einstein field equations are altered and the radial integral equations for the metric variables also change. These are the following:

$$rK' + 5K + \kappa\,\langle\chi|\,\Pi\Xi\,|\chi\rangle = 0, \tag{4.42}$$

$$\psi'' + \frac{2\psi'}{r} + \frac{3}{16}\psi^{-7}r^4K^2 + \frac{1}{8}\kappa\psi^{-3}(\,\langle\chi|\,\Pi^2\,|\chi\rangle + r^2\,\langle\chi|\,\Xi^2\,|\chi\rangle + 2\psi^4\,\langle\chi|\,(\partial_\theta\Phi)^2\,|\chi\rangle - 2\psi^8\Lambda) = 0, \tag{4.43}$$

$$\alpha'' + 2\alpha'(\frac{1}{r} + \frac{\psi'}{\psi}) - \alpha\Big[\kappa\psi^{-4}\,\langle\chi|\,\Pi^2\,|\chi\rangle + \psi^4\Lambda + \frac{3}{2}\psi^{-8}r^4K^2\Big] = 0, \tag{4.44}$$

4.5 Results

In this section results are presented for the simulations of a scalar field coupled to gravity, in a numerical scheme where the physical space is zooming in as the system is evolved. Results are presented both for classical and semiclassical cases, this is possible as one can simply turn off the quantum modes in the semiclassical system to achieve a classical system.

First, the evolutions of subcritical and supercritical cases are examined both classically and semiclassically to illustrate how the ingoing boundary condition works.

In the semiclassical case the evolution of the fluctuations of some physical quantities are presented.

These results were performed using $N_{grid} = 500$ and $r_{max} = 5.6$, which then determines the grid spacing. As in Chapter 2, artificial dissipation is used to keep the system numerically stable with a dissipation coefficient of $\epsilon = 0.15$.

4.5.1 Black hole formation

As before, depending on the initial scalar field, the final state of the evolution may or may not result in a black hole. To illustrate this the evolution of the field $\Xi(r,t)$ is plotted for both subcritical and supercritical cases in Figure 4.2. These are results from the classical simulations, where the quantum modes are not present.

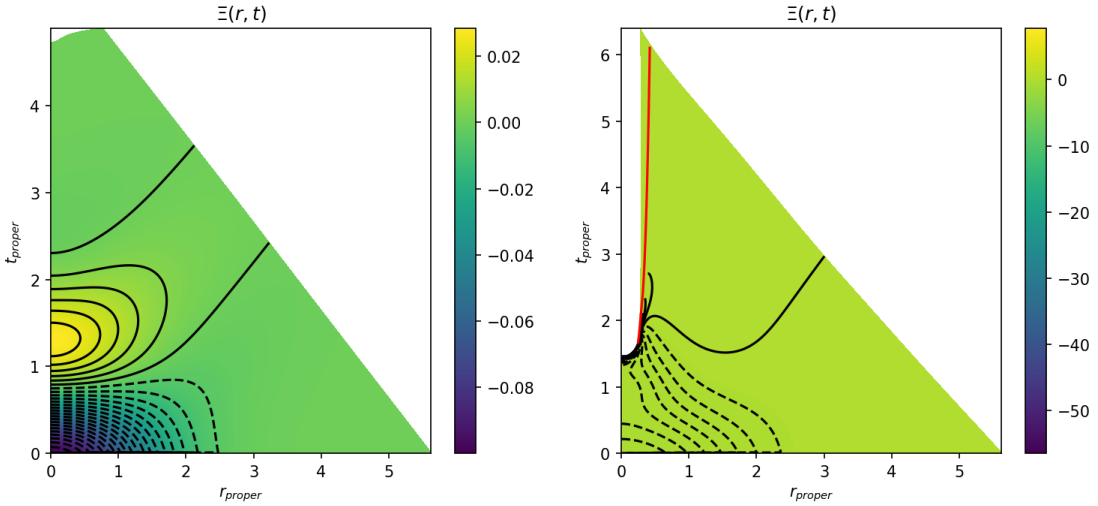

Figure 4.2: Evolution of the scalar field variable $\Xi(r,t)$ in cases when there is no black hole forming and when there is a black hole forming. The amplitude of the initial field in the second case is increased to achieve supercriticality. Note that these figures contain a heatmap together with a mesh that correspond to lines of constant values. The full lines show positive values and the dashed lines show negative values.

One can immediately observe that the outer boundary is indeed ingoing and null in

both cases. In the figure on the left, the amplitude of the initial scalar field is not large enough to reach gravitational collapse, hence the scalar field gets reflected at the origin and disperses towards the outer boundary and leaving the numerical grid. It can be observed that the scalar field is moving outward in a null line, which is what is expected as it is a massless field.

In the case of gravitational collapse, on the right side of the figure, the dynamics are somewhat different. The scalar field focuses more towards the origin and an apparent horizon forms quickly, illustrated in the figure as a red line. The apparent horizon is approaching a straight vertical line in these coordinates. The one full line travelling to the outer boundary shows that some of the scalar field pulse has managed to escape. Note that due to the maximal slicing condition, the evolution avoids the central singularity as expected, resulting in a sort of hollow physical grid. Also note that the values of the heatmap here is three orders of magnitude larger than in the no black hole case, and more specifically, these values arise close to the central singularity. Lastly, it is interesting to see how towards the end of the evolution the outer boundary of the physical grid enters the apparent horizon and thus the evolved hypersurface does not correspond to a space-like hypersurface anymore.

In addition, Figure 4.3 shows snapshots of the evolution of $\Xi(r,t)$ to better illustrate the difference between the evolution in the subcritical and supercritical cases. One can see that in the subcritical case (left) the matter field gets reflected and leaves the computational domain. However, in the supercritical case, the field gets frozen at the center before it could get reflected. This happens due to the chosen singularity avoiding gauge condition. Also, note that here the coordinate time is considered rather than the proper time, in contrast to Figure 4.2.

To illustrate the quantum effects associated to this evolution, the fluctuations of the connected two point function of $\Xi(t,r)$ are plotted in Figure 4.4 for both sub-

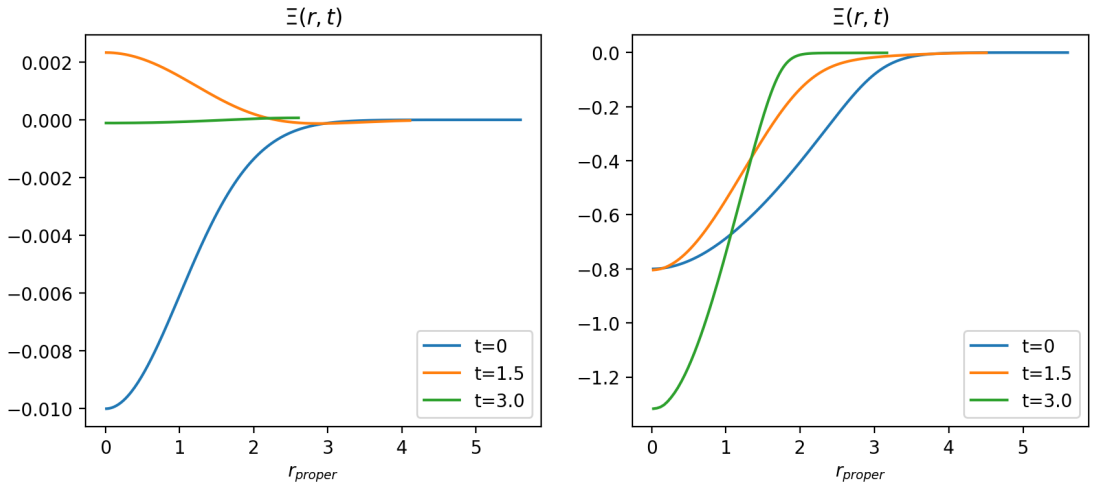

Figure 4.3: Snapshots of the evolution of the scalar field variable $\Xi(r,t)$ in cases when there is no black hole forming and when there is a black hole forming. Note that here t is coordinate time rather than proper time.

and supercritical cases. These fluctuations are defined as follows:

$$\Delta\langle\Xi(r,t)\Xi(r,t)\rangle = \langle\Xi(r,t)\Xi(r,t)\rangle - \langle\Xi(r,t)\rangle\langle\Xi(r,t)\rangle. \tag{4.45}$$

These simulations contain $N_l = N_k = 30$ modes, which is $N_{mode} = 900$ in total and also the backreaction is turned off, thus the modes do not contribute to the stress-energy tensor components. These figures differ from Figure 4.2 in that the evolutions stop sooner, which is because the quantum modes become numerically unstable around $r = 0$ in both cases, hence they are plotted until just before this happens. Moreover, in the supercritical case the apparent horizon is not plotted as it appears after the evolution has been stopped. Nevertheless, one can observe the behaviour of the quantum fluctuations in both cases. In the subcritical case the fluctuations are small and follow the classical field. In the supercritical case the amplitude of the fluctuations are much larger (order one), and one can observe that even in late times, around $t_{proper} = 3 - 4$, there are still fluctuations present.

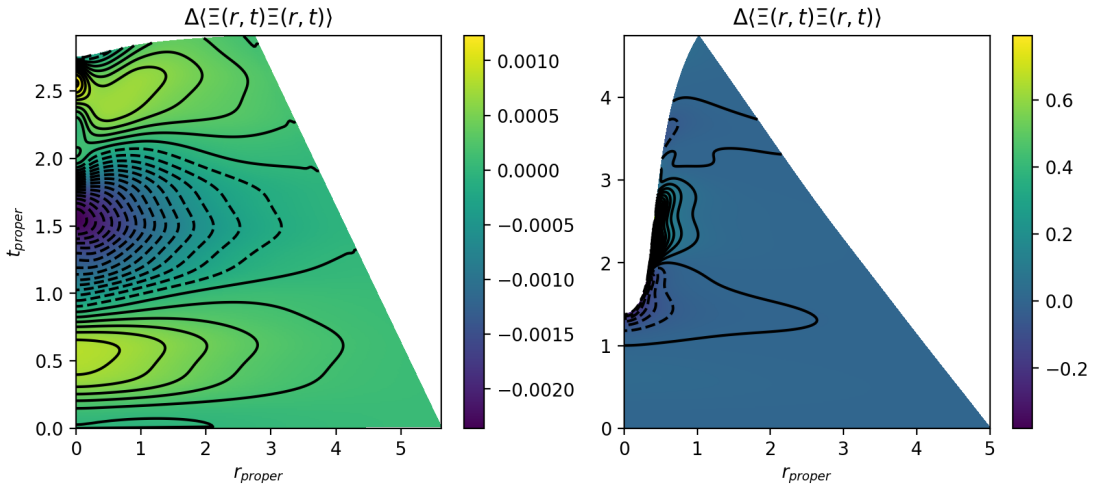

Figure 4.4: Evolution of the fluctuations of the connected two point function of the scalar field variable $\Xi(r,t)$ in cases when there is no black hole forming and when there is a black hole forming. The amplitude of the initial field in the second case is increased.

4.5.2 Classical Choptuik scaling

As stated before, the system of equations and numerical method that this chapter is based on was presented in [4], where Choptuik scaling is analysed for supercritical cases. Here, these results are reproduced for a classical scalar and also subcritical Choptuik scaling is analysed. As mentioned in the last section, backreaction is not possible to study with these specific numerical methods, as the quantum mode functions become numerically unstable and spoil the simulations before a black hole could form. Thus, the semiclassical version of Choptuik scaling is not studied in this section.

The full relation of Choptuik scaling including its periodic fine structure is the following [40]:

$$\ln M_{BH} = \gamma \ln(a - a_{crit}) + c + F(\gamma \ln(a - a_{crit}) + c), \tag{4.46}$$

where the function F has a period Δ (and, in our case, is a *sin* function). Then, γ and Δ are universal constants and only the value of c depends on the initial data.

It was first shown by [72] that the universal scaling found for black hole masses in supercritical cases also appears for subcritical cases for parameters of the spacetime like the Ricci scalar. By a simple dimensional analysis one can show that the slope of the subcritical Choptuik scaling for the Ricci scalar is double as for the supercritical black hole masses (see [72]). Here, I will illustrate subcritical cases using the central value of the stress-energy tensor component T^t_t. As it has the same dimensionality as the Ricci scalar, it should obey the same scaling relation:

$$\ln T^t_t = -2\gamma \ln(a - a_{crit}) + c + F(-2\gamma \ln(a - a_{crit}) + c), \tag{4.47}$$

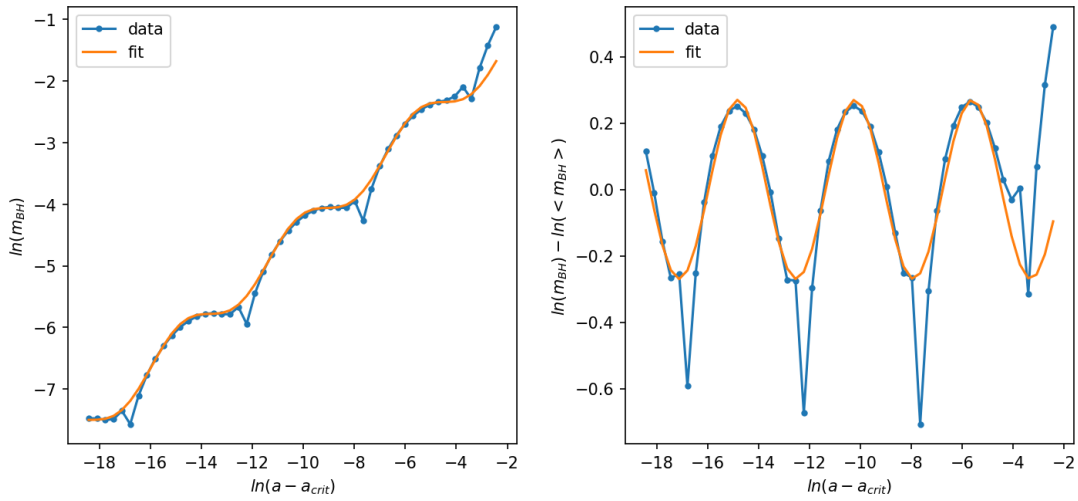

Figure 4.5: Choptuik scaling for the supercritical case. On the left the full scaling relation is shown between the logarithm of the black hole mass and the logarithm of the distance in amplitude from the critical case. On the right, the same relation is shown without the linear proportionality. The data is fitted by the orange lines that are parametrised by the known Choptuik scaling values.

The supercritical phenomena can be seen in Figure 4.5. The plot on the left shows the full relationship; proportionality together with a periodic term, and the plot on the right just shows the periodic component. The lines labeled "fit" are parametrised by the best known parameters of Choptuik scaling (see [72]):

$$\gamma = 0.374 \quad \Delta = 3.445. \tag{4.48}$$

One can see that the data and the fit agree very well.

In Figure 4.6 the central value of the (t, t) component of the stress-energy tensor is plotted as a function of the amplitude difference from the critical amplitude. Similarly, there are two graphs; the left showing the full relation and the right showing the periodic part of the scaling. The subcritical data is fitted by the same values of γ and Δ as the supercritical case.

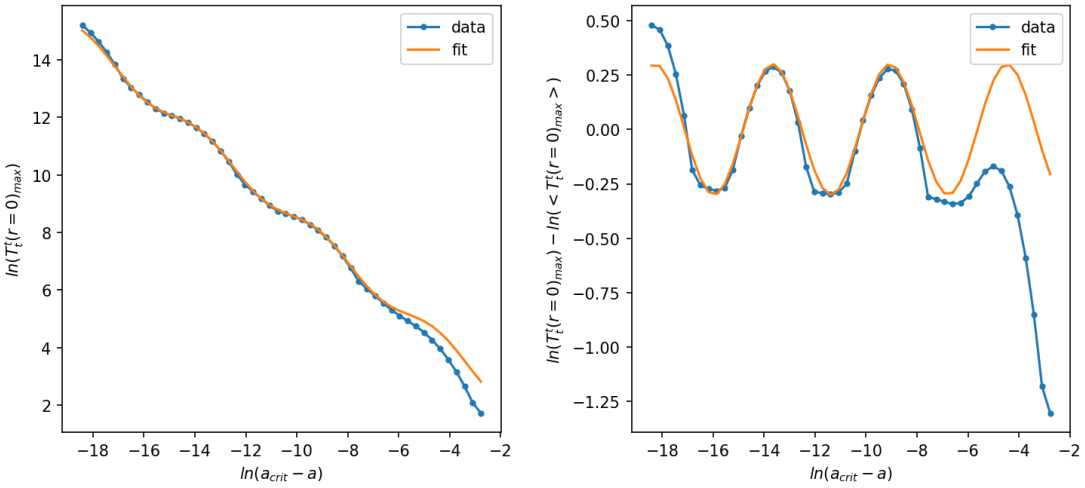

Figure 4.6: Choptuik scaling for the subcritical case. On the left hand side the logarithm of the central value of one of the stress-energy tensor components is plotted against the logarithm of the distance in amplitude from the critical case. On the right, the periodic relationship is isolated by subtracting the linear relationship. The data is fitted by the orange lines that are parametrised by the known Choptuik scaling values.

4.6 Summary

In this chapter I presented a specific formulation of the Einstein equations together with a numerical scheme, based on [4], that produces a simulation with an ingoing null boundary. This system is ideal to study critical phenomena and Choptuik scaling, as the evolution takes place at smaller and smaller scales as the critical solution is approached.

The classical system was introduced and promoted to a semiclassical system by re-

placing the classical scalar field with a quantum scalar field. Results were shown for both black hole and no black hole evolutions and the corresponding quantum effects were presented for both cases. The main purpose of implementing this method was to study the backreaction of the quantum effects for smaller black holes compared to Chapter 2, however, the numerical scheme proved to be insufficient to keep the quantum modes stable for the duration of the collapse. Nevertheless, classical Choptuik scaling was reproduced for both supercritical and subcritical cases, agreeing with the known values of the universal constants corresponding to critical phenomena.

Note that convergence tests were omitted from this chapter as this system does not allow for straightforwards tests[1]. As there are no new results presented regarding the quantum effects throughout the simulations, these needed not to be validated. In addition, the illustration of classical Choptuik scaling itself validates the code on the classical level, as the results exactly match those in [4].

It is worth noting that with a numerical scheme that is capable of evolving the quantum mode functions for long times in a stable manner this system has the potential to study the semiclassical version of Choptuik scaling to a high accuracy. A potential numerical method could be the so-called summation by parts method put forward by [73].

[1]The constraint equations that could be studied involve a time derivative, which is difficult to approximate at the fourth order in a system where the time step keeps changing. Also, pointwise convergence tests cannot be performed easily on a staggered grid, as if one doubles the number of grid points, the points do not align with the original grid.

Part II

Double null formulation

Chapter 5

Quantum collapse with $r = 0$

5.1 Introduction

In this chapter a double null formulation of a massless self-gravitating scalar quantum field is presented in 4D in spherical symmetry. The reformulation of the Einstein equations from the ADM formalism to double null is motivated by the fact that the matter in my system is massless, which means that it propagates on null geodesics. Hence, if the coordinates themselves are null, the evolution of the matter fields are simple straight lines. In addition, as I will present in the following sections, the line element and Einstein equations get significantly simpler when the (r, t) coordinates are cast into the null coordinates (u, v).

Another more practical motivation has to do with $r = 0$ in the system. Firstly, since the evolution will flow on null lines, the initial conditions will have to be null hypersurfaces as well. This means that one has a choice whether or not to include $r = 0$ in the initial null slice, and so in the full simulation in general as well. Recall that much of the numerical difficulty of building these semiclassical simulations comes from the numerical instability of the quantum mode functions

around $r = 0$. Thus, one can simply remove this point and its vicinity of the simulation space to achieve a more stable simulation. This is the subject of the next chapter.

In this chapter, I will focus on a system where $r = 0$ is part of the numerical grid from the beginning. Even though the numerical instabilities will be present in such simulations, this formulation is motivated by the fact that by construction each and every point on the initial null slice will be null and ingoing. This means that the system naturally focuses toward $r = 0$ as the evolution commences. Recall that in Chapter 4 a similar situation was artificially constructed using a specific choice of shift vector in the ADM formulation. In this null formulation of the numerical system this happens completely naturally. Thus, a double null numerical system with $r = 0$ included in it from the initial null slice is an ideal place to study Choptuik scaling.

An important difference compared to the ADM formulation simulations is that in double null coordinates the nature of the quantisation changes when promoting from a classical to a semiclassical system. In the ADM formulation the standard equal-time quantisation is appropriate, but as in a double null formulation the hypersurfaces that are evolved are not space-like but null, the quantisation itself must be done on those slices. This is a qualitatively different situation from equal-time quantisation and it bears the name light-front quantisation.

The chapter is organised as follows. First the classical system is introduced and cast into a first order system, then the light-front quantisation of the scalar field is described and lastly the full semiclassical system is presented. The classical system of equations is loosely based on [54], and the basic numerical method is based on [74].

5.2 Classical system

Here let us review the classical system of gravity plus a scalar field in spherical symmetry in double null coordinates. The fundamental coordinates in this system, instead of (t, r, θ, φ) like in the ADM formulation are going to be (u, v, θ, φ), where u is the retarded time coordinate and v is the retarded radial coordinate. Note that the angular coordinates θ and φ stay the same. In Minkowski spacetime the null coordinates have the simple definitions:

$$u = t - r, \tag{5.1}$$

$$v = t + r. \tag{5.2}$$

In more general spacetimes the coordinates t and r are some functions of u and v; $t = t(u, v)$ and $r = r(u, v)$.

Using these coordinates the metric is chosen to be:

$$ds^2 = -e^{\sigma(u,v)} du dv + r^2(u, v) d\Omega, \tag{5.3}$$

where $d\Omega^2$ is the unit sphere. Then the Einstein equations reduce to the following:

$$\partial_u \partial_v r = -\frac{\partial_u r \partial_v r}{r} - \frac{e^\sigma}{4r}\Big(1 - (\partial_\theta \Phi)^2\Big), \tag{5.4}$$

$$\partial_u \partial_v \sigma = \frac{2\partial_u r \partial_v r}{r^2} + \frac{e^\sigma}{2r^2}\Big(1 - (\partial_\theta \Phi)^2\Big) - 2\partial_v \Phi \partial_u \Phi, \tag{5.5}$$

$$\partial_u^2 r = \partial_u r \partial_u \sigma - \frac{1}{2} r (\partial_u \Phi)^2, \tag{5.6}$$

$$\partial_v^2 r = \partial_v r \partial_v \sigma - \frac{1}{2} r (\partial_v \Phi)^2, \tag{5.7}$$

where the first two are interpreted as evolution equations whilst the second two are constraint equations[1]. Note that the scalar field is assumed to be a function

[1] In this scheme u plays the role of "time" in the sense of the scheme evolving forward in time from some initial data.

of all coordinates; $\Phi = \Phi(u, v, \theta, \varphi)$. The evolution equation of the scalar field is just the Klein-Gordon equation:

$$\partial_u \partial_v \Phi = -\frac{1}{r}\Big(\partial_u r \partial_v \Phi + \partial_v r \partial_u \Phi\Big). \tag{5.8}$$

To evolve this second order system in a domain that does not include $r = 0$ we take our boundary data to live along the two null surfaces $u = u_0$ and $v = v_0$. Given that data we are able to integrate (5.4), (5.5) and (5.8) along, say, the v direction starting at $v = v_0$ on the next "time" step forward from u_0. In this scheme (5.6) and (5.7) are extra equations that may be considered as constraint equations.

Then in order to have a stable system whilst incorporating $r = 0$ in the evolution, it is sufficient to recast the equations into a fully first order system. Note that if we exclude $r = 0$, evolving the metric variables (σ, r) and the scalar Φ amounts to a stable system. Then, let us define the following group of new dynamical variables:

$$D_\Phi = \partial_v \Phi, \tag{5.9}$$

$$K_\Phi = \partial_u \Phi, \tag{5.10}$$

$$D_r = \partial_v r, \tag{5.11}$$

$$K_r = \partial_u r, \tag{5.12}$$

$$D_\sigma = \partial_v \sigma, \tag{5.13}$$

$$K_\sigma = \partial_u \sigma, \tag{5.14}$$

and also some auxiliary variables:

$$\lambda = D_r K_r + \frac{1}{4} e^\sigma \Big(1 - (\partial_\theta \Phi)^2\Big), \tag{5.15}$$

$$\mu = D_r K_\Phi + D_\Phi K_r. \tag{5.16}$$

Note that K_{sigma} does not appear in the evolution equations at all, only in a constraint equation, hence it will not be a dynamical variable. Then the full system of evolution equations is a product of integration in the u-direction:

$$\partial_u D_\Phi = -\frac{1}{r}\mu, \tag{5.17}$$

$$\partial_u D_\sigma = \frac{2}{r^2}\lambda - 2\partial_u\Phi\partial_v\Phi, \tag{5.18}$$

and in the v-direction:

$$\partial_v \sigma = D_\sigma, \tag{5.19}$$

$$\partial_v \Phi = D_\Phi, \tag{5.20}$$

$$\partial_v r = D_r, \tag{5.21}$$

$$\partial_v D_r = D_r D_\Phi - \frac{1}{2} r(\partial_v\Phi)^2, \tag{5.22}$$

$$\partial_v K_r = -\frac{1}{r}\lambda, \tag{5.23}$$

$$\partial_v K_\Phi = -\frac{1}{r}\mu. \tag{5.24}$$

To give initial conditions for the system at $u = 0$ one needs to simply choose $\Phi(0, v)$ which determines $D_\Phi(0, v)$. In addition initially, $\sigma(0, v) = 0$ which means $D_\sigma(0, v) = 0$. Then the other variables are readily integrated in the v-direction with suitable initial conditions at $v = u = 0$ (or in general $v = u$). These are the following;

$$\text{“}\partial_r\sigma(u, u) = 0\text{”}, \tag{5.25}$$

$$\text{“}\partial_r\Phi(u, u) = 0\text{”}, \tag{5.26}$$

$$r(u, u) = 0, \tag{5.27}$$

$$D_r(u, u) = -K_r(u, u) = \frac{1}{2} e^{\frac{\sigma(u,u)}{2.0}}, \tag{5.28}$$

$$K_\Phi(u, u) = D_\Phi(u, u). \tag{5.29}$$

The first two rows are in inverted commas, since strictly those dynamical fields are not functions of r, however, around $v = u$ one can make the following approximation for a function G:

$$\partial_r G(u,u) = \frac{G_n^n - G_{n+1}^{n-1}}{r_n^n - r_{n+1}^{n-1}}, \tag{5.30}$$

where the superscript denotes the u step index and the subscript the v index. Hence using this equation and the vanishing of the partial derivative of Φ and σ with respect to r when $u = v$ one can provide initial conditions for the v-integration for these variables. Note that the derivative approximation can be made higher order by including terms corresponding to G at additional previous terms in u, like G_{n+2}^{n-2}, G_{n+3}^{n-3} etc.

The numerical scheme is then the following:

- Specify initial data along $u = 0$.
  1. Choose some form for Φ, D_Φ and take $\sigma = D_\sigma = 0$.
  2. Take (5.27), (5.28) as boundary values at $v = u = 0$ to solve (5.21), (5.23), (5.22) along the v direction, giving r, D_r and K_r, using (5.15).
  3. Take (5.29) as a boundary value at $v = u = 0$ then use (5.24) and (5.16) to solve for K_Φ.
  4. We have now have values for (Φ, D_Φ, σ, D_σ, r, D_r, K_r, K_Φ) along the initial surface $u = 0$.
- evolve the system to $u = 0 + du$
  1. Use (5.17) and (5.18) to find D_Φ and D_σ on the new "time" slice.
  2. Take (5.25), (5.26), (5.27), (5.28) and (5.29) as boundary values for σ, Φ, r, D_r, K_r and K_ϕ at $v = u = du$ to solve (5.19), (5.20), (5.21),

(5.22), (5.23) and (5.24) along the v direction, giving σ, Φ, r, D_r, K_r and K_ϕ using (5.15). Note the order of the integration is important.

3. We have now have values for (Φ, D_Φ, σ, D_σ, r, D_r, K_r, K_Φ) along the next surface $u = du$.

5.3 Light front quantisation

As the hypersurfaces that the numerical grid sits on are now null rather than space-like, as in the ADM formulation, one cannot use the same equal-time quantisation process, but a light front quantisation scheme is required to quantise the scalar field.

This scheme is similar in spirit to equal-time quantisation, with the difference that the initial Lagrangian must be cast into double null coordinates, and hence the conjugate momentum and the commutation relations as well are defined using null coordinates, as expected.

The metric of the system is:

$$ds^2 = -e^{\sigma(u,v)}dudv + r^2(u,v)d\Omega^2. \tag{5.31}$$

The Lagrangian, using double null coordinates, is:

$$\mathcal{L} = \partial_u\phi\partial_v\Phi - \frac{1}{2}(\nabla\Phi)^2 - V(\Phi), \tag{5.32}$$

and the conjugate momentum is defined to be

$$\Pi = \frac{\delta\mathcal{L}}{\delta\partial_u\Phi} = \partial_v\Phi. \tag{5.33}$$

The commutation relations are then

$$\begin{aligned}[\Phi(v_1,u),\Pi(v_2,u)] &= \frac{i\hbar}{2}\delta(v_1-v_2),\\ [\Phi(v_1,u),\Phi(v_2,u)] &= \frac{i\hbar}{4}\epsilon(v_1-v_2),\end{aligned} \tag{5.34}$$

where $\epsilon(x)=1$ for $x>0$ and $\epsilon(x)=-1$ for $x<0$.

Then one can expand the scalar field as

$$\Phi = \int \frac{dk_v}{\sqrt{4\pi k_v}} \int \frac{d^2k}{2\pi}\Big[\hat{a}_k e^{-ikx} + \hat{a}_k^\dagger e^{ikx}\Big], \tag{5.35}$$

where the ladder operators obey the commutation relations

$$\begin{aligned}[a_k, a_q^\dagger] &= \hbar\delta(k-q),\\ [a_k, a_q] &= 0.\end{aligned} \tag{5.36}$$

The coherent state is defined similarly as in case of equal-time quantisation as a spherical state:

$$|\chi\rangle = \mathcal{N}\exp\left\{\frac{1}{\hbar}\int\frac{dk_v}{\sqrt{4\pi k_v}}\int\frac{d^2k}{2\pi}z(k)a_k^\dagger\right\}|0\rangle\,, \tag{5.37}$$

where the normalisation constant is defined as:

$$|\mathcal{N}|^2 = \exp\left\{\frac{1}{\hbar}\int\frac{dk_v}{\sqrt{4\pi k_v}}\int\frac{d^2k}{2\pi}|z(k)|^2\right\}, \tag{5.38}$$

and the coherent state is an eigenfunction of the ladder operator with eigenvalue $z(k)$:

$$a_q|\chi\rangle = z(k)|\chi\rangle\,. \tag{5.39}$$

So that one can express the quantum scalar field in the coherent state as

$$\begin{aligned}\Phi(x) &= \langle\chi|\,\hat{\Phi}\,|\chi\rangle \\ &= \int \frac{dk_v}{\sqrt{4\pi k_v}} \int \frac{d^2k}{2\pi}\Big[z(k)e^{-ikx} + z(k)^* e^{ikx}\Big].\end{aligned} \tag{5.40}$$

Thus Φ will correspond to the quantum scalar field expectation value in the coherent state, which intersects with a classical scalar field, as they obey the same equations of motion.

In spherical symmetry the quantum scalar has the expansion

$$\hat{\Phi}(x) = \sum_{l,m} \int dk[\hat{a}_{k,l,m}\tilde{f}_{k,l}(u,v)Y_l^m(\theta,\varphi) + \hat{a}^\dagger_{k,l,m}\tilde{f}^*_{k,l}(u,v)Y_l^{*m}(\theta,\varphi)], \tag{5.41}$$

with $\tilde{f}(u,v) = r(u,v)^l f(u,v)$ [2]. In addition, the equation of motion for the quantum scalar field is:

$$r\partial_u\partial_v\hat{\Phi} + \partial_u r\partial_v\hat{\Phi} + \partial_v r\partial_u\hat{\Phi} + \frac{e^\sigma}{4}\frac{l(l+1)}{r}\hat{\Phi} = -\frac{1}{4}m^2 e^\sigma\hat{\Phi}, \tag{5.42}$$

or rearranging it for $\partial_u\partial_v\Phi$:

$$\partial_u\partial_v\hat{\Phi} = -\frac{1}{r}\Big[\partial_u r\partial_v\hat{\Phi} + \partial_v r\partial_u\hat{\Phi}\Big] - \frac{e^\sigma}{4}\frac{l(l+1)}{r^2}\hat{\Phi} - \frac{1}{4}m^2 e^\sigma\hat{\Phi}, \tag{5.43}$$

In case of the coherent state expectation value of the quantum scalar field, this equation reduces to the classical equation for the scalar field, as expected, as it is comprised of the zero-mode ($l = 0$) and it is massless.

To find the equations of motion for the quantum modes, one can expand this above equation in terms of the modes on both sides, and rearrange for the modes

[2] In the previous chapters the quantum mode functions were denoted by u, however, as now u is a coordinate, to avoid any confusion, the quantum modes are going to be denoted by f

themselves. This is done in Appendix B.1, and the result is:

$$\partial_u\partial_v f_{k,l} = -\frac{l+1}{r}\Big(\partial_v r\partial_u f_{k,l}+\partial_u r\partial_v f\Big)-\frac{l^2}{r^2}\Big(\frac{e^\sigma}{4}(1-(\partial_\theta\Phi)^2)+\partial_u r\partial_v r\Big)f_{k,l}-\frac{1}{4}m^2e^\sigma f_{k,l}. \tag{5.44}$$

Note that from here on the subscript of the mode functions f will be suppressed to ensure cleaner equations. In the classical simulation one can define the derivatives of Φ as

$$\begin{aligned} D_\Phi &= \partial_v\Phi, \\ K_\Phi &= \partial_u\Phi, \end{aligned} \tag{5.45}$$

so in accordance, the mode functions can be defined in a similar manner:

$$\begin{aligned} D_f &= \partial_v f, \\ K_f &= \partial_u f, \end{aligned} \tag{5.46}$$

and also extra auxiliary dynamical fields can be defined to ensure stability as:

$$\begin{aligned} \lambda &= \frac{e^\sigma}{4}(1-(\partial_\theta\Phi)^2)+\partial_u r\partial_v r, \\ \mu &= \partial_v r\partial_u\Phi+\partial_u r\partial_v\Phi = D_rK_\Phi+K_rD_\Phi, \\ \mu_f &= \partial_v r\partial_u f+\partial_u r\partial_v f = D_rK_f+K_rD_f, \end{aligned} \tag{5.47}$$

and so the equation of motion for f becomes:

$$\partial_u D_f = -\frac{l+1}{r}\mu_f-\frac{l^2}{r^2}\lambda f-\frac{1}{4}m^2e^\sigma f. \tag{5.48}$$

In a numerical system then the evolution equations of the variables (f, D_f, K_f)

would be:

$$\begin{aligned}\partial_u D_f &= -\frac{l+1}{r}\mu_f - \frac{l^2}{r^2}\lambda f - m^2 e^{\sigma} f, \\ \partial_v f &= D_f, \\ \partial_v K_f &= -\frac{l+1}{r}\mu_f - \frac{l^2}{r^2}\lambda f - \frac{1}{4}m^2 e^{\sigma} f,\end{aligned} \tag{5.49}$$

where the order of these equations resemble the numerical order.

At $u = 0$ initial conditions are freely given for f, D_f and K_f. In addition initial conditions for f and K_f at $v = u$ must be provided. For f, this is achieved using the fact that "$\partial_r f = 0$" as for Φ and σ. For K_f, the initial condition is simply $K_f(u, u) = D_f(u, u)$.

The initial conditions at $u = 0$ are provided by the fact that in Minkowski there is an analytical solution to the wave equation for the mode functions, and these are the spherical Bessel functions:

$$f^{(M)} = \frac{k}{\sqrt{\pi\omega}} e^{-i\omega t} \frac{j_l(kr)}{r^l}. \tag{5.50}$$

Substituting the null coordinates u and v in the place of t and r, one can find the initial conditions for the present simulations:

$$f^{(M)} = \frac{k}{\sqrt{\pi\omega}} e^{-i\omega \frac{u+v}{2}} \frac{j_l(k\frac{v-u}{2})}{(\frac{v-u}{2})^l}, \tag{5.51}$$

and thus analytical expressions can be found for D_f and K_f as well.

5.4 Semiclassical system

Now we can put together the classical system and the mode functions to create the fully quantum mechanical scalar field plus gravity system in double null

coordinates, cast into a first order system of differential equations.

The full list of dynamical fields is:

$$\Phi, D_\Phi, K_\Phi, \sigma, D_\sigma, r, D_r, K_r, f, D_f, K_f, \tag{5.52}$$

with λ, μ and μ_f being additional auxiliary variables, and of which all are functions of u and v.

The evolution equations in u are the following:

$$\begin{aligned}
\partial_u D_\Phi &= -\frac{1}{r}\mu, \\
\partial_u D_\sigma &= \frac{2}{r^2}\lambda - 2\left\langle\chi\right| \partial_u\Phi\partial_v\Phi \left|\chi\right\rangle, \\
\partial_u D_f &= -\frac{l+1}{r}\mu_f - \frac{l^2}{r^2}\lambda f - \frac{1}{4}m^2 e^\sigma f,
\end{aligned} \tag{5.53}$$

and in the v-direction:

$$\begin{aligned}
\partial_v \sigma &= D_\sigma, \\
\partial_v \Phi &= D_\Phi, \\
\partial_v f &= D_f, \\
\partial_v D_r &= D_r D_\Phi - \frac{1}{2} r \left\langle\chi\right| \partial_v\Phi\partial_v\Phi \left|\chi\right\rangle, \\
\partial_v r &= D_r, \\
\partial_v K_r &= -\frac{1}{r}\lambda, \\
\partial_v K_\Phi &= -\frac{1}{r}\mu, \\
\partial_v K_f &= -\frac{l+1}{r}\mu_f - \frac{l^2}{r^2}\lambda f - \frac{1}{4}m^2 e^\sigma f,
\end{aligned} \tag{5.54}$$

with

$$\begin{aligned}\lambda &= \frac{e^{\sigma}}{4}(1 - \langle\chi|\,\partial_\theta\Phi\partial_\theta\Phi\,|\chi\rangle + \partial_u r\partial_v r,\\ \mu &= \partial_v r\partial_u\Phi + \partial_u r\partial_v\Phi = D_r K_\Phi + K_r D_\Phi,\\ \mu_f &= \partial_v r\partial_u f + \partial_u r\partial_v f = D_r K_f + K_r D_f,\end{aligned} \tag{5.55}$$

Note that the subscript denoting the k- and l-value for each quantum mode there are corresponding quantum mode function equations. In the above equations the bilinears of the quantum field are in expectation values. They are calculated by:

$$\begin{aligned}\langle\chi|\,\hat{\Phi}\hat{\Phi}\,|\chi\rangle &= \Phi\Phi + \frac{\hbar c^2}{4\pi}\int dk \sum_{l=0}^{N_l-1}(2l+1)\left|\tilde{f}_{k,l}\right|^2,\\ \langle\chi|\,\partial_u\hat{\Phi}\partial_u\hat{\Phi}\,|\chi\rangle &= \partial_u\Phi\partial_u\Phi + \frac{\hbar c^2}{4\pi}\int dk \sum_{l=0}^{N_l-1}(2l+1)\left|\partial_u\tilde{f}_{k,l}\right|^2,\\ \langle\chi|\,\partial_v\hat{\Phi}\partial_v\hat{\Phi}\,|\chi\rangle &= \partial_v\Phi\partial_v\Phi + \frac{\hbar c^2}{4\pi}\int dk \sum_{l=0}^{N_l-1}(2l+1)\left|\partial_v\tilde{f}_{k,l}\right|^2,\\ \langle\chi|\,\partial_u\hat{\Phi}\partial_v\hat{\Phi}\,|\chi\rangle &= \partial_u\Phi\partial_v\Phi + \frac{\hbar c^2}{4\pi}\int dk \sum_{l=0}^{N_l-1}(2l+1)\frac{1}{2}(\partial_u\tilde{f}^*_{k,l}\partial_v\tilde{f}_{k,l} + \partial_u\tilde{f}_{k,l}\partial_v\tilde{f}^*_{k,l}),\\ \langle\chi|\,\partial_\theta\hat{\Phi}\partial_\theta\hat{\Phi}\,|\chi\rangle &= \frac{\hbar c^2}{4\pi}\int dk \sum_{l=0}^{N_l-1}(2l+1)\left|\tilde{f}_{k,l}\right|^2 sin^2\theta,\end{aligned} \tag{5.56}$$

where the last bilinear does not have a "classical" part, since it is classically not dependent on θ. These equations are supplemented by initial conditions and boundary conditions described in the previous sections.

Note that the exact same regularisation scheme applies for this semiclassical system as presented in Chapter 2 for the ADM formulation. There are five additional dynamical Pauli-Villars fields that contribute to the stress-energy tensor components in order to make the divergences cancel out and thus create physical values.

One has freedom in choosing the values at $u = 0$ for D_Φ, D_σ and D_f. D_Φ is chosen so that Φ is a gaussian lump on the initial v-grid, $D_\sigma = 0$ initially, and

D_f are determined by the fact that in Minkowski spacetime the solutions to the wave equation of the mode functions are the spherical Bessel functions. For the quantum modes and regularisation scheme, the same parameters are used as in Chapter 2 (minimum wavenumber dk, ghost mass M_{PV}), and hence the vacuum plots would look exactly the same.

Hence we have a full system of partial differential equations and initial conditions for these and we can start simulating the dynamics of the system.

5.5 Numerical methods

The numerical grid is simply a uniform grid both in u and v with $du = dv = h$. Note that since $r = 0$ is part of the grid, at $u = v$, this means that at each advance in u, e.g. from u_n to $u_n + du$ one loses the innermost grid point. Hence, after evolving the system for n u-steps, one has $N - n$ grid points (if N is the number of grid points at $u = 0$). This is simply because each grid point is null and ingoing and end at $r = 0$. To increase resolution as we focus around $r = 0$ we interpolate the lost points between the existing ones. More specifically, once we have lost half of the grid points, we stop the evolution and interpolate our dynamical fields half way between the existing grid points. Hence every time the numerical grid halves, the resolution is doubled.

5.6 Results

Once both classical and quantum initial conditions have been specified along with the evolution equations for all dynamical fields, one can start evolving the system. In this section I present semiclassical simulation results for both subcritical and supercritical cases. First I present the evolution of the coherent state expectation

value of the scalar field, $\Phi(u,v) = \langle\hat{\Phi}\rangle$ and the radial variable $r(u,v)$. Then, the quantum fluctuations are examined through the expectation value of a two-point function of one of the scalar variables. Lastly, classical results are presented of Choptuik scaling, including its fine-structure.

Note that in the simulations presented here the backreaction is turned off (in other words, the quantum modes do not contribute to the stress-energy tensor). This is due to the fact that the numerical instabilities seemed to be stronger in that case, and the quantum modes would diverge numerically before the meaningful dynamics would unfold. For this reason as well, a semiclassical Choptuik scaling is not presented in this section.

The more unstable nature of the quantum modes compared to the systems and simulations presented in the previous chapters can be explained by the fact that the numerical methods here involve a simple first order accurate system. Even though the radial domain is shrinking resulting in increasing resolution, this is not enough to account for the low numerical accuracy. Increasing the order of accuracy of the numerical solutions is not as straightforward as in the other systems, as $r = 0$ is involved in the system while r is also a dynamical variable. In addition, the boundary conditions for some of the dynamical fields utilises their symmetry with respect to r. Thus, going above first order accuracy becomes a nontrivial task that is omitted from this chapter.

Note that the numerical simulations here have a constant step size of $du = dv = h = 0.02$ and $N_{grid} = 513$.

5.6.1 Black hole formation

Here I will examine the evolution of some of the dynamical fields for cases when no black hole forms or a black hole forms. The results from the simulations presented

here involved a quantum field composed by a coherent state expectation value and some mode functions. Due to the numerical instabilities of the mode functions, the total number of quantum modes involved in these simulations was $N_{mode} = 100$, namely with $N_l = N_k = 10$.

Note that in these coordinates the location of the apparent horizon is at

$$\partial_v r = 0, \tag{5.57}$$

corresponding to a trapped surface. Then, the largest r for which there is a point where $\partial_v r = 0$ is said to be the radius of the black hole. In the limit of v goes to infinity, this corresponds to the event horizon exactly.

Let us start with the evolution of the coherent state expectation value, $\Phi(u, v)$. This is plotted in Figure 5.1 for both subcritical and supercritical cases. In both cases the initial scalar field is a Gaussian lump located at $v = 5$ with unit width. The amplitude of the field is adjusted to reach subcritical or supercritical evolutions. Note that in both figures the diagonal line at $u = v$ corresponds to $r = 0$. On the left plot one can observe the scalar field propagating towards $r = 0$ vertically upwards, which is what one expects as the field is massless and hence propagates on null lines. Once the scalar reaches the diagonal of $r = 0$ it gets reflected and becomes an outgoing field, now travelling on horizontally, corresponding to outgoing null lines. In Minkowski spacetime one would expect the scalar field to fully get reflected, however, as gravitational dynamics take place, one can see an additional small scalar oscillation around the centre.

In the black hole formation case, on the right side of Figure 5.1, the evolution starts in the same manner as before. However, as the amplitude was slightly increased in this case, the dynamics changes qualitatively. While the scalar field is getting reflected it collapses and start diverging. A nice feature of these double

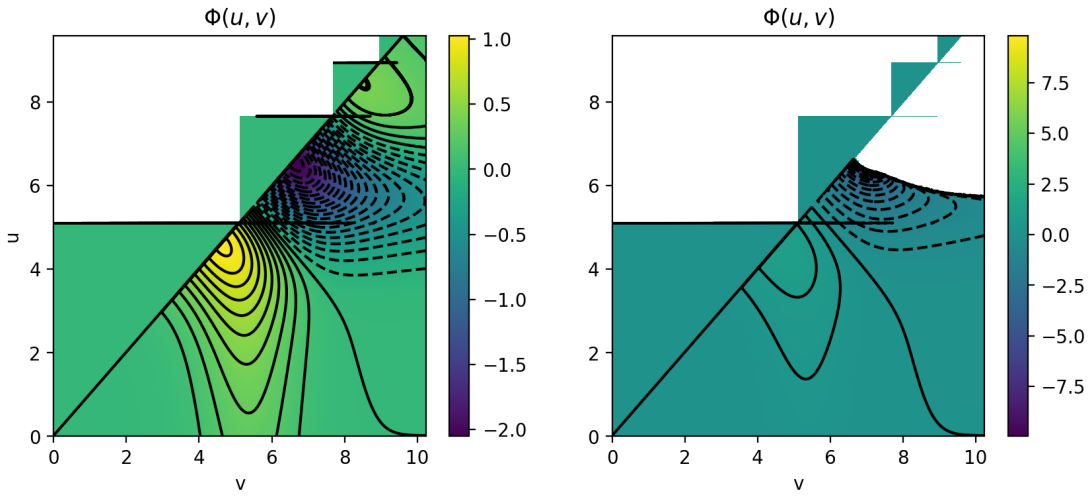

Figure 5.1: Evolution of the classical scalar field $\Phi(u, v)$ in cases when there is no black hole forming and when there is a black hole forming. The amplitude of the initial field in the second case is increased to achieve supercriticality. Note that these figures contain a heatmap together with a mesh that correspond to lines of constant values.

null simulations is that one can see the singularity enter the numerical domain at $v = v_{max} = 10$ and reach $r = 0$.

Note that, as explained in the previous section, on these plots the numerical domain is shrinking, as the grid points correspond to ingoing null lines, which once reached the centre, disappear. These points are then recycled once half of them have been lost, by interpolating between the other half of the points. This is the reason for the shrinking squares in the upper diagonal of the plots.

In addition, the same evolution as in Figure 5.1 is plotted using (t, r) coordinates instead of (u, v) in Figure 5.2. Here r and t are simply defined by Eq. (5.1). It can be seen that the initial surfaces are null in both cases, and that the matter field propagates on an ingoing null line towards the center perpendicular to it. In the no black hole case it gets reflected and leaves the computational domain, whilst in the black hole case, it hits the forming singularity. In the latter case it can be seen that the singularity starts on a spacelike surface and slowly asymptotes to an outgoing null line.

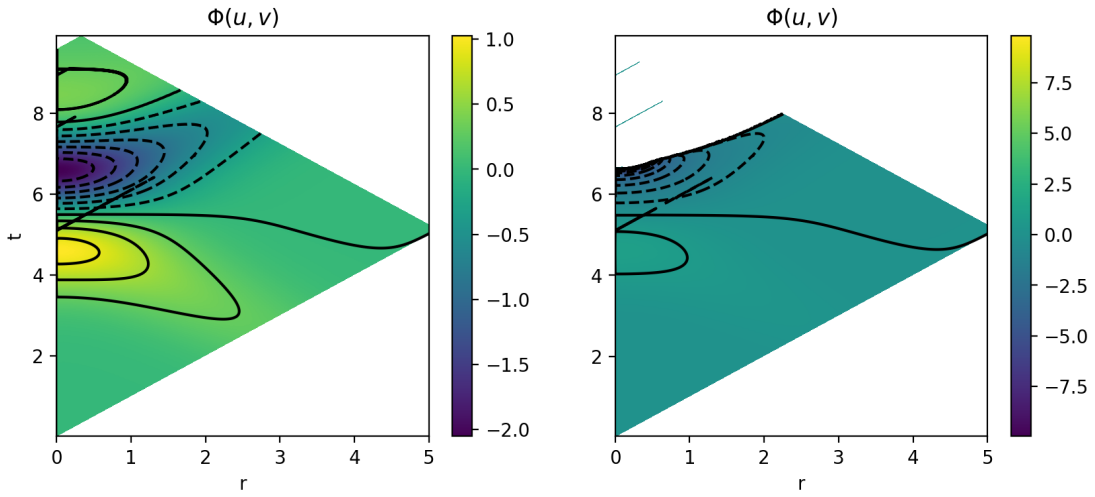

Figure 5.2: Evolution of the classical scalar field $\Phi(u, v)$ in cases when there is no black hole forming and when there is a black hole forming, using coordinates (t, r).

Let us now turn to the evolution of the radial variable $r(u, v)$. These evolutions can be seen in Figure 5.3. As before, the no black hole evolution is plotted on the left. In this case the constant r lines (black contours) are barely off of a diagonal direction, which would correspond to Minkowski. Only when the scalar field gets reflected, at around $u = 5$, do the lines show different behaviour, signalling that there is significant curvature in the spacetime. However, the lines quickly go back and approach 45° once again.

In the black hole formation case, on the right of Figure 5.3, similarly the constant r lines seem close to diagonal, however, after the scalar gets reflected, they start approaching a horizontal line. This is signalling black hole formation and in this case a black hole forms with radius $r = 0.3$. Again, one can see the singularity explicitly enter the numerical domain and reaching the main diagonal line. Note that the colour bar has limits 0 to 9 in the black hole case, however, the initial limits of r is actually 0 to 5, like in the no black hole case. The reason for the larger limit in the black hole case is simply that close to the singularity all variables diverge numerically, and hence r reached a higher value than its initial limit.

In order to examine the quantum effects present in these simulations, I plot the

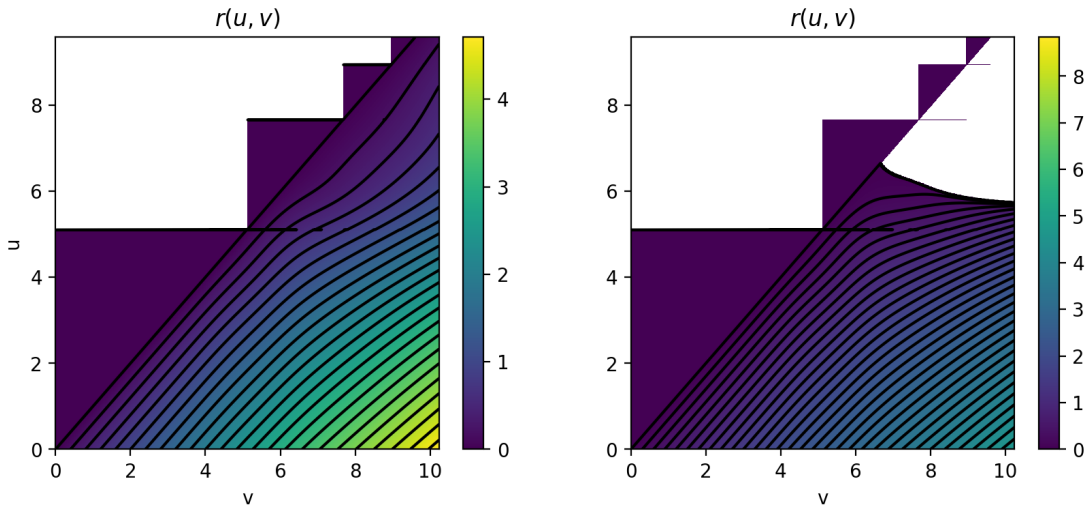

Figure 5.3: Evolution of the radius $r(u, v)$ in cases when there is no black hole forming and when there is a black hole forming. The amplitude of the initial field in the second case is increased to achieve supercriticality. Note that these figures contain a heatmap together with a mesh that correspond to lines of constant values.

fluctuations of a bilinear of the scalar field. Namely,

$$\Delta\langle \hat{D_\Phi} \hat{D_\Phi} \rangle = \langle \hat{D_\Phi} \hat{D_\Phi} \rangle - \langle \hat{D_\Phi} \rangle \langle \hat{D_\Phi} \rangle, \tag{5.58}$$

where D_Φ is the v-derivative of the scalar field. These are presented in Figure 5.4. Note that here the evolutions are plotted for a smaller range in u, due to the quantum mode instabilities spoiling the evolutions at later advanced times. Once again, no black hole case on the left and black hole case on the right. In the no black hole case, one can observe small oscillations of the quantum modes in the timelike direction. This is expected, as in Minkowski these modes are simply standing waves. As we are slightly away from Minkowski space here, the modes show some nontrivial oscillations, that are nevertheless small.

In the black hole case on the right, however, the evolution seems qualitatively different. Note that here the red line shows the location of the event horizon, which is essentially the largest radial location of the apparent horizon. In this case the quantum fluctuations are an order of magnitude larger than in the no

black hole case, and they seem to be propagating in null directions, both ingoing and outgoing.

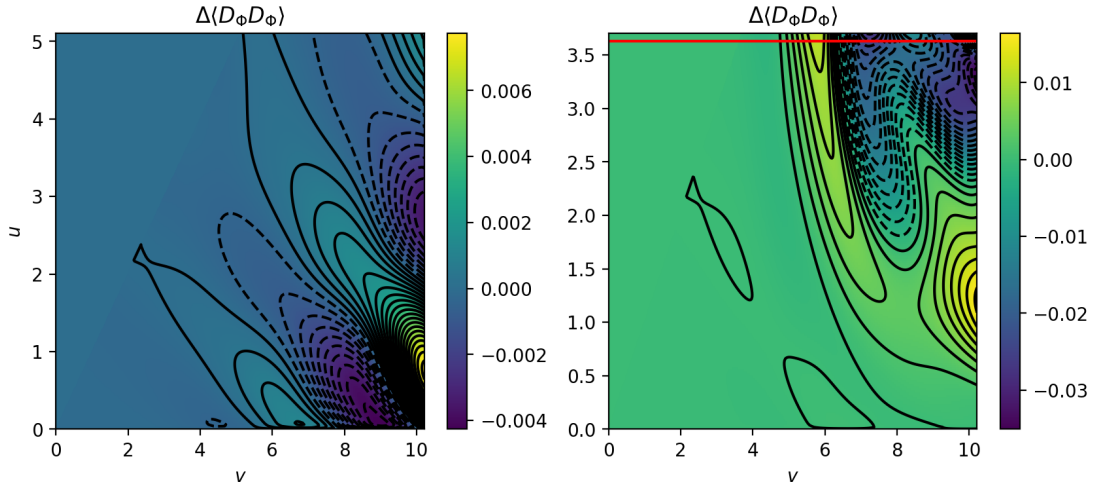

Figure 5.4: Evolution of the bilinear $\Delta\langle D_\Phi D_\Phi\rangle$, which is the fluctuations around the two-point function of the $v-$derivative of the scalar operator Φ. Plotted for the case of no black hole (left), and the case of black hole formation (right).

Thus, I have shown nontrivial quantum effects present in both subcritical and supercritical cases. However, these simulations only contain a 100 modes ($N_l = N_k = 10$), which is not enough to fully capture the dynamics of the quantum fluctuations, according to the convergence studies conducted in Chapter 2. Nonetheless, the presented simulations give a flavour of how the quantum effects look like qualitatively.

5.6.2 Classical Choptuik scaling

Due to the ever increasing resolution of the numerics as the physical domain shrinks, this system is capable of capturing classic Choptuik scaling to a high accuracy. Remarkably, this is achieved in spite of the relatively low order of numerical accuracy (first order). Nevertheless, the shrinking nature of the physical domain is not sufficient to ensure numerical stability of the quantum mode functions. This is further complicated by the fact that smaller black holes take longer

to form, thus creating a need for stable quantum mode functions for longer time scales. Hence, in these simulations the numerical methods were not sufficient for full semiclassical simulations, but only purely classical ones. Thus, in this section I present results of Choptuik scaling, with its fine-structure, and self-similar behaviour of the classical scalar field.

This analysis was achieved by finding the critical amplitude for the set of initial conditions presented in the previous subsection, using a binary search between amplitudes achieving sub- and supercritical evolutions. This required finding a suitable initial v_{max} as well, as this determines the location towards which the physical domain is shrinking.

Chopuik scaling for the supercritical case is presented in Figure 5.5. The plots show the formed black hole mass as a function of the difference between the initial amplitude and the critical amplitude. These are presented on log scales. The plot on the left presents the full Choptuik scaling relation; the linear proportionality and the periodicity together. On the right plot, the linear part of the relation is removed by subtracting the mean proportionality to isolate the periodic fine-structure. The data is fitted with the exact values of Choptuik scaling found in previous studies. Note that the difference in the amplitudes reaches e^{-33}, which corresponds to 10^{-15}, that is essentially machine accuracy.

The self-similar behaviour of the classical scalar field was also examined, by simply plotting its evolution at $r = 0$; this can be seen in Figure 5.6. The x-axis on this plot is the negative logarithm of the difference between the advanced time u and the time of black hole formation at u_{crit}. One can see that the scalar oscillates three times until the black hole forms, on ever decreasing advanced time scales. The red dots illustrate the oscillation with period found by previous studies of self-similarity in this setting. They agree well with the peaks of the oscillations of the scalar field.

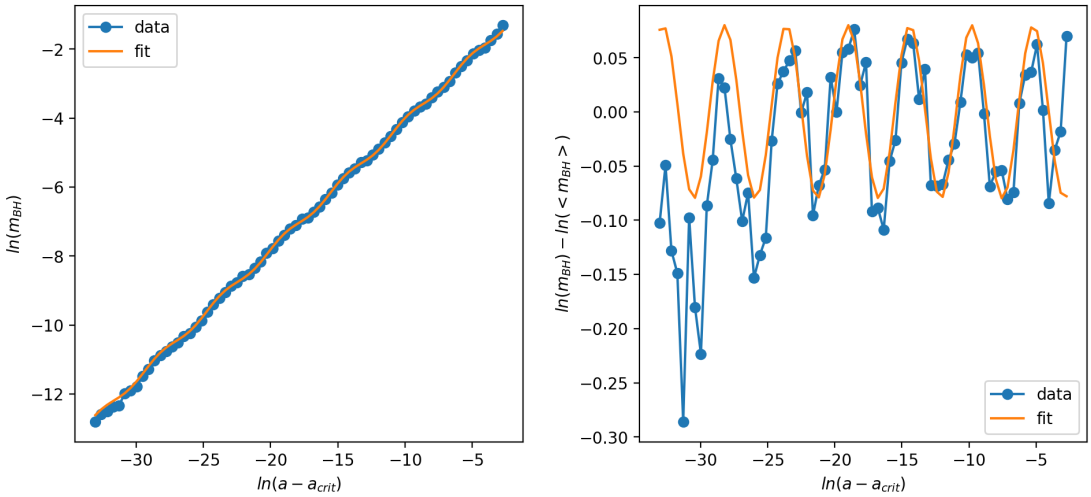

Figure 5.5: Choptuik scaling for the supercritical case. Similarly as for the scaling plots in Chapter 4, on the left graph the full scaling relation is shown and on the right the periodic component is isolated. The data is fitted by the orange lines that are parametrised by the known Choptuik scaling values.

5.7 Convergence tests

In order to validate the simulation some convergence studies were conducted for both the classical fields and quantum modes. This data comes from simulations where a black hole does not form, but the initial amplitude is large enough to create considerable curvature (half of the critical amplitude).

Here, the point-wise convergence of some dynamical fields is presented. This allows one to examine the convergence of individual fields, hence providing more detail than just examining the constraint equations. This analysis involved running the same simulation with increasing (double) resolutions. Then, the difference between fields with doubled resolution is plotted. If the numerical solutions are converging towards a true solution, these differences must overlap.

In Figure 5.7 the point-wise convergence of the scalar variable $\Phi(u, v)$ is plotted together with the metric variable $\sigma(u, v)$. These are taken from the no black hole evolution with a constant advanced time coordinate $u = 3$. Note that because the point $r = 0$ corresponds to $u = v$, since the figures are plotted at $u = 3$, these start

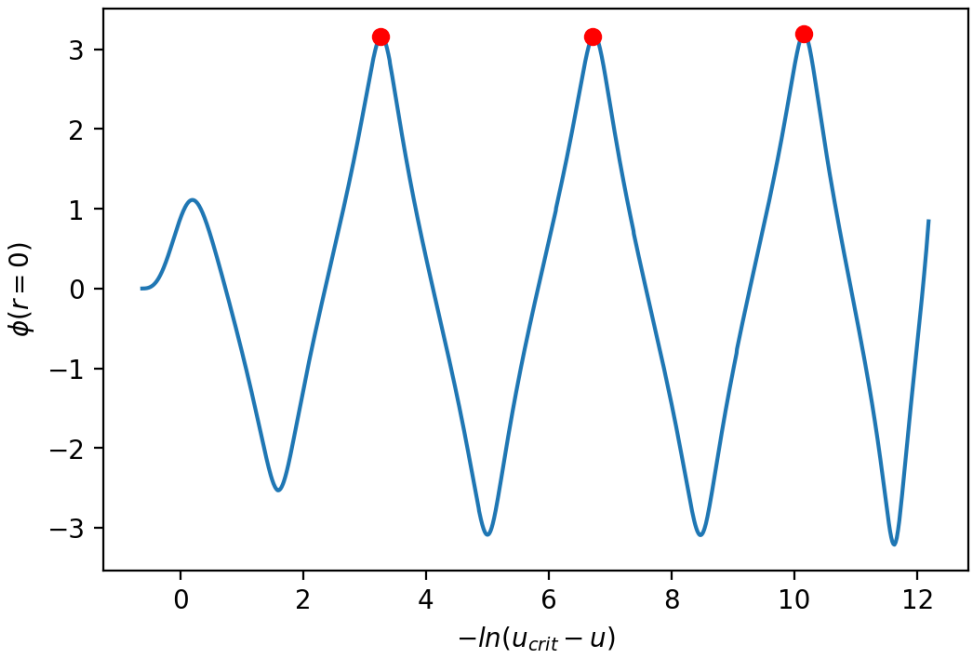

Figure 5.6: Self-similar behaviour of the scalar field at $r = 0$ before black hole formation with an initial amplitude close to the critical case.

at $v = 3$. The difference is taken between the fields with four consecutive resolution increases. In addition, the higher resolution differences are plotted multiplied by the expected order of convergence, which in this case is just first order. Thus, on the left, one can see that the curves overlap almost exactly to the naked eye, showing a very good convergence for the scalar variable $\Phi(u, v)$ at all points on the grid.

On the right, the convergence of the metric variable $\sigma(u, v)$ is similarly apparent, however, the curves do not overlap exactly. This shows that a small systematic error is present in the simulation. This might be the cause of the approximate boundary conditions (relying on the function's symmetry with respect to $r(u, v)$. Nevetheless, these show good convergence as well at the expected rate, which is first order.

Let us now turn to the point-wise convergence of some of the quantum mode functions. In Figure 5.8 I plot the point-wise convergence for two specific quantum

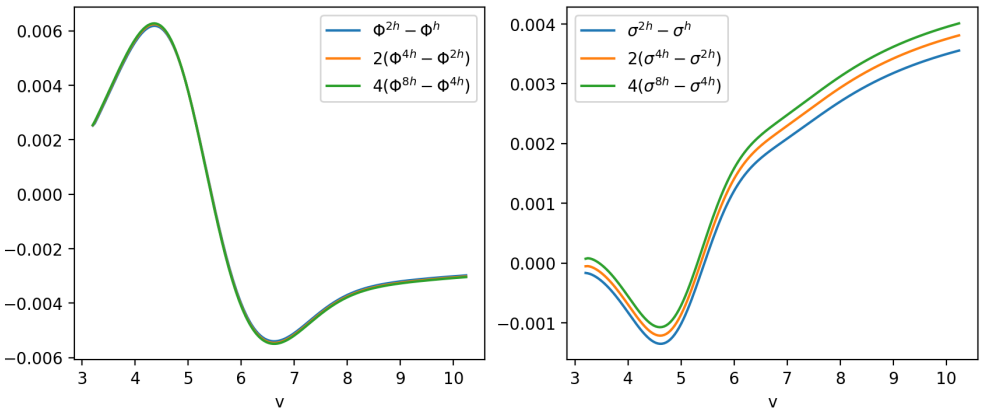

Figure 5.7: Point-wise convergence of the scalar variable Φ (left) and metric variable σ (right). Both show first order convergence as expected. These are taken from the no black hole evolution simulations and are snapshots of constant u slices, from around $u = 3$.

modes, one with $l = k = 10$ and one with $l = k = 20$. This is to highlight how quantum modes with larger l-values diverge quicker due to numerical instabilities at and around $r = 0$. The Figure shows four plots, in the first row, the two quantum mode functions are plotted at $u = 0.8$, $l = 10$ on the left and $l = 20$ on the right, whereas on the bottom row these are plotted at a later advanced time $u = 1.6$. Again, this is to highlight the change in convergence as the evolution commences.

Looking at the first row, one can see good convergence for both of the quantum modes, as the curves overlap fairly well. However, on the $l = 20$ plot a numerical instability can already be observed at $r = 0$, manifesting as a sharp change in errors. Still, the rest of the $l = 20$ quantum mode seems to be converging well.

Now focusing on the bottom row, at a later advanced time $u = 1.6$, the situation is different. On the left, the $l = 10$ mode still shows good convergence, albeit small discontinuities are arising on the boundaries of the grid. For the $l = 20$, on the other hand, there is no convergence at all at any point on the grid now. Namely, observing the range of values on the y-axis, the amplitude of the error difference for the orange curve is now of the order of 10^{-8}, which is six orders

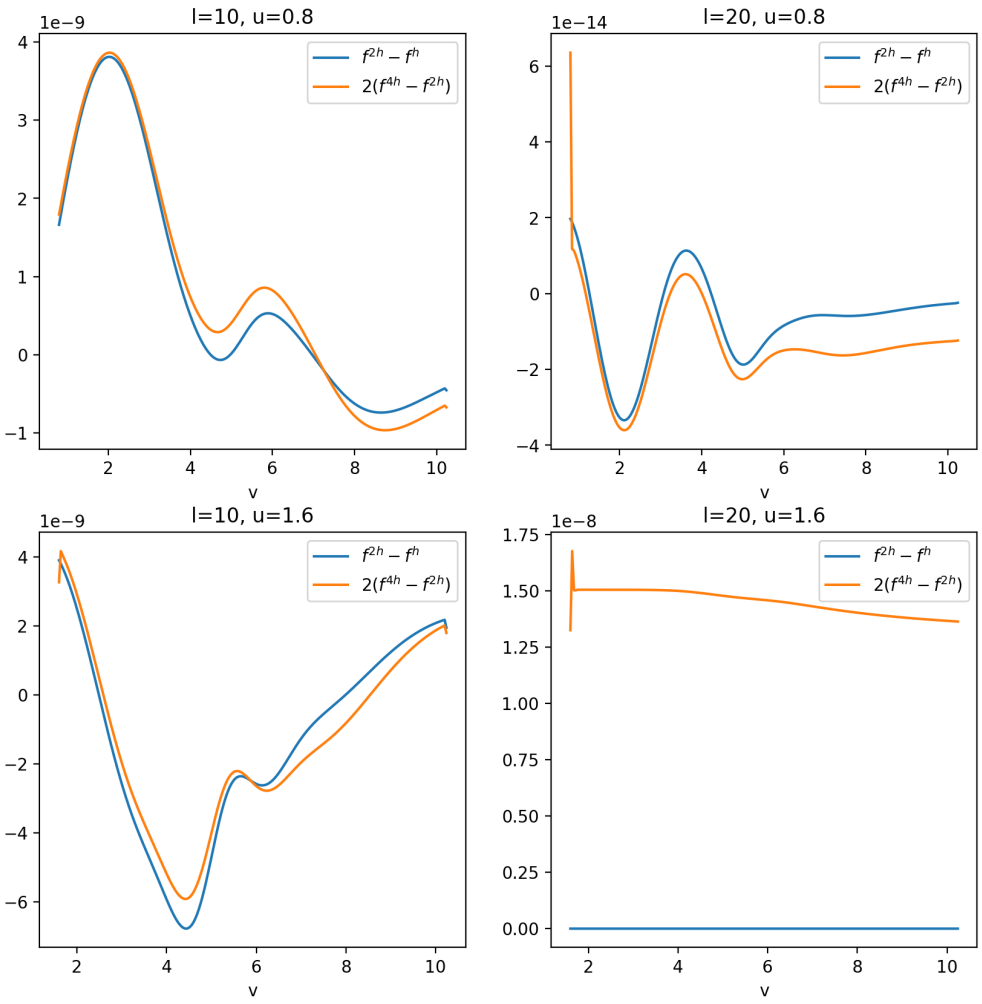

Figure 5.8: Point-wise convergence of quantum mode variables f_l with $l = 10$ (left) and with $l = 20$ (right) at two different advanced time instances, $u = 0.8$ and $u = 1.6$. Both modes show first order convergence at $u = 0.8$, however, at later time, the mode with $l = 20$ diverges due to numerical instabilities. These are taken from the no black hole evolution simulations.

of magnitude larger than at the previous time in the upper row, of 10^{-14}. This illustrates how quickly the quantum mode functions can diverge after a numerical instability appears. Thus this analysis shows how quantum mode functions with larger l-values diverge during the evolution and spoil the dynamics taking place.

5.8 Summary

In this chapter I have introduced a semiclassical simulation of gravitational collapse of a quantum scalar field in a double null formulation that includes the centre, $r = 0$, in the grid from the start of the simulation. This method is largely based on the classical formulation of this system in [54]. This method creates a physical space that is naturally focusing towards the centre, making it an ideal method to study Choptuik scaling.

I have presented the classical system and promoted it to a semiclassical one, adding quantum mode variables to the dynamical system. I have shown results of the full semiclassical simulation. These include a small number of quantum mode functions ($N_{mode} = 100$), due to the fact that quantum modes with larger l-values become numerically unstable and spoil the simulations. This can be explained by the low order of accuracy of the simulations, as these are first order systems.

Nevertheless, I have illustrated how the classical version of this simulation can be used to analyse Choptuik scaling and the self-similar behaviour of the dynamical fields. In addition, I have validated the simulations with convergence tests for both the classical variables and the quantum modes, illustrating the numerical divergence with larger l-value quantum modes.

Chapter 6

Quantum collapse without $r = 0$

6.1 Introduction

In the previous chapter a double null simulation was introduced where the point $r = 0$ is part of the numerical domain from the beginning. However, generally, this does not have to be the case when dealing with characteristic initial conditions. In fact simulations can be constructed where $r = 0$ is not part of the numerical domain at all, even after evolving the initial slice. This was done, for example, in [5] where the authors study charged black holes.

Thus, in this chapter, we introduce a similar system to the one in the previous chapter, with the difference that $r = 0$ is not present in the numerical grid at all. This creates a qualitatively different numerical system due to the fact that in this case the inner boundary will be null, just like the outer boundary. Recall that in the previous chapter, the inner boundary was $r = 0$, which is a time-like surface. Thus, the boundary conditions are not given by the symmetry conditions of the dynamical fields around the origin. Instead, they are determined by another initial null hypersurface ($v = constant = 0$) perpendicular to the ingoing initial

null hypersurface ($u = constant = 0$) from the previous chapter. This second null hypersurface then corresponds to outgoing null lines. The initial conditions on this hypersurface are essentially determined by the fact that no extra matter enters the numerical domain from it.

The advantage of a system that does not contain $r = 0$ in the case of our semi-classical simulations is that it creates an opportunity to remove the numerical instabilities stemming from the quantum mode equations of motion (due to the $1/r$ terms). Simply removing the close vicinity of $r = 0$ is not necessarily sufficient, however, as instabilities can occur increasingly far from $r = 0$ as one increases the order of spherical harmonics, i.e. the l-value. Nevertheless, using the characteristic formulation of Einstein equations, one can determine empirically how far from $r = 0$ is it sufficient to go in order to reach a stable simulation for all quantum modes in the system.

Another advantage, comparing to the ADM formulation, is that it is significantly easier to study the long term behaviour of quantum effects around the horizon of a black hole. In the ADM formulation, to simulate the horizon for longer one needs to increase the initial grid and also evolve further in time. In contrast, in a double null formulation, one needs to do only the former, as the event horizon is located at a constant retarded time coordinate u.

The disadvantage of getting rid of $r = 0$ in the full simulation (initially $r = 0$ is not present, but also we never evolve the initial grid long enough to reach $r = 0$) is that one loses the ability to create arbitrarily small black holes. This is because an initial matter field does not have the opportunity to get reflected off the central axis and dissipate to infinity, like we have seen in previous simulations. Thus this method is not suitable to study Choptuik scaling classically or semiclassically.

The main objective thus, using this system, is not to study the backreaction of the quantum effects and the potential alteration of dynamics compared to classical

simulations (like in the case of Choptuik scaling), but rather to study the quantum effects around the created black hole. In other words, the main objective is to find numerical evidence for Hawking radiation.

This chapter is organised as follows. First the semiclassical system is introduced, which is quite similar to the system in the previous chapter, with the difference that it is not cast into a first order system. Then, the numerical methods are described, after which some results are discussed. The results include details of black hole formation and the study of correlation function. Following this some convergence tests are presented to validate the simulation. Lastly, the chapter is summarised.

6.2 Classical system

The line element is the same as in the previous chapter:

$$ds^2 = -e^{\sigma(u,v)}dudv + r^2(u,v)d\Omega, \tag{6.1}$$

where $d\Omega$ is the unit sphere. The Einstein equations and the evolution equation of the scalar field is exactly the same as in the previous chapter as well. The Einstein equations are

$$\partial_u\partial_v r = -\frac{\partial_u r\partial_v r}{r} - \frac{e^\sigma}{4r}\Big(1 - (\partial_\theta\Phi)^2\Big), \tag{6.2}$$

$$\partial_u\partial_v\sigma = \frac{2\partial_u r\partial_v r}{r^2} + \frac{e^\sigma}{2r^2}\Big(1 - (\partial_\theta\Phi)^2\Big) - 2\partial_v\Phi\partial_u\Phi, \tag{6.3}$$

$$\partial_u^2 r = \partial_u r\partial_u\sigma - \frac{1}{2}r(\partial_u\Phi)^2, \tag{6.4}$$

$$\partial_v^2 r = \partial_v r\partial_v\sigma - \frac{1}{2}r(\partial_v\Phi)^2, \tag{6.5}$$

and the evolution equation of the scalar field is:

$$\partial_u \partial_v \Phi = -\frac{1}{r}\Big(\partial_u r \partial_v \Phi + \partial_v r \partial_u \Phi\Big). \tag{6.6}$$

Since we exclude $r = 0$ from the simulation entirely it is not needed to recast the above equations to a first order form. This makes the classical simulation significantly simpler, as it has less dynamical variables than the system in the previous chapter. The dynamical fields then are just:

$$(\Phi, \sigma, r), \tag{6.7}$$

These dynamical variables are evolved using Eq.-s (6.6), (6.3) and (6.2), respectively. The rest of the differential equations coming from the Einstein equations, namely Eq.-s (6.4) and (6.5) are not used in the evolution equations, but remain constraint equations. These are important as they determine boundary conditions.

The initial conditions required for this system are qualitatively different from when $r = 0$ was involved in the simulation, since now the inner boundary of the physical grid is also a null line, just like the $u = 0$ initial hypersurface. These then in combination are the so-called characteristic initial conditions, involving two null surfaces perpendicular to each other.

Thus, the initial conditions on the $v = 0$ hypersurface must be specified. These are largely determined by the fact that I choose to have no outgoing scalar field configuration. Then, $\Phi(u, 0) = 0$ and also $\sigma(u, 0) = 0$. The radial variable $r(u, 0)$ can then be determined by Eq. (6.4) with some additional boundary conditions. More precisely, one needs two boundary conditions as Eq. (6.4) is a second order partial differential equation. The first choice is simply to specify $r(0, 0) = r_{min}$. The second choice is determined the first derivative of r with respect to u; $\partial_u r$. As there is no mass inside of r_{min} in these initial conditions, one must choose this

to correspond to flat spacetime. But in flat spacetime

$$u = t - r, \tag{6.8}$$

$$v = t + r, \tag{6.9}$$

which can be straightforwardly rearranged to

$$r = \frac{v - u}{2}. \tag{6.10}$$

Thus $\partial_u r(0,0) = -\frac{1}{2}$.

The initial conditions on the $u = 0$ hypersurface are the following. I specify an initial ingoing scalar field configuration; $\Phi(0, v)$. In addition, I choose $\sigma(0, v) = 0$, which is a standard choice in the literature [54]. Finally, $r(0, v)$ is determined by Eq. (6.5) with suitable boundary conditions supplied by initial conditions on the other null hypersurface corresponding to $v = 0$.

6.3 Semiclassical system

The full semiclassical system is built up similarly as in the previous chapter, using light front quantisation. The only difference being that the system does not need to be cast into a first order system, hence the only quantum mode variable is $f(u, v)$ in this case. Recall that the purpose of casting the system to first order equations in the previous chapter was to deal with numerical instabilities around $r = 0$. However, as this point won't be part of the numerical domain here, this is not needed.

The quantisation of the scalar field can be done in exactly the same fashion as in the previous chapter, and the derived equation of motion to the quantum mode

functions is the same as well. Thus this is not repeated in this chapter.

The semiclassical system is then built up by the classical variables in the previous section, with the additional dynamical quantum modes and their equation of motion, plus the expectation values of the bilinears of the scalar operator that appear in the evolution equations.

Thus, for this system the full list of dynamical fields is:

$$(r, \sigma, \Phi, f). \tag{6.11}$$

with λ, μ and μ_f being additional auxiliary variables, and of which all are functions of u and v.

The equations that will be used for the evolution are then the following:

$$\begin{aligned}
\partial_u\partial_v r &= -\frac{\partial_u r\partial_v r}{r} - \frac{e^\sigma}{4r}\Big(1 - \langle(\partial_\theta\Phi)^2\rangle\Big),\\
\partial_u\partial_v \sigma &= \frac{2\partial_u r\partial_v r}{r^2} + \frac{e^\sigma}{2r^2}\Big(1 - \langle(\partial_\theta\Phi)^2\rangle\Big) - 2\langle\partial_v\Phi\partial_u\Phi\rangle,\\
\partial_u\partial_v\Phi &= -\frac{1}{r}\Big(\partial_u r\partial_v\Phi + \partial_v r\partial_u\Phi\Big).\\
\partial_u\partial_v f &= -\frac{l+1}{r}\Big(\partial_v r\partial_u f + \partial_u r\partial_v f\Big) - \frac{l^2}{r^2}\Big(\frac{e^\sigma}{4}(1 - \langle(\partial_\theta\Phi)^2\rangle) + \partial_u r\partial_v r\Big) f - \frac{1}{4}m^2 e^\sigma f.
\end{aligned} \tag{6.12}$$

The remaining Einstein equations act simply as constraint equations for the dynamical system. Note that the bilinears of the quantum field now are in expecta-

tion values and these are calculated by the following equations:

$$\begin{aligned}
\langle\chi|\,\hat{\Phi}\hat{\Phi}\,|\chi\rangle &= \Phi\Phi + \frac{\hbar c^2}{4\pi}\int dk \sum_{l=0}^{N_l-1}(2l+1)\left|\tilde{f}_{k,l}\right|^2,\\
\langle\chi|\,\partial_u\hat{\Phi}\partial_u\hat{\Phi}\,|\chi\rangle &= \partial_u\Phi\partial_u\Phi + \frac{\hbar c^2}{4\pi}\int dk \sum_{l=0}^{N_l-1}(2l+1)\left|\partial_u\tilde{f}_{k,l}\right|^2,\\
\langle\chi|\,\partial_v\hat{\Phi}\partial_v\hat{\Phi}\,|\chi\rangle &= \partial_v\Phi\partial_v\Phi + \frac{\hbar c^2}{4\pi}\int dk \sum_{l=0}^{N_l-1}(2l+1)\left|\partial_v\tilde{f}_{k,l}\right|^2,\\
\langle\chi|\,\partial_u\hat{\Phi}\partial_v\hat{\Phi}\,|\chi\rangle &= \partial_u\Phi\partial_v\Phi + \frac{\hbar c^2}{4\pi}\int dk \sum_{l=0}^{N_l-1}(2l+1)\frac{1}{2}(\partial_u\tilde{f}^*_{k,l}\partial_v\tilde{f}_{k,l} + \partial_u\tilde{f}_{k,l}\partial_v\tilde{f}^*_{k,l}),\\
\langle\chi|\,\partial_\theta\hat{\Phi}\partial_\theta\hat{\Phi}\,|\chi\rangle &= \frac{\hbar c^2}{4\pi}\int dk \sum_{l=0}^{N_l-1}(2l+1)\left|\tilde{f}_{k,l}\right|^2 sin^2\theta,
\end{aligned} \tag{6.13}$$

where the last bilinear does not have a "classical" part, since the scalar field is classically not dependent on θ. These bilinears are regularised using Pauli-Villars fields as in the previous chapters. The evolution equations are supplemented by initial conditions and boundary conditions described in the previous sections in order to create the full numerical system.

Note that for the quantum modes and regularisation scheme, the same parameters are used as in Chapter 2 (minimum wavenumber dk, ghost mass M_{PV}), and hence the vacuum plots would look exactly the same, but in double null coordinates. Hence these plots are omitted from this chapter.

6.4 Numerical methods

The main numerical technique used is a diamond evolution presented in [5]. The physical spacetime is uniformly discretised with the grid spacing in the ingoing and outgoing directions being equal; $du = dv$. As mentioned before the coordinate u acts as the time coordinate, which means that I evolve constant u surfaces. The

numerical grid constitutes of these hypersurfaces with coordinates from v_0 to v_{max} and from u_0 to u_{max}.

The numerical evolution is driven by a diamond evolution approximating the operator $\partial_u \partial_v$ in the following manner. Consider the grid element depicted in Figure 6.1. The aim is then to approximate the partial operator mentioned at point 0. For the sake of simplicity, let us use a generic function f as a representation of the collection of dynamical variables: Φ, σ, r. One can write this operator acting on this function f as:

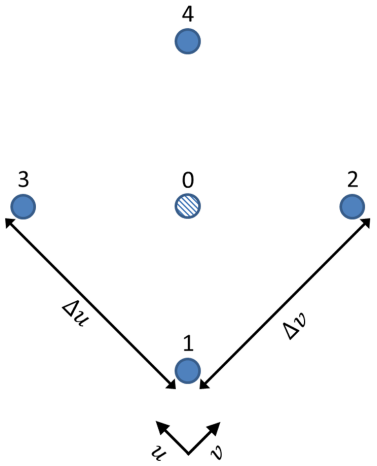

Figure 6.1: Element of the numerical double null grid. Figure taken from [5].

$$\partial_u \partial_v f = F(f, \partial_v f, \partial_u f). \tag{6.14}$$

To second order accuracy the left hand side can be approximated as:

$$\partial_u \partial_v f \simeq \frac{f_4 - f_3 - f_2 + f_1}{dudv}, \tag{6.15}$$

where the subscript denotes at which point the function is evaluated. Then at point 0 one must approximate the first order partial derivatives inside F as well.

At second order accuracy these are:

$$\partial_u f \simeq \frac{f_3 - f_1 + f_4 - f_2}{2du}, \tag{6.16}$$

$$\partial_v f \simeq \frac{f_4 - f_3 + f_2 - f_1}{2dv}. \tag{6.17}$$

Thus, substituting these expressions to Eq. (6.15) yields an algebraic equation for f_4; the function at point 4.

In practice, however, this algebraic equation might be non-linear, thus the numerical method uses instead a predictor-corrector scheme. This involves initially approximating the partial derivatives in Eq.-s (6.16) to a first order accuracy and using these to find a temporary value for f_4. This is then used to find the second order accurate partial derivatives and thus these are used to find the corrected value of f_4 using Eq. (6.15).

6.5 Results

In this section I will present results of semiclassical simulations for both subcritical and supercritical cases. The backreaction in these simulations was turned off, meaning that the quantum mode functions did not contribute to the stress-energy tensor components. Nevertheless, the quantum modes were evolved and create observable quantum effects. The lack of backreaction simply makes a generally more numerically stable simulation, as the potential instabilities of the quantum mode functions do not influence the other dynamical fields. In Chapter 2 it has been established that the backreaction in these simulations does not change the dynamics qualitatively and have a small effect overall. The backreaction might cause qualitative difference for relatively small black holes (smaller than studied in Chapter 2 during the Choptuik scaling analysis), as quantum effects like Hawking radiation are inversely proportional to the resulting black hole mass. However, in

this chapter, the resulting black holes are relatively large, as the scalar field does not have the opportunity to reflect from $r = 0$ and partially escape.

The results shown in this section are all coming from semiclassical simulations involving quantum modes with $N_l = 100$ and $N_k = 50$, meaning a total of $N_{mode} = 5000$. In simulations of the previous chapters the number of l and k modes were held equal, however, as here the physical grid is away from $r = 0$, it is beneficial to create a larger area where the quantum field is well-defined. This is exactly the effect of setting N_l to be larger than N_k, as shown in Chapter 2. Thus, using twice as many l-values as k-values doubles the physical grid where the quantum field is well-defined. In addition, since $r = 0$ is not part of the grid here, modes with higher l-values (and hence more unstable evolutions) can be part of the simulation too, as it will be shown in the next section.

The exact initial conditions for the simulations presented here are the following. The expectation value of the scalar field, Φ, is a Gaussian lump located at $v = 3$ with unit width. The amplitude of the initial scalar field is varied between $a = 0.1$ and $a = 0.3$ to create subcritical and supercritical evolutions. The metric variable σ is zero at the initial slices, as explained before. The last choice is the initial radius at $u = v = 0$, which is chosen to be $r = 5$. In addition, the constant step size is $du = dv = h = 0.01$ and $N_{grid} = 1001$.

The structure of this section is the following. I will first present results of the dynamics of some metric variables and scalar variables during the simulations of subcritical and supercritical cases of the scalar field evolution. Then I will present results of the quantum effects created during these simulations by examining the bilinears of the matter field. Lastly, some correlation functions of the scalar field will be studied, as these could include the smoking gun of Hawking radiation.

6.5.1 Black hole formation

Let us begin with the evolution of the metric function $r(u, v)$ for both subcritical and supercritical cases. It is most informative to plot the evolution of this metric variable, as the condition of

$$\partial_v r = 0, \tag{6.18}$$

signals the formation of an apparent horizon in the simulation. The largest r that this equation is true for is said to be the apparent horizon radius that asymptotically approaches the event horizon. Thus, black hole formation can be easily seen on evolution plots of $r(u, v)$.

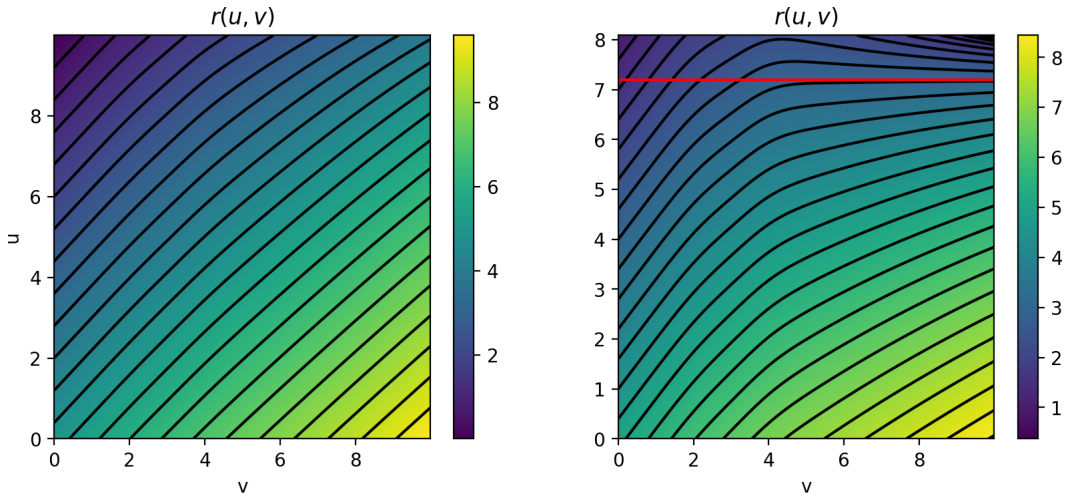

Figure 6.2: Evolution of the radius $r(u, v)$ in cases when there is no black hole forming and when there is a black hole forming. The amplitude of the initial field in the second case is increased to achieve supercriticality. Note that these figures contain a heatmap together with a mesh that correspond to lines of constant values.

Hence, the evolution of $r(u, v)$ is shown for the two simulations in Figure 6.2. The only difference in the simulations resulting in the plots on the left and right is that the initial amplitude of the scalar field is doubled in the second case. These figures are similar to the $r(u, v)$ figures in the previous chapter, Figure 5.3, with the difference that the full computational grid is part of the dynamics, rather than

just the lower triangular half.

In the plot on the left one can observe the constant lines of r being very close to 45°, showing that the geometry is close to a flat spacetime. The simulation here stops when the $v = 0$ grid point reaches $r = 0$, at around $u = 10$. Only at the very top of the plot, at late advanced time, can one see the constant r lines bending slightly, as the scalar field approaches the centre. Note that as the initial central radius at $u = v = 0$ is $r_0 = 5$, meaning that close to Minkowski evolutions reach $r = 0$ at around $u = 10$, which means the evolution here is terminated there.

The plot on the right of Figure 6.2 shows the evolution of $r(u, v)$ when a black hole forms. One can see that already at the initial null hypersurface at $u = 0$ the constant r lines bend away from 45° outside of the scalar field at $v = 3$. The constant r lines are 45° inside of the scalar field, as the inside geometry is Minkowski. As the evolution commences, the constant r lines approach a horizontal line slowly, and at around $u = 7$ an apparent horizon forms. The red line on this plot illustrates the event horizon, as the constant r line there is essentially horizontal.

Now, let us look at the evolution of the expectation value of the scalar field, which coincides with the evolution of a classical scalar field. This is shown in Figure 6.3. Both cases, no black hole evolution on the left, black hole evolution on the right, show similar behaviour. The initial amplitude in the former case is $a = 0.12$ and 0.24 in the latter case. As all data on the initial null surface of $u = 0$ is necessarily ingoing, and the scalar is massless, the scalar field in both cases simply propagates in a straight line in these coordinates towards $r = 0$. The only difference is that, due to the heavily non-linear dynamics during the black hole formation case, some of the scalar gets reflected in that case during the evolution (illustrated by the dashed lines that are close to horizontal).

In order to probe the quantum effects in the system I have plotted the fluctuations

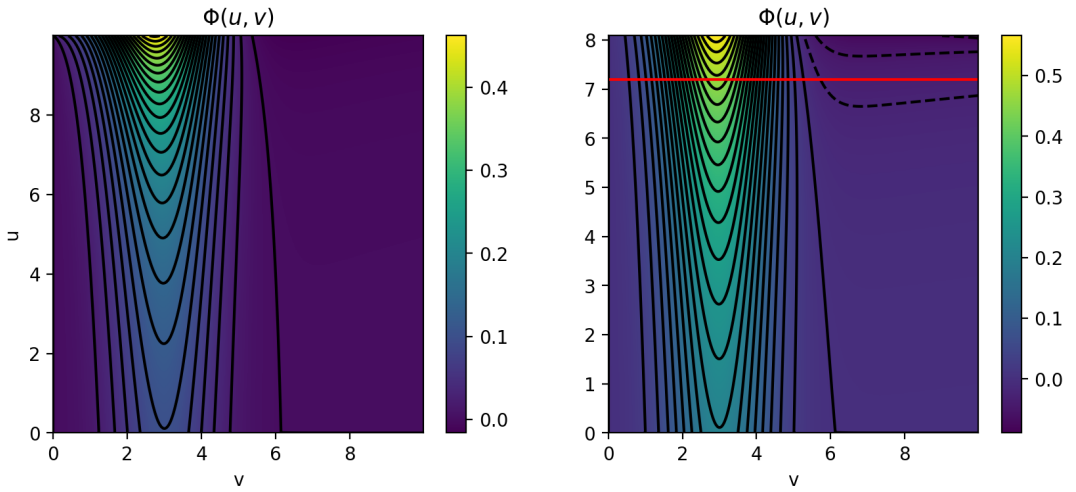

Figure 6.3: Evolution of $\Phi(u, v)$ in cases when there is no black hole forming and when there is a black hole forming. The amplitude of the initial field in the second case is increased to achieve supercriticality. Note that these figures contain a heatmap together with a mesh that correspond to lines of constant values.

of the two-point function of the scalar field, defined by

$$\Delta\langle\Phi^2\rangle = \Delta\langle\hat{\Phi}\hat{\Phi}\rangle = \langle\hat{\Phi}\hat{\Phi}\rangle - \langle\hat{\Phi}\rangle\langle\hat{\Phi}\rangle. \tag{6.19}$$

These are plotted for both sub- and supercritical cases in Figure 6.4. Note that in the supercritical case the resulting black hole is larger than in the figures above in order to see deeper inside the apparent horizon, as in Figure 6.2 and 6.3 only a small area inside the horizon can be seen. Thus, the amplitude of the initial scalar expectation value is $a = 0.12$ and $a = 0.3$ for the two cases.

In the plot on the left, when no black hole forms, one can see small fluctuations (order of 10^{-4}) almost everywhere on the plotted grid. These are largest, however, at the very beginning and at the very end of the simulation. At the beginning, around $u = 1$, there is a larger positive fluctuation, resulting in some ingoing and some outgoing fluctuations. At the very end, around $u = 9$, there are larger negative fluctuations, which can be explained by the fact that the scalar field expectation value itself is increasing as it approaches $r = 0$. As expected, they are almost zero inside of the scalar field (inside $v = 2$), as this essentially corresponds

to Minkowski spacetime.

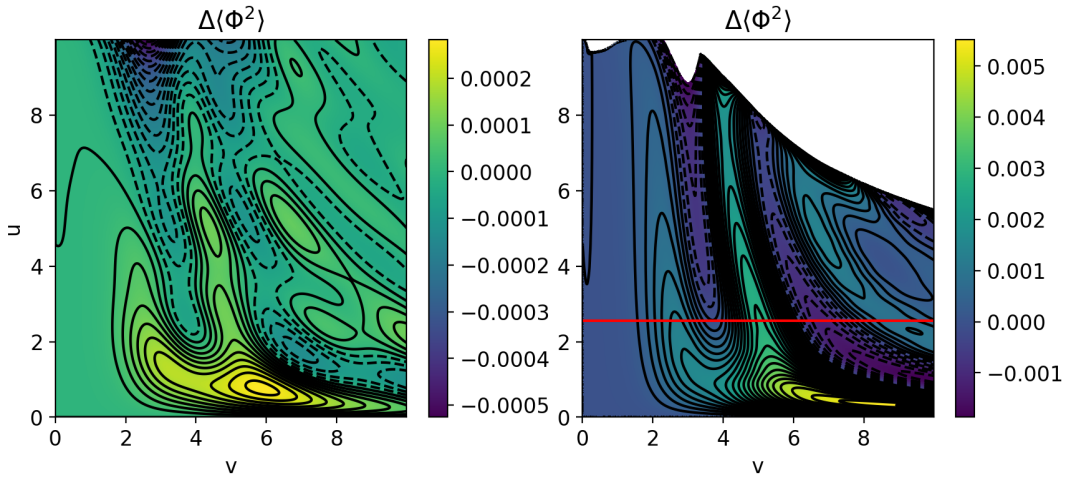

Figure 6.4: Evolution of the fluctuations of the bilinear of $\Phi(u, v)$ in cases when there is no black hole forming and when there is a black hole forming. The amplitude of the initial field in the second case is increased to achieve supercriticality. Note that these figures contain a heatmap together with a mesh that corresponds to lines of constant values.

In the graph on the right of Figure 6.4, the plot shows similar characteristics. Note that the event horizon is illustrated as a red line, and one can also see the singularity entering the grid from v_{max} at $u = 5$. The plot shows fluctuations arising at the beginning of the evolution and producing both ingoing and outgoing components (vertical and horizontal respectively). Notice that the amplitude of these fluctuations are more than an order of magnitude larger than in the no black hole case, even though the initial amplitude of the expectation value of the scalar is just three times larger here. In addition, it can be seen that the fluctuations do not simply become smaller after the fluctuations arising at the beginning, but they are growing as they approach the singularity.

An extremely useful characteristic of these double null simulations is that in case of black hole evolutions, if one would like to observe the later time dynamics, one just needs to increase the v-grid, as the horizon stays at a constant u. Hence, the dynamics need not to be evolved to later (advanced) times.

Hence, to see the late time behaviour of these quantum fluctuations I plot the

same evolution as on the right side of Figure 6.4, but with a grid that has a larger v-grid. This can be seen in Figure 6.5, where the maximum v coordinate, instead of $v_{max} = 10$, is now $v_{max} = 40$. Here, it can be seen that indeed the fluctuations decrease after $v = 10$ and $u = 1.5$ (where the initial large fluctuations have travelled inwards and outwards), however, there are visible fluctuations remaining even at late times. However, whether or not these fluctuations have anything to do with Hawking radiation is unclear, and to check this, one way is to study some correlation functions.

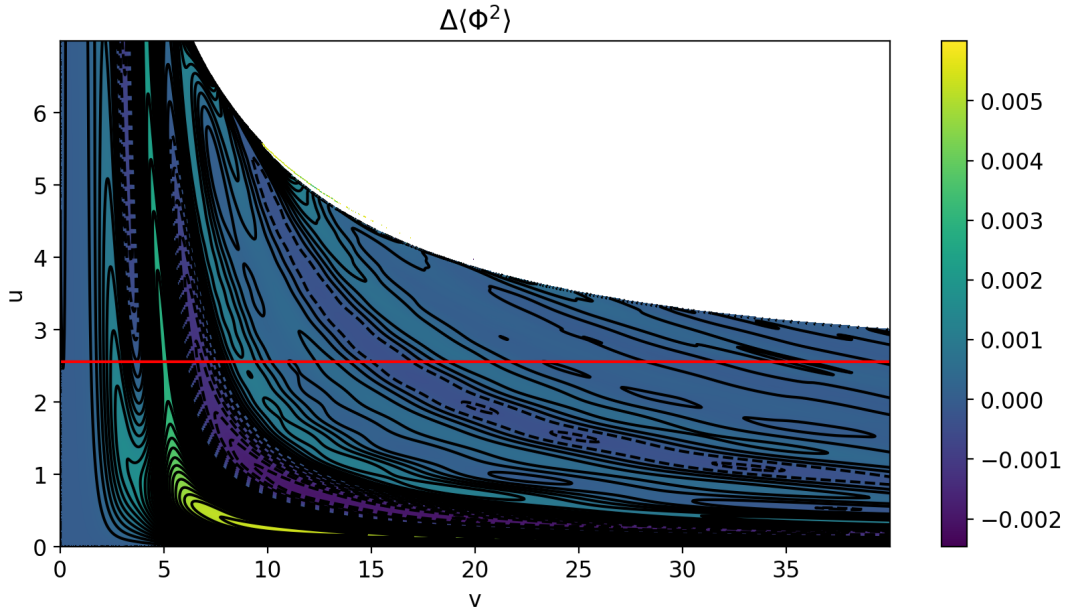

Figure 6.5: Long term evolution of the fluctuations of the bilinear of $\Phi(u, v)$ in cases when there is no black hole forming and when there is a black hole forming. The amplitude of the initial field in the second case is increased to achieve supercriticality. Note that these figures contain a heatmap together with a mesh that corresponds to lines of constant values.

6.5.2 Correlation functions

In order to check if there are any signs of Hawking radiation in these semiclassical simulations, correlation functions might be studied. This is due to the fact that Hawking radiation causes a long-range correlation between particles inside and outside of the horizon.

Correlation functions were analysed in Chapter 2 already, inspired by studies of correlation functions in analogue black hole simulations and experiments, e.g. [3]. However, the correlation functions there were equal-time correlators, which are the natural choice in an ADM formulation. Since in the double null simulations in this chapter the hypersurfaces are null, and the scalar field is quantised in a light-front manner, studying equal-time correlators becomes non-trivial.

Thus, instead of examining equal-time correlators, in this subsection I will study correlation between two null hypersurfaces. Sketches can be seen in Figure 6.6 illustrating how correlators might detect Hawking radiation in this scheme. On the left hand side, an illustration of an equal-time surface is presented (magenta line) that would capture the correlation between the outgoing (red) and ingoing (blue) Hawking quanta. On the right, the same situation is shown but instead of one equal-time surface, it shows two null surfaces; one constant v surface and one constant u surface.

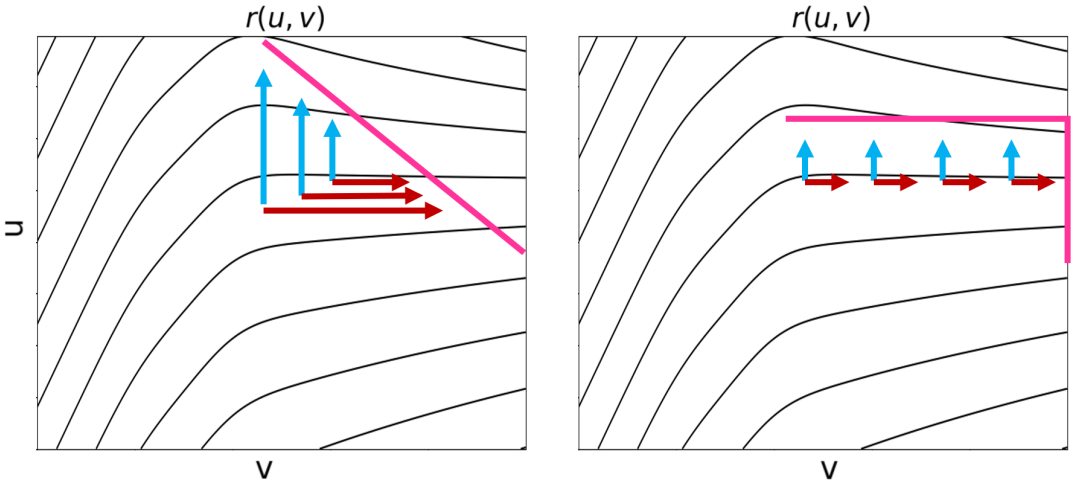

Figure 6.6: Sketch of ideal locations to study equal-time correlations (left) and correlations of null surfaces (right) in order to look for correlations between Hawking quanta.

A significant difference between the two methods of analysing correlation functions is that in the equal-time case, since it is a single hypersurface, the diagonal line on the correlation matrix would be showing short-range correlations, which is

expected even in flat spacetime. The long-range correlations would show up as off-diagonal lines starting from the location of the horizon (see Figure 2.9). In the case of null hypersurfaces, however, the only short-range correlation that would show up is the top right corner, as that is the only location where the two surfaces intersect; see the magenta lines on the right hand side of Figure 6.6.

Thus, I study correlation functions of null hypersurfaces. To illustrate where exactly the studied surfaces are located, I plot the $r(u, v)$ evolution. This is plotted in Figure 6.7. This, again, is a slightly different evolution than in the sections before, as the initial amplitude of the scalar field expectation value was set to be $a = 0.27$. This is so that there is an adequate amount of spacetime between the initial $u = 0$ surface and the apparent horizon, $u = u_{AH}$, surface. But also so that the apparent horizon does not form too late, where the quantum mode functions might become unstable. The red line in Figure 6.7 illustrates the event horizon, and the magenta lines show the null hypersurfaces where correlation was studied.

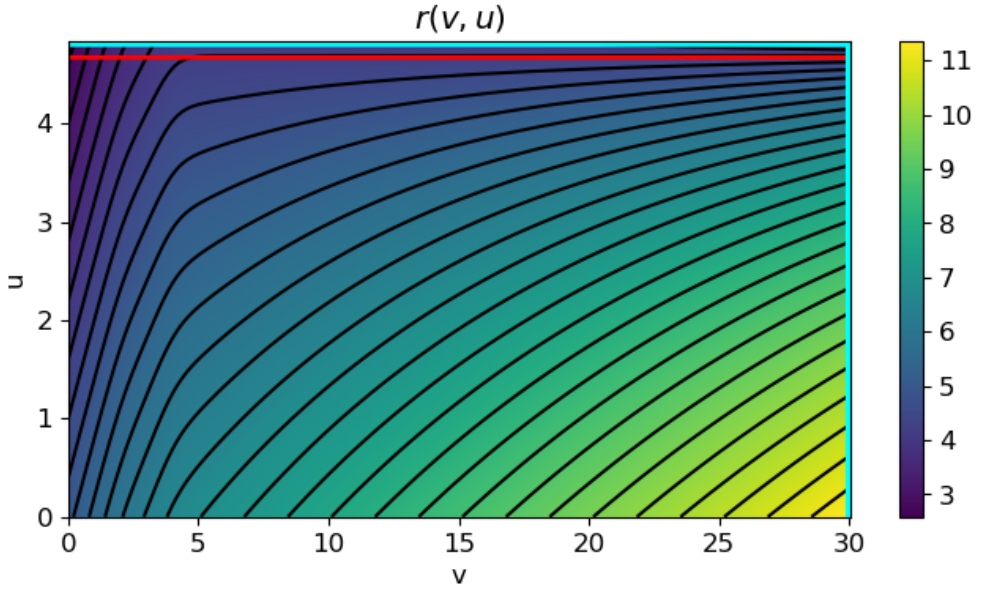

Figure 6.7: Evolution of $r(u, v)$ in a scenario where correlation functions are studied. The red line corresponds to the event horizon (which is just the largest apparent horizon) and the cyan lines correspond to the hypersurfaces between which correlation is studied.

A crucial consequence of the fact that the correlation is studied between two null hypersurfaces that only intersect at one point, is that these do not necessarily require regularisation. This is because *apriori* the correlation function of a scalar field is only divergent in the coincidence limit, and is finite away from that, meaning between two separated points. Hence, one only expects the top right corner of a correlation function between the (magenta) null hypersurfaces on Figure 6.7 to be divergent.

The correlation function is defined as follows:

$$\begin{aligned}\Delta\langle\Phi\Phi\rangle &= \Delta\langle\hat{\Phi}(u_1,v_1)\hat{\Phi}(u_2,v_2)\rangle \\ &= \langle\hat{\Phi}(u_1,v_1)\hat{\Phi}(u_2,v_2)\rangle - \langle\hat{\Phi}(u_1,v_1)\rangle\langle\hat{\Phi}(u_2,v_2)\rangle.\end{aligned} \tag{6.20}$$

Therefore, the correlation function between said null hypersurfaces is plotted for the regularised and also non-regularised simulations in Figure 6.8. This figure shows regularised (left) and non-regularised (right) correlation matrices. In the first row, these are shown on the full grid, meaning between $u = 0$ to $u = 5$ and $v = 0$ to $v = 30$. In the second row, the same plots are presented, but only between $v = 0$ and $v = 20$, in order to avoid the divergence at the coincidence limit; the intersection of the hypersurfaces. Note that the event horizon is plotted as a black line on these plots.

In the first row of Figure 6.8 one can see that the not regularised version of the correlator has a peak at the top right corner, which is what is expected as in theory, the correlator is divergent there. However, as there is a finite number of quantum modes in this system, it is not infinite, but an order of magnitute larger than the regularised version.

The top left graph shows the regularised correlator, and here one can observe some meaningful features. Firstly, note that long-term correlations are indeed shown in

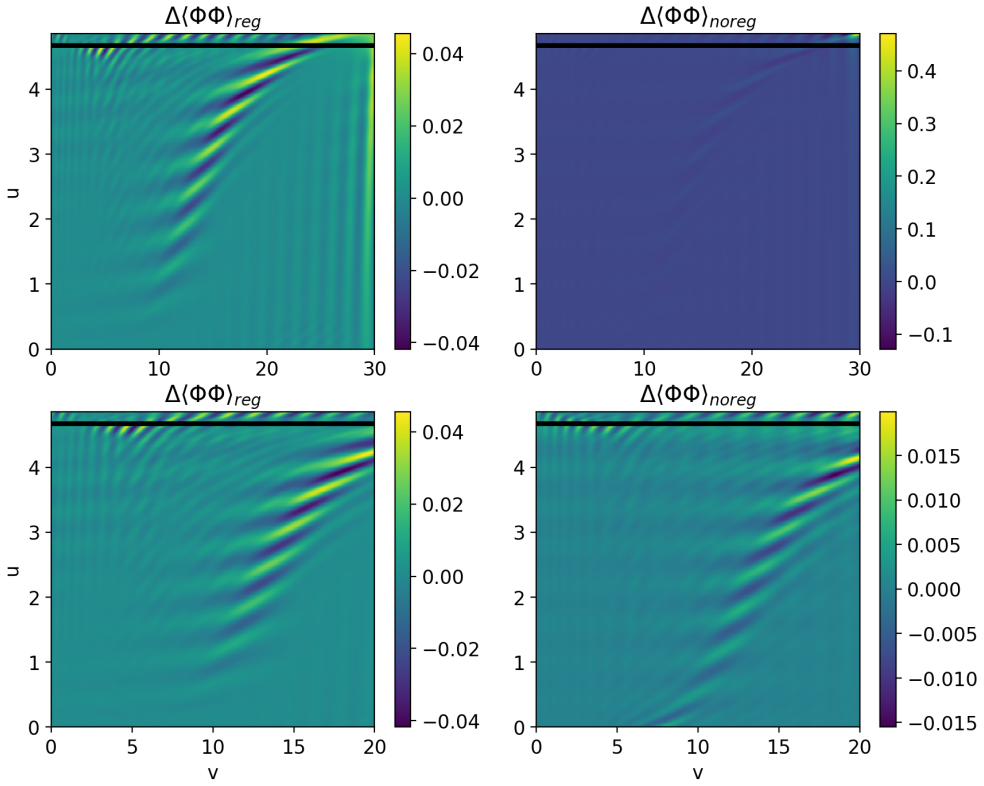

Figure 6.8: The fluctuation part of the correlators of the quantum scalar on the hypersurfaces on Figure 6.7. The left hand side corresponds to the regularised correlators and the right hand side to the non-regularised versions. The only difference in the first and second row is the limits on the x-axis on v; $v_{max} = 30$ and $v_{max} = 20$, respectively. This is to illustrate how, away from the divergence in the non-regularised correlator, the two correlators match qualitatively.

this graph. There are two distinct curves one can differentiate both starting at the top right corner. The first is a horizontal line just above the horizon, and the second is a curve moving towards the bottom left.

On the bottom row one can compare the regularised and non-regularised versions of the correlation matrix, since the divergent part of the latter correlator is omitted from the graph. It can be seen that indeed the two graphs show the same qualitative features, however, quantitatively, the regularised version has larger amplitudes, shown on the colour bar.

The expected signal of Hawking radiation in these correlation functions, according to the right graph in Figure 6.6, is that there should be correlation between a

constant u just outside of the event horizon and all values of v after the horizon has formed. In the plots in Figure 6.8 these would manifest as a horizontal line at around $u = 4$ starting from $v = 5$ to $v = 30$. This is quite different from what Figure 6.8 shows. Thus, it can not be concluded that the correlations found here correspond to Hawking radiation.

6.6 Convergence tests

In order to validate the semiclassical simulations in this chapter, convergence tests were conducted for both "classical" part of the simulations, and the quantum modes separately. This ensures that the results presented in the previous section are due to physical phenomena being present in the simulations rather than numerical errors.

Firstly, the value of the constraint equation in the v direction is plotted in Figure 6.9 for increasingly high resolutions. Namely, these have $dv = du = h$ with $h = 0.01$, $h = 0.02$ and $h = 0.04$. This is done for a typical subcritical simulation with a significant amplitude. On the left the value of the constraint equation is plotted for these three resolutions at the final advanced time step for all v. It can be seen that these converge towards zero. In order to inspect the order of accuracy of the system, the ratio of the difference between constraint equations with subsequent resolution are plotted. This is only plotted from $v = 4$, as before that the errors are dominated by random rounding errors. It can be seen that the ratio is close to four, which is exactly what is expected for a second order accurate numerical system.

In order to validate the quantum modes separately, the point-wise convergence of four different quantum modes are plotted. These modes are with values $(l = 10, k = 5)$, $(l = 30, k = 15)$, $(l = 50, k = 25)$ and $(l = 100, k = 50)$. To specifically

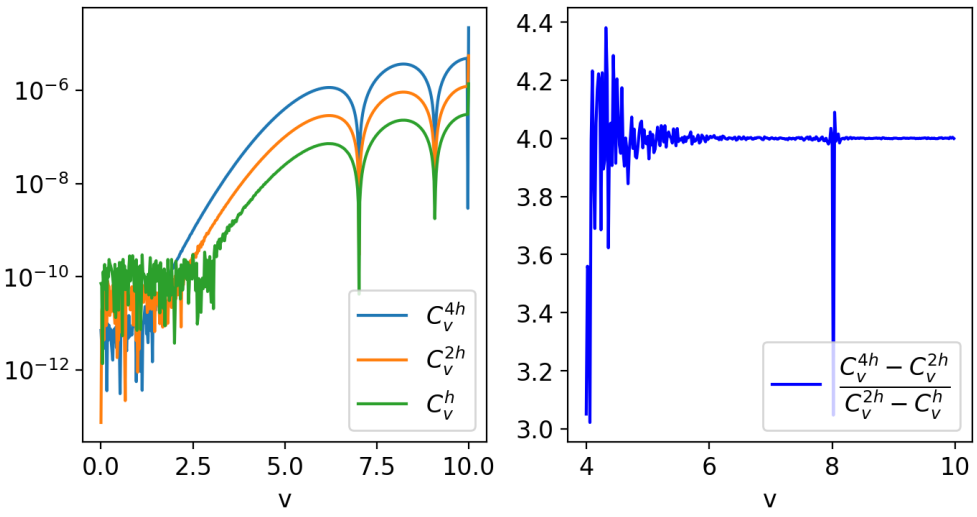

Figure 6.9: Convergence test on the classical simulation. The constraint equation in the v-direction is plotted for decreasing grid spacings on the left hand side. On the right hand side, the ratio of the differences between the constraints are taken in order to inspect the convergence rate of the simulation. As expected, the convergence rate is second order.

validate the quantum effects in the black hole formation evolutions, these modes are taken from the evolution plotted on the right graph in Figure 6.4, at advanced time $u = 2.5$, which is the location of the event horizon. The graphs start just after the apparent horizon has formed at around $v = 4$. Everything inside of this is approaching $r = 0$ much quicker than after the horizon has formed, and hence is more proned to numerical instabilities. Nevertheless, these do not affect the quantum modes after the apparent horizon has formed. Indeed, one can observe very good convergence for all modes, even the very high l-value ones. Thus, the quantum modes converge to a true solution at the expected second order rate.

This is astonishing and is in stark difference to the point-wise convergence analysis of the modes in the last chapter, namely in Figure 5.8. In addition, note that the order of magnitude of the amplitude of these quantum modes varies greatly. The top left mode has amplitude of order 10^{-12}, while the bottom right mode has amplitude at 10^{-75}. Even with this huge difference in orders of magnitude, these quantum modes show very similar convergence.

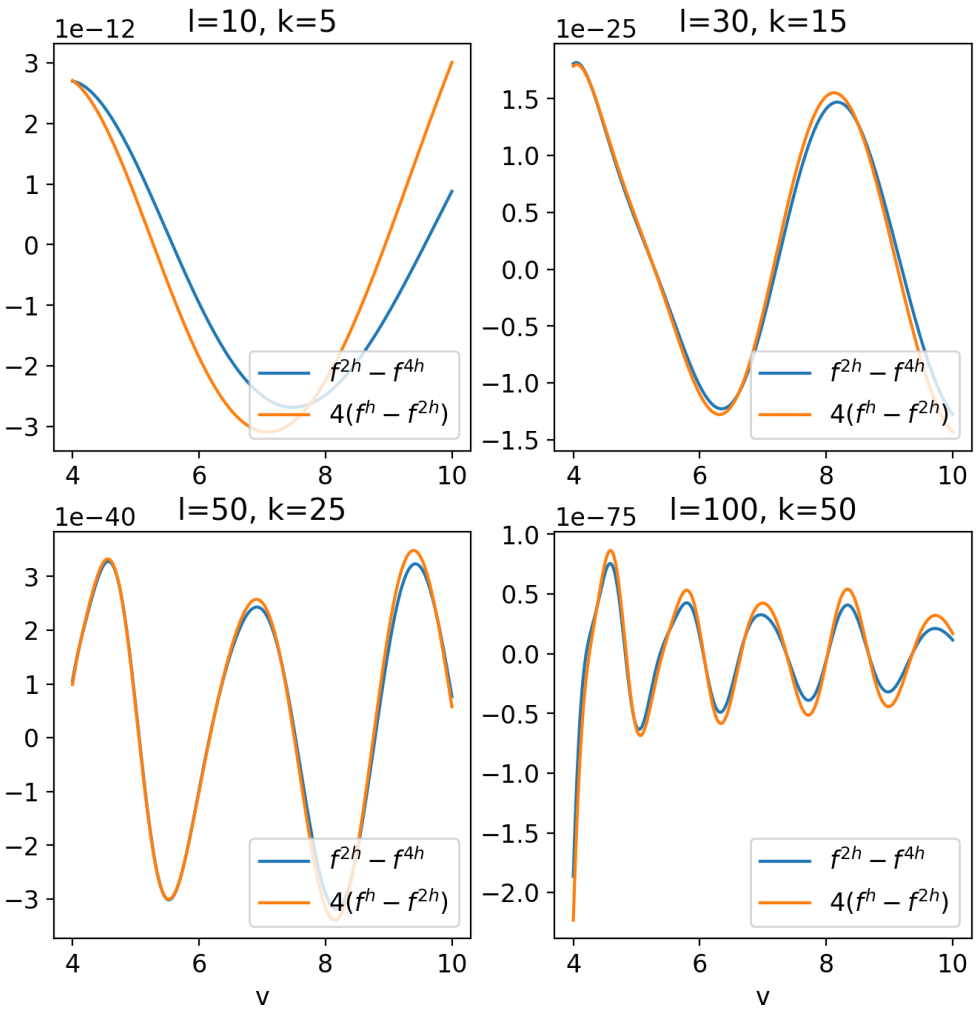

Figure 6.10: Pointwise convergence of some of the quantum mode functions. The difference between the solutions for simulations with decreasing grid spacings are plotted for two different cases on top of each other. These errors, as expected, are converging at a second order rate. The modes, from top left to bottom right, correspond to higher l- and k-values.

Lastly, as another way of validating the quantum effects shown in the previous subsection, in Figure 6.11 I plot the expectation value of the two-point function of Φ on both a constant u and a constant v hypersurface. These are plotted at $u = 2.5$ (left) and $v = 10$ (right) for simulations with increasing number of quantum modes. The number of modes for each curve is the following: $(N_l = 20, N_k = 10)$, $(N_l = 60, N_k = 30)$, $(N_l = 80, N_k = 40)$ and $(N_l = 100, N_k = 50)$. The graph on the right is only plotted until around $u = 5$, where the singularity is almost reached, and the modes start to diverge. In that region one does not expect

numerical convergence, as the numerical scheme inevitably breaks down.

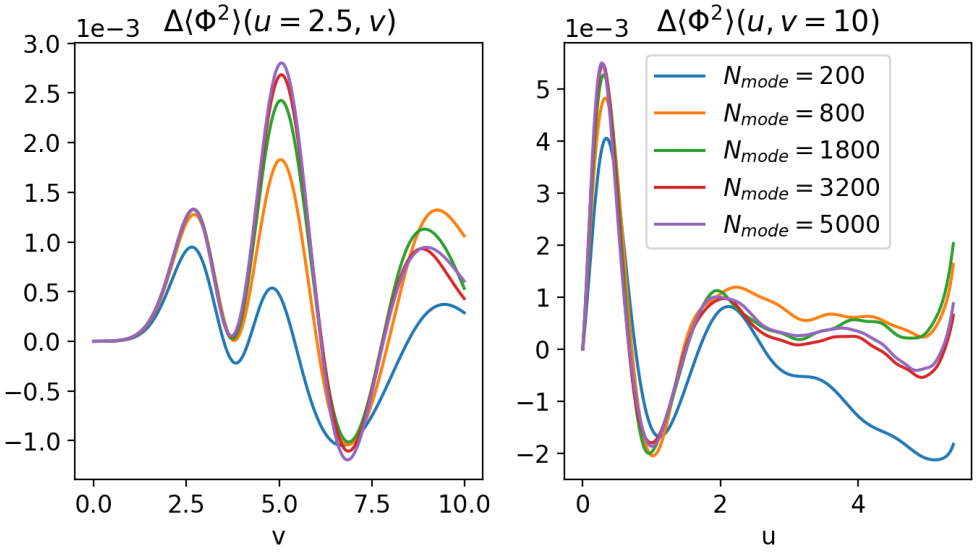

Figure 6.11: Convergence of quantum fluctuations in case of the square of the quantum scalar field. The fluctuations are plotted for simulations conducted with increasing number of mode functions, from as little as $N_{mode} = 200$ to $N_{mode} = 5000$. One can see that the fluctuations converge, and there is little difference between the fluctuations produced by $N_{mode} = 3200$ and $N_{mode} = 5000$.

It can be seen in both plots that the quantum effects converge well, and there is little difference between the curves with $N_{mode} = 3200$ and the one with $N_{mode} = 5000$.

Thus convergence has been shown for both classical variables, separate quantum modes and also quantum effects. This validates the simulations and their results whilst illustrating the increased numerical stability of the semiclassical simulations in double null coordinates away from $r = 0$ compared to the ADM formulation. Then, one can be confident that the quantum effects presented in the previous section - notably including the long-range correlations - are true physical effects in the system.

6.7 Summary

In this chapter a double null formulation of the semiclassical collapse of a scalar field has been presented. Results have been shown for both subcritical and supercritical simulations, including the fluctuations of the two-point function of the quantum scalar field and, in the supercritical case, correlation functions between points inside and outside of the formed black hole. Lastly, these findings and the simulation itself was validated by performing convergence studies of the classical variables, the separate quantum mode functions and also the resulting quantum effects (two-point function fluctuations).

This method proved to overcome the issue of numerical instabilities related to the quantum mode functions, especially the high l-value modes, since $r = 0$ is not present in the numerical grid at all, and the numerical grid only approaches its vicinity towards the end of the simulations.

Studying the correlation functions revealed long-range correlations that may point towards Hawking-like signals. However, these correlations are different from the expected long-range correlations coming from Hawking quanta, therefore it cannot be said that they are one and the same. Nevertheless, long-range correlations are present in these simulations, and more studies are needed to uncover the nature of these and their possible relation to Hawking quanta.

Lastly, looking at both regularised and non-regularised versions of the correlation functions, one can convince oneself that the presence of the ghost fields, even though their masses are finite, does not make a qualitative difference in the features of the correlations. Thus, validating the use of Pauli-Villars fields in semiclassical simulations as a regularisation scheme.

Chapter 7

Summary, conclusion and future work

7.1 Summary

In this thesis I presented multiple methods to simulate the gravitational collapse of quantum fields, and thus simulate semiclassical black holes. The thesis examined the ADM formulation of the Einstein equations first, in Chapters 2,3 and 4, and then the double null or characteristic formulation in Chapters 5 and 6.

The main body of the thesis started, in Chapter 2, with simulations using the ADM formulation of the Einstein field equations and finite difference methods as the chosen numerical scheme. Here quantum effects are detected and validated using multiple convergence studies. Choptuik scaling is shown to be present in semiclassical black holes, albeit it is still a question whether or not black holes closer to criticality obey it as well. Correlation functions were examined to look for signals of Hawking radiation, and even though some longer-range correlations were found, these cannot be attributed to Hawking quanta, as they don't show up

at the expected locations in the correlator.

Chapter 3 and 4 attempted to improve upon the original simulation by using spectral methods as a numerical scheme and using an ingoing boundary method, respectively. Spectral methods proved to be useful in that they require significantly fewer grid points to produce comparable accuracy as finite difference methods, however, they did not solve the problems of numerical instabilities of the quantum mode functions. In Chapter 4, the use of an ingoing boundary driven by a specifically chosen shift vector was successful to reproduce the periodic fine-structure of Choptuik scaling and study black holes much closer to criticality than before. However, as the numerical instabilities of the quantum mode functions spoil the full semiclassical simulation including backreaction, the semiclassical Choptuik scaling could not be studied with this system.

The later chapters take a different approach and, instead of the ADM formulation of the Einstein equations, the double null formulation is presented. Chapter 5 introduces a double null formulation where the centre of the spherical space is part of the simulation, thus creating a naturally ingoing grid that is ideal to study Choptuk scaling. Indeed, classical Choptuik scaling is reproduced to an even greater accuracy than in Chapter 4, however, the same issues persist regarding the quantum mode numerical instabilities that prevent the study of the semiclassical version of Choptuik scaling.

Lastly, Chapter 6 introduced a similar double null simulation as Chapter 5, constructed using the same evolution equations, however without including the centre of the spherical space. This creates a simpler simulation where the quantum modes stay stable for a longer time, as their numerical instabilities would arise precisely in the vicinity of the centre. This is then an ideal scenario to study quantum effects and correlation functions in the search for Hawking radiation signals. Indeed, it is shown that the quantum mode functions have a significantly better behaviour

than in any of the previous simulations and quantum effects are presented and validated. Correlation functions are studied as well, and although long-range correlations are found, it is debatable whether or not these correspond to Hawking radiation signals.

7.2 Conclusion

In this thesis I have presented the first simulations of a fully quantum mechanical scalar field collapsing, thus creating a semiclassical black hole. The main idea behind the formalism is the use of a coherent state as the quantum state, which creates a link between the well-established literature of classical collapse simulations and semiclassical simulations. Hence semiclassical simulations can be built upon the classical ones by adding extra quantum mode functions as dynamical variables that, together, essentially constitute the fluctuations around the coherent state expectation value.

I have shown that realistic semiclassical simulations can be created and true quantum effects can be found in the simulations. I did this by performing the same simulation with increasing number of quantum mode functions and showing how the resulting quantum effects converge. Albeit a very large number of quantum modes must be used (order of thousands) in order to capture the quantum effects properly. This makes the simulations computationally expensive both in terms of memory and computational time.

I have presented the first evidence for semiclassical Choptuik scaling, however, further investigation is required to examine semiclassical black holes closer to criticality. This has the potential to prove or disprove the statement that quantum effects stop naked singularities from forming, like the naked singularity that would form exactly at criticality. Methods to this end were proposed and shown to work

in the classical case, however, the numerical sensitivity of the quantum mode functions spoil the semiclassical analysis.

I have also presented evidence for long-range correlations of the scalar field both in Chapter 2 and Chapter 6. However, these cannot be attributed to Hawking radiation, as the locations of the correlation peaks do not match the expected behaviour of Hawking partners.

7.3 Future work

This is just the first attempt at simulating the real time dynamics of semiclassical black holes in four dimensions, thus there are many ways to improve and expand this avenue of research.

In terms of improvement, the most obvious direction has to do with the unstable numerical nature of the quantum mode functions present in the semiclassical simulations. As their evolution equations include a term proportional to $\frac{2l+2}{r}$, numerical instabilities are increasingly proned to arise for higher l-value quantum modes. In order to tame these instabilities better, a promising technique is the so-called "summation by part methods" introduced by Gundlach [73]. This method was introduced by the authors to improve the simulations of scalar fields in higher dimensions, however, this poses exactly the same numerical difficulty (namely terms of the form $\frac{D}{r}$, where D is the number of dimensions) as for higher order spherical harmonics (or l-values). Thus, this method could significantly improve the behaviour of the quantum modes, resulting in stable simulations capable of studying semiclassical Choptuik scaling and its fine-structure.

In addition, alternative regularisation schemes could be explored to tame the divergences of the physical observables of the quantum field. There is a regularisation

scheme developed by [75] that is done on a more rigorous mathematical grounding. The authors present a regularisation scheme that is a fully covariant formulation and applies to spacetimes of dynamical black holes as well.

In order to expand on the research presented in this thesis, there are multiple avenues to take. Here, the simplest possible toy model in four dimensional spacetime was studied, namely a spherical symmetric geometry and a massless scalar field. It would be possible to take an axisymmetric geometry instead of a spherical one, or even simulate collapse in a spacetime with no symmetry. However, these would result in even more computationally expensive simulations as presented here, as the computational grid would be more dimensional. Also, a mass could be given to the scalar field, or the matter could be not scalar, but fermionic. Another future direction is to consider self-interacting quantum matter fields. However, this is a somewhat more complicated endeavour as one then needs to solve a coupled system between two-point and higher correlation functions (see [76]).

I believe studying the real time dynamics of the gravitational collapse of quantum fields and semiclassical black holes is an exciting research direction to uncover the mysterious nature of quantum fields in black holes spacetimes, ultimately shining some light on a resolution to the black hole information paradox and giving clues about the nature of quantum gravity.

Bibliography

[1] Benjamin Berczi, Paul M. Saffin, and Shuang-Yong Zhou. Gravitational collapse of quantum fields and choptuik scaling. *Journal of High Energy Physics*, 2022(2), feb 2022.

[2] Benjamin Berczi. https://github.com/benjibrcz/phd, Sep 2023.

[3] Iacopo Carusotto, Serena Fagnocchi, Alessio Recati, Roberto Balbinot, and Alessandro Fabbri. Numerical observation of hawking radiation from acoustic black holes in atomic bose–einstein condensates. *New Journal of Physics*, 10(10):103001, oct 2008.

[4] Oliver Rinne. Type II critical collapse on a single fixed grid: a gauge-driven ingoing boundary method. *General Relativity and Gravitation*, 52(12), dec 2020.

[5] Ehud Eilon and Amos Ori. Adaptive gauge method for long-time double-null simulations of spherical black-hole spacetimes. *Physical Review D*, 93(2), jan 2016.

[6] S. W. Hawking. Particle Creation by Black Holes. *Commun. Math. Phys.*, 43:199–200, 1975.

[7] Bernard Carr, Kazunori Kohri, Yuuiti Sendouda, and Jun'ichi Yokoyama. Constraints on Primordial Black Holes. 2 2020.

[8] J. R. Oppenheimer and H. Snyder. On Continued gravitational contraction. *Phys. Rev.*, 56:455–459, 1939.

[9] B. Datt. *Z. Physik*, 108:314, 1938.

[10] Douglas M. Eardley and Larry Smarr. Time function in numerical relativity. Marginally bound dust collapse. *Phys. Rev. D*, 19:2239–2259, 1979.

[11] Demetrios Christodoulou. Violation of cosmic censorship in the gravitational collapse of a dust cloud. *Commun. Math. Phys.*, 93:171–195, 1984.

[12] Richard P. A. C. Newman. Strengths of naked singularities in Tolman-Bondi space-times. *Class. Quant. Grav.*, 3:527–539, 1986.

[13] B. Waugh and K. Lake. Strengths of Shell Focusing Singularities in Marginally Bound Collapsing Selfsimilar Tolman Space-times. *Phys. Rev. D*, 38:1315–1316, 1988.

[14] P. S. Joshi and I. H. Dwivedi. Naked singularities in spherically symmetric inhomogeneous Tolman-Bondi dust cloud collapse. *Phys. Rev. D*, 47:5357–5369, 1993.

[15] T. P. Singh and P. S. Joshi. The Final fate of spherical inhomogeneous dust collapse. *Class. Quant. Grav.*, 13:559–572, 1996.

[16] Amos Ori and Tsvi Piran. Naked Singularities in Selfsimilar Spherical Gravitational Collapse. *Phys. Rev. Lett.*, 59:2137, 1987.

[17] Amos Ori and Tsvi Piran. Naked Singularities and Other Features of Selfsimilar General Relativistic Gravitational Collapse. *Phys. Rev. D*, 42:1068–1090, 1990.

[18] P. S. Joshi and I. H. Dwivedi. The Structure of Naked Singularity in Self-Similar Gravitational Collapse. *Commun. Math. Phys.*, 146:333–342, 1992.

[19] I. H. Dwivedi and P. S. Joshi. On the occurrence of naked singularity in spherically symmetric gravitational collapse. *Commun. Math. Phys.*, 166:117–128, 1994.

[20] Tomohiro Harada. Final fate of the spherically symmetric collapse of a perfect fluid. *Phys. Rev. D*, 58:104015, 1998.

[21] Kayll Lake. Precursory singularities in spherical gravitational collapse. *Phys. Rev. Lett.*, 68:3129–3132, 1992.

[22] S. W. Hawking and R. Penrose. The Singularities of gravitational collapse and cosmology. *Proc. Roy. Soc. Lond. A*, 314:529–548, 1970.

[23] Roger Penrose. Gravitational collapse and space-time singularities. *Phys. Rev. Lett.*, 14:57–59, 1965.

[24] R. Penrose. Gravitational collapse: The role of general relativity. *Riv. Nuovo Cim.*, 1:252–276, 1969.

[25] Pankaj S. Joshi and Daniele Malafarina. Recent developments in gravitational collapse and spacetime singularities. *Int. J. Mod. Phys. D*, 20:2641–2729, 2011.

[26] D. Christodoulou. The problem of a self-gravitating scalar field. *Commun. Math. Phys.*, 105(3):337–361, 1986.

[27] D. Christodoulou. Global existence of generalized solutions of the spherically symmetric einstein-scalar equations in the large. *Commun. Math. Phys.*, 106(4):587–621, 1986.

[28] D. Christodoulou. The structure and uniqueness of generalized solutions of the spherically symmetric einstein-scalar equations. *Commun. Math. Phys.*, 109(4):591–611, 1987.

[29] D. Christodoulou. A mathematical theory of gravitational collapse. *Commun. Math. Phys.*, 109(4):613–647, 1987.

[30] Demetrios Christodoulou. Examples of naked singularity formation in the gravitational collapse of a scalar field. *Annals Math.*, 140:607–653, 1994.

[31] Demetrios Christodoulou. The Instability of Naked Singularities in the Gravitational Collapse of a Scalar Field. *Annals Math.*, 149:183–217, 1994.

[32] M. W. Choptuik. Universality and scaling in gravitational collapse of massless scalar field. *Phys. Rev. Lett.*, 70:9, 1993.

[33] Patrick R. Brady. Selfsimilar scalar field collapse: Naked singularities and critical behavior. *Phys. Rev. D*, 51:4168–4176, 1995.

[34] Carsten Gundlach. The Choptuik space-time as an eigenvalue problem. *Phys. Rev. Lett.*, 75:3214–3217, 1995.

[35] Carsten Gundlach. Understanding critical collapse of a scalar field. *Phys. Rev. D*, 55:695–713, 1997.

[36] A. M. Abrahams and C. R. Evans. Critical behavior and scaling in vacuum axisymmetric gravitational collapse. *Phys. Rev. Lett.*, 70:2980–2983, 1993.

[37] Charles R. Evans and Jason S. Coleman. Observation of critical phenomena and selfsimilarity in the gravitational collapse of radiation fluid. *Phys. Rev. Lett.*, 72:1782–1785, 1994.

[38] Matthew W. Choptuik, Tadeusz Chmaj, and Piotr Bizon. Critical behavior in gravitational collapse of a Yang-Mills field. *Phys. Rev. Lett.*, 77:424–427, 1996.

[39] Michael Reiterer and Eugene Trubowitz. Choptuik's critical spacetime exists. *Commun. Math. Phys.*, 368(1):143–186, 2019.

[40] Carsten Gundlach and Jose M. Martin-Garcia. Critical phenomena in gravitational collapse. *Living Rev. Rel.*, 10:5, 2007.

[41] Ahmed Almheiri, Donald Marolf, Joseph Polchinski, and James Sully. Black Holes: Complementarity or Firewalls? *JHEP*, 02:062, 2013.

[42] Daniel Harlow and Patrick Hayden. Quantum Computation vs. Firewalls. *JHEP*, 06:085, 2013.

[43] Marija Tomasevic. *Quantum Aspects of Space and Time.* PhD thesis, Barcelona U., 2021.

[44] A. Tomimatsu. Quantum gravitational collapse of a scalar field and the wave function of black hole decay. *Phys. Rev. D*, 52:4540–4547, Oct 1995.

[45] D. Bak, S. P. Kim, S. K. Kim, K.-S. Soh, and J. H. Yee. Wave functions for quantum black hole formation in scalar field collapse. *Phys. Rev. D*, 61:044005, 2000.

[46] Dongsu Bak, Sang Pyo Kim, Sung Ku Kim, Kwang-Sup Soh, and Jae Hyung Yee. Black hole decay and quantum instantons. *Phys. Rev. D*, 62:047504, 2000.

[47] Tanmay Vachaspati and Dejan Stojkovic. Quantum radiation from quantum gravitational collapse. *Phys. Lett. B*, 663:107–110, 2008.

[48] Eric Greenwood and Dejan Stojkovic. Quantum gravitational collapse: Non-singularity and non-locality. *JHEP*, 06:042, 2008.

[49] Tanmay Vachaspati and George Zahariade. Classical-Quantum Correspondence and Hawking Radiation. *JCAP*, 04:013, 2019.

[50] J. G. Russo, L. Susskind, and L. Thorlacius. The Endpoint of Hawking radiation. *Phys. Rev. D*, 46:3444–3449, 1992.

[51] A. Strominger and L. Thorlacius. Universality and scaling at the onset of quantum black hole formation. *Phys. Rev. Lett.*, 72:1584–1587, 1994.

[52] T. Piran and A. Strominger. Numerical analysis of black hole evaporation. *Phys. Rev. D*, 48:4729–4734, 1993.

[53] D. A. Lowe. Semiclassical approach to black hole evaporation. *Phys. Rev. D*, 47:2446–2453, 1993.

[54] Rufus S Hamadé and John M Stewart. The spherically symmetric collapse of a massless scalar field. *Classical and Quantum Gravity*, 13(3):497–512, mar 1996.

[55] Benjamin Berczi, Paul M. Saffin, and Shuang-Yong Zhou. Gravitational collapse with quantum fields. *Phys. Rev. D*, 104(4):L041703, 2021.

[56] Jana N. Guenther, Christian Hoelbling, and Lukas Varnhorst. Semiclassical gravitational collapse of a radially symmetric massless scalar quantum field. 10 2020.

[57] M. Alcubierre. *Introduction to 3+1 Numerical Relativity*. International Series of Monographs on Physics, 2012.

[58] C. Bona, J. Masso, E. Seidel, and J. Stela. New Formalism for Numerical Relativity. *Phys. Rev. Lett.*, 75:600–603, 1995.

[59] B. C. Sanders. Review of entangled coherent states. *Journal of Physics A: Mathematical and Theoretical*, 45(24):244002, May 2012.

[60] W. Pauli and F. Villars. On the invariant regularization in relativistic quantum theory. *Rev. Mod. Phys.*, 21:434–444, Jul 1949.

[61] J. Martin. Everything You Always Wanted To Know About The Cosmological Constant Problem (But Were Afraid To Ask). *Comptes Rendus Physique*, 13:566–665, 2012.

[62] J. Braden, J. R. Bond, and L. Mersini-Houghton. Cosmic bubble and domain wall instabilities I: parametric amplification of linear fluctuations. *JCAP*, 03:007, 2015.

[63] H. O. Kreiss and J. Oliger. *Methods for the approximate solution of time dependent problems*. GARP publication series No. 10, Geneva, 1973.

[64] Shahar Hod and Tsvi Piran. Fine structure of Choptuik's mass scaling relation. *Phys. Rev. D*, 55:440–442, 1997.

[65] John P. Boyd. *Chebyshev and Fourier Spectral Methods*. Dover Books on Mathematics. Dover Publications, Mineola, NY, second edition, 2001.

[66] Thomas W. Baumgarte and Stuart L. Shapiro. Numerical integration of einstein's field equations. *Physical Review D*, 59(2), December 1998.

[67] Masaru Shibata and Takashi Nakamura. Evolution of three-dimensional gravitational waves: Harmonic slicing case. *Phys. Rev. D*, 52:5428–5444, Nov 1995.

[68] M. A. Alcoforado, R. F. Aranha, W. O. Barreto, and H. P. de Oliveira. Multidomain Galerkin–collocation method: spherical collapse of scalar fields II. *Class. Quant. Grav.*, 38(22):225004, 2021.

[69] M. A. Alcoforado, R. F. Aranha, W. O. Barreto, and H. P. de Oliveira. New numerical framework for the generalized Baumgarte-Shapiro-Shibata-Nakamura formulation: The vacuum case for spherical symmetry. *Phys. Rev. D*, 104(8):084065, 2021.

[70] Lloyd N. Trefethen. *Spectral Methods in MATLAB*. Society for Industrial and Applied Mathematics, USA, 2000.

[71] Carl Runge. Über empirische funktionen und die interpolation zwischen äquidistanten ordinaten. *Zeitschrift für Mathematik und Physik, 46: 224–243.*, 1901.

[72] David Garfinkle and G. Comer Duncan. Scaling of curvature in subcritical gravitational collapse. *Phys. Rev. D*, 58:064024, 1998.

[73] Carsten Gundlach, Jose M. Martin-Garcia, and David Garfinkle. Summation by parts methods for spherical harmonic decompositions of the wave equation in any dimensions. *Class. Quant. Grav.*, 30:145003, 2013.

[74] David Garfinkle. Choptuik scaling in null coordinates. *Physical Review D*, 51(10):5558–5561, may 1995.

[75] Adam Levi and Amos Ori. Versatile method for renormalized stress-energy computation in black-hole spacetimes. *Phys. Rev. Lett.*, 117(23):231101, 2016.

[76] Paul M. Saffin, Paul Tognarelli, and Anders Tranberg. Oscillon Lifetime in the Presence of Quantum Fluctuations. *JHEP*, 08:125, 2014.

Appendices

Appendix A

Calculations in the ADM formalism

A.1 Derivation of equations of motion for mode functions

To find the evolution of the quantum mode function π we take

$$\Phi = r^l u(r,t) Y(\theta, \varphi), \tag{A.1}$$

and so we can deduce that

$$\begin{aligned} \Psi &= \partial_r \big(r^l u(r,t) Y(\theta,\varphi) \big) = l r^{l-1} u Y + r^l (\partial_r u) Y, \\ \Pi &= \frac{A^{\frac{1}{2}} B}{\alpha} r^l (\partial_t u) Y. \end{aligned} \tag{A.2}$$

Therefore using these equations we can find the evolution equation for π by substituting these into equation (2.24). This happens as follows:

$$\begin{aligned}\dot{\Pi} &= r^l \partial_t \left(\frac{A^{\frac{1}{2}} B}{\alpha} \partial_t u \right) Y \\ &= \frac{1}{r^2} \partial_r \left[\frac{\alpha B r^2}{A^{\frac{1}{2}}} (l r^{l-1} u Y + r^l (\partial_r u) Y) \right] - \alpha A^{\frac{1}{2}} \frac{l(l+1)}{r^2} r^l u Y,\end{aligned} \tag{A.3}$$

where the first line is by the definition of Π, and the second one is from its evolution equation. Dividing by Y leads us to

$$\begin{aligned}r^l \partial_t \Big(\frac{A^{\frac{1}{2}} B}{\alpha} \partial_t u \Big) &= \frac{1}{r^2} \Bigg[\partial_r \Big(\frac{\alpha B}{A^{\frac{1}{2}}} \Big) (l r^{l+1} u + r^{l+2} \partial_r u) \\ &\quad + \frac{\alpha B}{A^{\frac{1}{2}}} \Big(l(l+1) r^l u + l r^{l+1} \partial_r u + (l+2) r^{l+1} \partial_r u + r^{l+2} \partial_r^2 u \Big) \Bigg] \\ &\quad - \alpha A^{\frac{1}{2}} r^{l-2} l(l+1) u, \\ r^l \partial_t \Big(\frac{A^{\frac{1}{2}} B}{\alpha} \partial_t u \Big) &= \partial_r \Big(\frac{\alpha B}{A^{\frac{1}{2}}} \Big) (l r^{l-1} u + r^l \partial_r u) + \frac{\alpha B}{A^{\frac{1}{2}}} \Big(l(l+1) r^{l-2} u + (2l+2) r^{l-1} \partial_r u + r^l \partial_r^2 u \Big) \\ &\quad - \alpha A^{\frac{1}{2}} r^{l-2} l(l+1) u.\end{aligned} \tag{A.4}$$

Now dividing by r^l we find that

$$\dot{\pi} = \partial_r \left(\frac{\alpha B}{A^{\frac{1}{2}}} \right) \left(\frac{l}{r} u + \partial_r u \right) + \frac{\alpha B}{A^{\frac{1}{2}}} \left(\frac{l(l+1)}{r^2} u + \frac{2l+2}{r} \partial_r u + \partial_r^2 u \right) - \alpha A^{\frac{1}{2}} \frac{l(l+1)}{r^2} u. \tag{A.5}$$

Using the definition for ψ we find that

$$\dot{\pi} = \partial_r \left(\frac{\alpha B}{A^{\frac{1}{2}}} \right) \left(\frac{l}{r} u + \psi \right) + \frac{\alpha B}{A^{\frac{1}{2}}} \left(\frac{2l+2}{r} \psi + \partial_r \psi \right) - \alpha A^{\frac{1}{2}} \Big(\frac{B}{A} - 1 \Big) \frac{l(l+1)}{r^2} u. \tag{A.6}$$

Using λ we need to rewrite the last term, since in theory it is indeed regular, however numerical errors can make it blow up. By using λ we force it to be regular at all times, since λ is antisymmetric. Thus the final evolution equation

is:

$$\dot{\pi} = \partial_r \left(\frac{\alpha B}{A^{\frac{1}{2}}} \right) \left(\frac{l}{r} u + \psi \right) + \frac{\alpha B}{A^{\frac{1}{2}}} \left(\frac{2l+2}{r} \psi + \partial_r \psi \right) - \frac{\alpha B}{A^{\frac{1}{2}}} \lambda \frac{l(l+1)}{r} u. \tag{A.7}$$

At $r = 0$ this becomes

$$\dot{\pi}(r=0) = \frac{\alpha B}{A^{\frac{1}{2}}} \Big[(2l+3) \partial_r \psi + l(l+1) u \partial_r \lambda \Big], \tag{A.8}$$

since $\psi(r=0) = 0$ and $\frac{u}{r}(r=0) = u'(r=0) = \psi(r=0) = 0$. A similar argument is used in the case of the second term in the evolution equation of π for ψ and ψ'. Thus the final evolution equation is:

$$\dot{\pi} = \partial_r \left(\frac{\alpha B}{A^{\frac{1}{2}}} \right) \left(\frac{l}{r} u + \psi \right) + \frac{\alpha B}{A^{\frac{1}{2}}} \left(\frac{2l+2}{r} \psi + \partial_r \psi \right) - \frac{\alpha B}{A^{\frac{1}{2}}} \lambda \frac{l(l+1)}{r} u. \tag{A.9}$$

As mentioned above, λ is used to make sure the terms of the form $(\frac{A}{B} - 1)$ are stable. This in other words means maintaining local flatness at $r = 0$, i.e. $A(r = 0) = B(r = 0)$. One can see that the evolution equation of π is fairly dependent on this condition at the centre.

A.2 Derivation of the analytical value for the cosmological constant counter term

Let us consider a quantum scalar field with an operator expansion

$$\phi(t, \underline{x}) = \int \frac{d^3p}{\sqrt{(2\pi)^3}} \frac{1}{\sqrt{2\omega}} \left[a_p e^{-i\omega t} e^{i\underline{p}.\underline{x}} + h.c. \right], \tag{A.10}$$

$$\pi(t, \underline{x}) = -i \int \frac{d^3p}{\sqrt{(2\pi)^3}} \sqrt{\frac{\omega}{2}} \left[a_p e^{-i\omega t} e^{i\underline{p}.\underline{x}} - h.c. \right], \tag{A.11}$$

$$\omega^2 = \underline{p}^2 + m^2, \tag{A.12}$$

where *h.c.* stands for hermitian conjugate. In order to get the canonical commutation relations we take

$$\left[a_p, a_q^\dagger\right] = \delta(\underline{p} - \underline{q}) \tag{A.13}$$

Now I pick the vacuum defined by

$$a_p|0\rangle = 0 \tag{A.14}$$

and thus one can compute the operator expansions as

$$\langle\phi^2\rangle = \int \frac{d^3p}{(2\pi)^3}\frac{1}{2\omega_p} \tag{A.15}$$

$$\langle(\underline{\nabla}.\phi)^2\rangle = \int \frac{d^3p}{(2\pi)^3}\frac{\underline{p}^2}{2\omega_p} \tag{A.16}$$

$$\langle\pi^2\rangle = \int \frac{d^3p}{(2\pi)^3}\frac{\omega_p^2}{2\omega_p} \tag{A.17}$$

The expectation value of the stress tensor components for a single scalar field are given by

$$\begin{aligned}\langle T_{tt}\rangle &= \frac{1}{2}\pi^2 + \frac{1}{2}(\underline{\nabla}\phi)^2 + \frac{1}{2}m^2\phi^2 \\ &= \int \frac{d^3p}{(2\pi)^3}\frac{1}{2\omega_p}\left[\frac{1}{2}\omega_p^2 + \frac{1}{2}\underline{p}^2 + \frac{1}{2}m^2\right], \\ &= \int \frac{d^3p}{(2\pi)^3}\frac{1}{2\omega_p}\left[\omega_p^2\right],\end{aligned} \tag{A.18}$$

$$\begin{aligned}\frac{1}{3}\left[\langle T_{xx}\rangle + \langle T_{yy}\rangle + \langle T_{zz}\rangle\right] &= \frac{1}{2}\pi^2 - \frac{1}{6}(\underline{\nabla}\phi)^2 - \frac{1}{2}m^2\phi^2 \\ &= \int \frac{d^3p}{(2\pi)^3}\frac{1}{2\omega_p}\left[\frac{1}{2}\omega^2 - \frac{1}{6}\underline{p}^2 - \frac{1}{2}m^2\right] \\ &= \frac{1}{3}\int \frac{d^3p}{(2\pi)^3}\frac{1}{2\omega}\underline{p}^2\end{aligned} \tag{A.19}$$

If I have the physical scalar plus five Pauli-Villars fields, as explained in Section 2.3.4, such that $\phi_{1,3,5}$ are ghosts, then the total stress tensor has the following

components

$$\langle T^{tot}_{tt}\rangle = \int \frac{d^3p}{(2\pi)^3}\frac{1}{2}\left[\omega_p - \omega_{(1)p} + \omega_{(2)p} - \omega_{(3)p} + \omega_{(4)p} - \omega_{(5)p}\right] \tag{A.20}$$

$$\frac{1}{3}\left[\langle T^{reg}_{xx}\rangle + \langle T^{tot}_{yy}\rangle + \langle T^{reg}_{zz}\rangle\right] = \frac{1}{3}\int \frac{d^3p}{(2\pi)^3}\underline{p^2}\frac{1}{2}\left[\frac{1}{\omega} - \frac{1}{\omega_{(1)p}} + \frac{1}{\omega_{(2)p}} - \frac{1}{\omega_{(3)p}} + \frac{1}{\omega_{(4)p}} - \frac{1}{\omega_{(5)p}}\right] \tag{A.21}$$

Then I note that the integrand is spherically symmetric, so I have

$$\int \frac{d^3p}{(2\pi)^3} = \frac{4\pi}{(2\pi)^3}\int dp\; p^2 \tag{A.22}$$

If one looks at the large p limit of the integrands one can see that,

$$\begin{aligned}
\langle T^{tot}_{tt}\rangle =& finite \\
&+ \frac{1}{(2\pi)^2}\int dp\Big[-\frac{p}{2}\left[m_1^2 - m_2^2 + m_3^2 - m_4^2 + m_5^2\right] \\
&+ \frac{1}{8p}\left[m_1^4 - m_2^4 + m_3^4 - m_4^4 + m_5^4\right] + ...\Big] \\
\frac{1}{3}&\left[\langle T^{reg}_{xx}\rangle + \langle T^{tot}_{yy}\rangle + \langle T^{reg}_{zz}\rangle\right] \\
&= finite + \frac{1}{3}\frac{1}{(2\pi)^2}\int dp\Big[-\frac{p}{2}\left[m_1^2 - m_2^2 + m_3^2 - m_4^2 + m_5^2\right] \\
&- \frac{3}{8p}\left[m_1^4 - m_2^4 + m_3^4 - m_4^4 + m_5^4\right] + ...\Big]
\end{aligned} \tag{A.23}$$

in order for an overall finite result one needs

$$m_1^2 - m_2^2 + m_3^2 - m_4^2 + m_5^2 = 0 \tag{A.24}$$

$$m_1^4 - m_2^4 + m_3^4 - m_4^4 + m_5^4 = 0 \tag{A.25}$$

One way to solve this is with (as explained in Section 2.3.4)

$$m_1 = M_{PV},\; m_2 = \sqrt{3}M_{PV},\; m_3 = M_{PV},\; m_4 = \sqrt{3}M_{PV},\; m_5 = 2M_{PV} \tag{A.26}$$

and then we have (taking the physical field to be massless)

$$\langle T^{tot}_{tt}\rangle = \frac{1}{(2\pi)^2}\int_0^{\xi} \xi^2\left[\xi - \sqrt{\xi^2+1} + \sqrt{\xi^2+3} - \sqrt{\xi^2+1} + \sqrt{\xi^2+3} - \sqrt{\xi^2+4}\right] \tag{A.27}$$

$$\frac{1}{3}\left[\langle T^{reg}_{xx}\rangle + \langle T^{tot}_{yy}\rangle + \langle T^{reg}_{zz}\rangle\right] \tag{A.28}$$
$$= \frac{1}{3}\frac{1}{(2\pi)^2}\int_0^{\infty} d\xi\, \xi^4\left[\frac{1}{\xi} - \frac{1}{\sqrt{\xi^2+1}} + \frac{1}{\sqrt{\xi^2+3}} - \frac{1}{\sqrt{\xi^2+1}} + \frac{1}{\sqrt{\xi^2+3}} - \frac{1}{\sqrt{\xi^2+4}}\right].$$

Feeding these expressions into Mathematica one arrives at the following results,

$$\int_0^{\infty} d\xi\, \xi^2\left(\xi - \sqrt{\xi^2+1} + \sqrt{\xi^2+3} - \sqrt{\xi^2+1} + \sqrt{\xi^2+3} - \sqrt{\xi^2+4}\right) = \frac{1}{8}\ln\left(\frac{3^9}{2^{16}}\right) \tag{A.29}$$

$$\int_0^{\infty} d\xi\, \xi^4\left(\frac{1}{\xi} - \frac{1}{\sqrt{\xi^2+1}} + \frac{1}{\sqrt{\xi^2+3}} - \frac{1}{\sqrt{\xi^2+1}} + \frac{1}{\sqrt{\xi^2+3}} - \frac{1}{\sqrt{\xi^2+4}}\right) = -3\frac{1}{8}\ln\left(\frac{3^9}{2^{16}}\right) \tag{A.30}$$

so that

$$\langle T^{tot}_{tt}\rangle = \frac{M^4_{PV}}{(2\pi)^2}\frac{1}{8}\ln\left(\frac{3^9}{2^{16}}\right) \tag{A.31}$$

$$\frac{1}{3}\left[\langle T^{reg}_{xx}\rangle + \langle T^{tot}_{yy}\rangle + \langle T^{reg}_{zz}\rangle\right] = -\frac{M^4_{PV}}{(2\pi)^2}\frac{1}{8}\ln\left(\frac{3^9}{2^{16}}\right) \tag{A.32}$$

By isotropy one has that $T_{xx} = T_{yy} = T_{zz}$, and so it can be seen that

$$\langle T^{tot}_{\mu\nu}\rangle = -\frac{M^4_{PV}}{(2\pi)^2}\frac{1}{8}\ln\left(\frac{3^9}{2^{16}}\right)\eta_{\mu\nu}. \tag{A.33}$$

This then gives the cosmological constant counter term, as we require the Minkowski vacuum to have vanishing physical stress tensor,

$$\Lambda_{ct} = \frac{M^4_{PV}}{(2\pi)^2}\frac{1}{8}\ln\left(\frac{3^9}{2^{16}}\right), \tag{A.34}$$

Note that it is $\mathcal{O}(M_{PV}^4)$ as expected.

A.3 Derivation of equations of motion for mode functions with nonzero shift

To find the evolution equation of v let us use the Π eom, paired with the above definitions, and using, schematically that

$$\begin{aligned} "\hat{\Phi} &= \sum r^l u Y", \\ "\hat{\Pi} &= \sum r^l v Y", \\ "\hat{\Xi} &= \sum r^l (w + \psi^2 l r^{-2} u) Y". \end{aligned} \tag{A.35}$$

Then plugging these into the eom of Π, adding the angular and a mass term, and dividing by Y, we get:

$$\begin{aligned} r^l \dot{v} =& r\beta(l r^{l-1} v + r^l v') + (2\beta + \alpha\psi^{-6} r^2 K) r^l v \\ &+ \alpha\psi^{-2} r (l r^{l-1} w + r^l w' + 2\psi\psi' l r^{l-2} u + \psi^2 l(l-2) r^{l-3} u + \psi^2 l r^{l-2} u') \\ &+ \psi^{-2}(r\alpha' + 3\alpha)(r^l w + \psi^2 l r^{l-2} u) - \alpha \frac{l(l+1)}{r^2} r^l u - m^2 \alpha \psi^4 r^l u, \end{aligned} \tag{A.36}$$

which after some rearranging and dividing by r^l this becomes

$$\begin{aligned} \dot{v} =& r\beta v' + ((2+l)\beta + \alpha\psi^{-6} r^2 K) v \\ &+ \alpha\psi^{-2} r (2l \frac{w}{r} + w' + 2l\psi\psi' \frac{u}{r} + \psi^2 l(l-2) \frac{u'}{r^3}) \\ &+ \psi^{-2} r\alpha' w + l \frac{\alpha'}{r} u + 3\alpha\psi^{-2} w + 3l \frac{u}{r^2} - \alpha \frac{l(l+1)}{r^2} u - m^2 \alpha \psi^4 u, \end{aligned} \tag{A.37}$$

collecting similar terms

$$\begin{aligned}\dot{v} =& r\beta v' + \Big[(2+l)\beta + \alpha\psi^{-6}r^2K\Big]v \\ &+ \alpha\psi^{-2}\Big[(2l+3)w + rw'\Big] + l\Big[\alpha' + 2\frac{\psi'}{\psi}\Big]\frac{u}{r} + \psi^{-2}r\alpha' w \\ &+ \alpha\Big[\frac{l(l-2)}{r^2} + \frac{3}{r^2} - \frac{l(l+1)}{r^2}\Big]u - m^2\alpha\psi^4 u,\end{aligned} \tag{A.38}$$

where thankfully the $1/r^2$ terms cancel and we get the final eom for v:

$$\boxed{\begin{aligned}\dot{v} =& r\beta v' + \Big[(2+l)\beta + \alpha\psi^{-6}r^2K\Big]v + \alpha\psi^{-2}rw' \qquad (A.39)\\ &+ \psi^{-2}\Big[r\alpha' + (2l+3)\alpha\Big]w + \frac{l}{r}\Big[\alpha' + 2\frac{\psi'}{\psi}\Big]u - m^2\alpha\psi^4 u. \qquad (A.40)\end{aligned}}$$

One can check that this reduces to the eom of Π in case of $l = 0$.

Then through the definition of w, simply taking its time derivative, one can find its eom as well:

$$\begin{aligned}\dot{w} =& r^{-1}2\psi\dot{\psi}u' + r^{-1}\psi^2\dot{u}', \\ \dot{w} =& 2\frac{\dot{\psi}}{\psi}w + r^{-1}\psi^2\dot{u}', \\ \dot{w} =& 2\frac{w}{\psi}\Big[\frac{1}{2}\beta\psi + r\beta\psi' + \frac{1}{4}r^2\alpha\psi^{-5}K\Big] \\ &+ \frac{\psi^2}{r}\Big[l\beta' u + l\beta u' + \beta u' + r\beta' u' + r\beta u'' + \alpha'\psi^{-4}v - 4\alpha\psi^{-5}\psi' v + \alpha\psi - 4v'\Big],\end{aligned} \tag{A.41}$$

where we have used the eom of ψ and the eom of u:

$$\boxed{\dot{u} = l\beta u + r\beta u' + \alpha\psi^{-4}v.} \tag{A.42}$$

Using some rearrangements and finding u'' in terms of w' and w and also plugging

in the equation for β', we arrive at

$$\begin{aligned}\dot{w} =&\Big[\beta + 2r\beta\frac{\psi'}{\psi} + \frac{1}{2}r^2\alpha\psi^{-6}K\Big]w \\ &+ \frac{3}{2}l\alpha\psi^{-4}Ku + (l+1)\beta w + \frac{3}{2}r^2\alpha\psi^{-6}Kw + \beta w - 2r\frac{\psi'}{\psi}\beta w + r\beta w' \\ &+ \alpha'\psi^{-2}\frac{v}{r} - 4\alpha\psi^{-3}\psi'\frac{v}{r} + \alpha\psi^{-2}\frac{v'}{r}.\end{aligned} \tag{A.43}$$

Once again collecting similar terms we get

$$\boxed{\begin{aligned}\dot{w} =&r\beta w' + \Big[(l+3)\beta + 2\alpha\psi^{-6}r^2K\Big]w + \alpha\psi^{-2}\frac{v'}{r} && \text{(A.44)}\\ &+ \psi^{-3}(\psi\alpha' - 4\alpha\psi')\frac{v}{r} + \frac{3}{2}l\alpha\psi^{-4}Ku. && \text{(A.45)}\end{aligned}}$$

Again, if we set $l = 0$ we recover the zero mode equation, which is the same as for İI.

Appendix B

Calculations in the double null formalism

B.1 Derivation of equation of motion for mode functions

To find the equations of motion of the quantum mode functions let us (schematically) expand the full quantum field as

$$"\Phi(u,v,\theta,\varphi) = r(u,v)^l f(u,v) Y_l^m(\theta,\varphi)," \tag{B.1}$$

and we can evaluate both sides of the previous equation to find the equation of motion for the mode functions $f(u,v)$, let us start with the left hand side:

$$\begin{aligned}
\partial_u\partial_v\Phi &= \partial_u\partial_v(r^l f Y) = Y\partial_u\partial_v(r^l f) \\
&= Y\Big[\partial_u(lr^{l-1}\partial_v r f + r^l\partial_v f)\Big] \\
&= Y\Big[(l(l-1)r^{l-2}\partial_u r\partial_v r f + lr^{l-1}\partial_u\partial_v r f + lr^{l-1}\partial_v r\partial_u f + lr^{l-1}\partial_u r\partial_v f + r^l\partial_u\partial_v f)\Big], \\
&= Yr^l\Big[(l(l-1)r^{-2}\partial_u r\partial_v r f + lr^{-1}\partial_u\partial_v r f + lr^{-1}\partial_v r\partial_u f + lr^{-1}\partial_u r\partial_v f + \partial_u\partial_v f)\Big],
\end{aligned} \tag{B.2}$$

then the other terms of the equation:

$$\begin{aligned}
\partial_u\partial_v\Phi &= -\frac{1}{r}\Big[\partial_u r\partial_v\Phi + \partial_v r\partial_u\Phi\Big] - \frac{e^\sigma}{4}\frac{l(l+1)}{r^2}\Phi - m^2e^\sigma\Phi, \\
&= -\frac{1}{r}\Big[\partial_u r\partial_v(r^l fY) + \partial_v r\partial_u(r^l fY)\Big] - \frac{e^\sigma}{4}\frac{l(l+1)}{r^2}r^l fY + m^2e^\sigma r^l fY, \\
&= Y\Bigg[-\frac{1}{r}\Big[\partial_u r\partial_v(r^l f) + \partial_v r\partial_u(r^l f)\Big] - \frac{e^\sigma}{4}\frac{l(l+1)}{r^2}r^l f - m^2e^\sigma r^l f\Bigg], \\
&= Y\Bigg[-\frac{1}{r}\Big[lr^{l-1}\partial_u r\partial_v r f + r^l\partial_u r\partial_v f + lr^{l-1}\partial_v r\partial_u r f + r^l\partial_v r\partial_u f\Big] \\
&- \frac{e^\sigma}{4}\frac{l(l+1)}{r^2}r^l f - m^2e^\sigma r^l f\Bigg], \\
&= Yr^l\Bigg[-\frac{1}{r}\Big[lr^{-1}\partial_u r\partial_v r f + \partial_u r\partial_v f + lr^{-1}\partial_v r\partial_u r f + \partial_v r\partial_u f\Big] - \frac{e^\sigma}{4}\frac{l(l+1)}{r^2}f - m^2e^\sigma f\Bigg].
\end{aligned} \tag{B.3}$$

Now we can equate the two right sides of the above equations and eliminate Yr^l:

$$\begin{aligned}
&\frac{l(l-1)}{r^2}\partial_u r\partial_v r f + \frac{l}{r}\partial_u\partial_v r f + \frac{l}{r}\partial_v r\partial_u f + \frac{l}{r}\partial_u r\partial_v f + \partial_u\partial_v f = \\
&\qquad -\frac{1}{r}\Big[\frac{l}{r}\partial_u r\partial_v r f + \partial_u r\partial_v f + \frac{l}{r}\partial_v r\partial_u r f + \partial_v r\partial_u f\Big] - \frac{e^\sigma}{4}\frac{l(l+1)}{r^2}f - m^2e^\sigma f,
\end{aligned} \tag{B.4}$$

now rearranging for $\partial_u\partial_v f$:

$$\begin{aligned}\partial_u\partial_v f = &-\frac{l(l-1)}{r^2}\partial_u r\partial_v rf - \frac{l}{r}\partial_u\partial_v rf - \frac{l}{r}\partial_v r\partial_u f - \frac{l}{r}\partial_u r\partial_v f \\ &-\frac{l}{r^2}\partial_u r\partial_v rf - \partial_u r\frac{\partial_v f}{r} - \frac{l}{r^2}\partial_v r\partial_u rf - \partial_v r\frac{\partial_u f}{r} - \frac{e^\sigma}{4}\frac{l(l+1)}{r^2}f - m^2e^\sigma f,\end{aligned} \tag{B.5}$$

then collecting similar terms:

$$\begin{aligned}\partial_u\partial_v f = &-\frac{l(l-1)}{r^2}\partial_u r\partial_v rf - \frac{l}{r^2}\partial_u r\partial_v rf - \frac{l}{r^2}\partial_v r\partial_u rf \\ &-\frac{l}{r}\partial_v r\partial_u f - \frac{1}{r}\partial_v r\partial_u f \\ &-\frac{l}{r}\partial_u r\partial_v f - \frac{1}{r}\partial_u r\partial_v f \\ &-\frac{l}{r}\partial_u\partial_v rf \\ &-\frac{e^\sigma}{4}\frac{l(l+1)}{r^2}f \\ &-m^2e^\sigma f,\end{aligned} \tag{B.6}$$

which then becomes

$$\begin{aligned}\partial_u\partial_v f = &-\frac{l(l+1)}{r^2}\partial_u r\partial_v rf \\ &-\frac{l+1}{r}\Big(\partial_v r\partial_u f + \partial_u r\partial_v f\Big) \\ &-\frac{l}{r}\partial_u\partial_v rf \\ &-\frac{e^\sigma}{4}\frac{l(l+1)}{r^2}f \\ &-m^2e^\sigma f,\end{aligned} \tag{B.7}$$

and we also know from the Einstein equations that

$$\begin{aligned}\partial_u\partial_v r &= -\frac{\partial_u r\partial_v r}{r} - \frac{e^\sigma}{4r}\Big(1-(\partial_\theta\Phi)^2\Big), \\ &= -\frac{1}{r}\Big(\frac{e^\sigma}{4}\Big(1-(\partial_\theta\Phi)^2\Big) + \partial_u r\partial_v r\Big).\end{aligned} \tag{B.8}$$

Using this in the equation of motion for f we get:

$$\begin{aligned}\partial_u\partial_v f =& -\frac{l(l+1)}{r^2}\partial_u r\partial_v r f \\ &- \frac{l+1}{r}\Big(\partial_v r\partial_u f + \partial_u r\partial_v f\Big) \\ &+ \frac{l}{r^2}\Big(\frac{e^\sigma}{4}(1-(\partial_\theta\Phi)^2) + \partial_u r\partial_v r\Big) f \\ &- \frac{e^\sigma}{4}\frac{l(l+1)}{r^2} f \\ &- m^2 e^\sigma f,\end{aligned} \tag{B.9}$$

and again rearranging:

$$\begin{aligned}\partial_u\partial_v f =& -\frac{l+1}{r}\Big(\partial_v r\partial_u f + \partial_u r\partial_v f\Big) \\ &+ \frac{l}{r^2}\Big(\frac{e^\sigma}{4}(1-(\partial_\theta\Phi)^2) + \partial_u r\partial_v r\Big) f \\ &- \frac{l(l+1)}{r^2}\Big(\frac{e^\sigma}{4}(1-(\partial_\theta\Phi)^2) + \partial_u r\partial_v r\Big) f \\ &- m^2 e^\sigma f,\end{aligned} \tag{B.10}$$

which then ultimately becomes:

$$\partial_u\partial_v f = -\frac{l+1}{r}\Big(\partial_v r\partial_u f + \partial_u r\partial_v f\Big) - \frac{l^2}{r^2}\Big(\frac{e^\sigma}{4}(1-(\partial_\theta\Phi)^2) + \partial_u r\partial_v r\Big) f - m^2 e^\sigma f. \tag{B.11}$$